ABSTRACT

Title of dissertation: EXPERIMENTAL INVESTIGATIONS OF CAPILLARY EFFECTS ON NONLINEAR FREE-SURFACE WAVES

James D. Diorio, Doctor of Philosophy, 2009

Dissertation directed by: Professor James Duncan
Department of Mechanical Engineering

This thesis presents the results of three experiments on various aspects of the effects of surface tension on nonlinear free-surface waves. The first two experiments focus on capillary effects on the breaking of short-wavelength gravity waves, a problem of interest in areas of physical oceanography and remote sensing. The third experiment is concerned with the bifurcation of solitary capillary-gravity waves, a problem that is relevant in the study of nonlinear, dispersive wave systems.

In the first set of experiments, streamwise profile measurements were made of spilling breakers at the point of incipient breaking. Both wind-waves and mechanically generated waves were investigated in this study, with gravity wavelengths in the range of 10–120 cm. Although it has been previously argued that the crest shape is dependent only on the surface tension, the results reported herein are to the contrary as several geometrical parameters used to describe the crest change significantly with the wavelength. However, the non-dimensional crest shape is self-similar, with two-shape parameters that depend on a measure of the local wave

slope. This self-similarity persists over the entire range of wavelengths and breaker conditions measured, indicating a universal behavior in the near-crest dynamics that is independent of the method used to generate the wave. The measured wave slope is found to be related to the wave growth rate and phase-speed prior to breaking, a result that contributes towards the development of a breaking criterion for unsteady capillary-gravity waves.

The second set of experiments examines the cross-stream surface structure in the turbulent breaking zone generated by short-wavelength breakers. Waves in this study were generated using a mechanical wedge and ranged in wavelength from 80–120 cm. To isolate the effects of surface tension on the flow, the important experimental parameters were adjusted to produce Froude-scaled, dispersively-focused wave packets. The results show the development of "quasi"-2D streamwise ripples along with smaller cross-stream ripples that grow as breaking develops and can become comparable in amplitude to the streamwise ripples for larger breakers. It is found that the amplitude of the cross-stream surface ripples scale as $\bar{\lambda}^3$, where $\bar{\lambda}$ is the average wavelength of the wave packet. The cross-stream ripple activity appears to be highest in the "troughs" of the larger streamwise ripples, with the appearance of persistent "scar"-like features. Based on these observations, a simple model for the coupling between the vorticity and capillary structure in the breaking zone is conjectured.

The third set of experiments focuses on the generation of capillary-gravity waves by a pressure source moving near the minimum phase speed c_{min}. Near this minimum, nonlinear capillary-gravity solitary waves, or "lumps", have been shown

to exist theoretically. We identify an abrupt transition to a wave-like state that features a localized solitary wave that trails the pressure forcing. This trailing wave is steady, fully localized in 3D, elongated in the cross-stream relative to the streamwise direction, and has a one-to-one relationship between height and phase speed. All of these characterisitics are commensurate with the freely propogating "lumps" computed by previous authors, and a quantitative comparison between these previous numerical calculations and the current experiments is presented. At speeds closer to c_{min}, a new time-dependent state is observed that can qualitatively be described by the shedding of solitary depressions from the tips of a "V"-shaped pattern. These results are discussed in conjunction with a new theoretical model for these waves that employs nonlinear and viscous effects, both of which are crucial in capturing the salient features of the surface response. While discussed in the context of water waves, these results have applicaiton to other wave systems where nonlinear and dispersive effects are important.

EXPERIMENTAL INVESTIGATIONS OF CAPILLARY EFFECTS ON NONLINEAR FREE-SURFACE WAVES

by

James D. Diorio

Dissertation submitted to the Faculty of the Graduate School of the
University of Maryland, College Park in partial fulfillment
of the requirements for the degree of
Doctor of Philosophy
2009

Advisory Committee:
Professor James Duncan, Chair/Advisor
Professor Kenneth Kiger
Professor Daniel Lathrop
Professor Larry Sanford
Professor James Wallace

He would talk to you about Jesus and Leonardo Da Vinci, all of these great historical figures. And it made you realize that your little piece of greatness, whatever it may be, was worth like hell fighting for.

–Herb Elliott (1960 Gold Medalist in the 1500 meters) on coach Percy Cerutty

How can he remember well his ignorance – which his growth requires – who has so often to use his knowledge?

–Henry David Thoreau

Dedication

For Gaga, who taught me how to never stop asking questions.

Acknowledgments

As with any document that is more than 100 pages, it wasn't completed alone. Furthermore, when you spend more than five years in one place, you undoubtedly come in contact with some of the finest people who help you along your way. This section is dedicated to them.

First and foremost, I must thank my lab colleagues, past and present. None of the work done in thesis would have been completed if it weren't for the hard work of students who came before me, and every painstaking hour they spent building tanks and designing software made my job that much easier. To the people I have worked with most directly – Dr. Xinan Liu, Dr. Mostafa Shakeri, Dr. Eric Maxeiner, to future Drs. Mohammad Tavakolinajad and Christine Ikeda – I thank you. Nothing gets done in our lab alone, and the selflessness you have all shown over the years is a truly remarkable feature of our group. Although I probably speak too much at lab meetings, I hope that you have all enjoyed working me as much as I have working with you. To the undergraduates, namely Andrew Lisiewski, Ryan Harris, Joe Zuech and Nick Watkins, for their hours of help with the gravity-capillary lumps experiment and the cross-stream profile measurements. I hope your abilities to stare at a computer screen or to run a carriage repeatedly serves you all well in your future careers. To the generations of German students I've endured, thanks for allowing me to practice my limited (and probably somewhat offensive) German. Thanks also to Dr. T.R. Akylas at MIT for his help with understanding the lump theory.

A sincere thank you to my ARCS Foundation "family". Your hard work and

welcoming ways made my last few years at Maryland not only easier, but more enjoyable as well. A special thanks to my “space mom” Mary Snitch, my “ARCS mom” Toni Schierling, and Angie Delaney and Diana Alexander for their book suggestions and conversation. Your mission is a great one, and any way in which I can help I will.

Thanks to my committe members, Dr. Kenneth Kiger, Dr. Dan Lathrop, Dr. Larry Sanford, and Dr. James Wallace, for even dreaming of taking the time to read this. May my soporific prose make the rest of your daily lives seem that much more interesting. To Dr. Ugo Piomelli, whose help early on will not be forgotten, but whose stress-inducing CFD class may take years to recover from. Thanks to Penny Komsat who endlessly endured my requests for pizza. Thanks to Dr. Doug Kelley whose MATLAB prowess I can only hope to imitate, and again to Dr. Wallace for pushing us to do “just one more” analysis. Thanks again to Dr. Kiger for being truly dedicated to his teaching and for his open and honest conversation. Thanks to Dr. Jerry Gollub for helping me find my way and writing me endless recommendations, and to Dr. Paulo Arratia for his honest and experienced guidance.

I certainly wouldn’t be writing any of this if it weren’t for the love and support of my parents, John and Deborah. I love you both and I hope you will now permit me to say that I’ve finally had enough school and I don’t want to go anymore. To my siblings Amanda and Joshua, whose love of life and dedication to their dreams are palpable. If I love my chosen profession half as much as the two of you I will consider it a success. To Dr. Dan Cole, Dr. Martha Betz, and future Drs. Brendan Casey, Nick Piekiel and Kyle Sullivan, who have shared these years with me. May we preserve

in our memories this unique time in our lives, including the back-to-back intramural basketball championships. To Ms. Hollis Richardson, whose companionship and understanding have been a blessing this past year. To all of the friends I've had here at Maryland, you've made my years here a truly special experience.

But the most deserving of thanks is reserved for my advisor, Jim Duncan. Although my more eager and impetuous nature tended to clash with your pragmatic and fastidious (and most often correct) approach, the result of our labors was always something to be proud of. You embody the true spirit of the scholar-teacher and all that I see as right with academia. Your passion for your work is truly infectious. Always remember that your "lasting impact" extends beyond the science to those who have had the privelage of learning from you.

Table of Contents

List of Tables ix

List of Figures x

List of Abbreviations xii

1 Introduction 1
- 1.1 Waves on a liquid free-surface . . . 1
- 1.2 Pure gravity waves . . . 5
- 1.3 Capillary effects . . . 7
- 1.4 Thesis outline . . . 9

2 Streamwise profile measurements of spilling breakers at incipient breaking 11
- 2.1 Abstract . . . 11
- 2.2 Summary of previous work . . . 12
- 2.3 Experimental details . . . 17
  - 2.3.1 The wave tank . . . 17
  - 2.3.2 Wave generation . . . 20
  - 2.3.3 Wave profile measurement . . . 24
- 2.4 Results and discussion . . . 26
  - 2.4.1 Crest geometry . . . 26
  - 2.4.2 The slope parameter, m . . . 35
- 2.5 Summary and conclusions . . . 38

3 Cross-stream profile measurements of unsteady spilling breakers 40
- 3.1 Abstract . . . 40
- 3.2 Summary of previous work . . . 41
- 3.3 Experimental details . . . 47
  - 3.3.1 Wave generation: isolating the effect of surface tension . . . 47
  - 3.3.2 Wave profile measurement . . . 49
- 3.4 Results and discussion . . . 54
  - 3.4.1 Frequency dependence: the effect of Weber number . . . 54
  - 3.4.2 Amplitude dependence . . . 70
  - 3.4.3 History of the surface gradient and curvature . . . 72
- 3.5 Summary and conclusions . . . 84

4 Non-linear gravity-capillary waves generated by a moving pressure source 87
- 4.1 Abstract . . . 87
- 4.2 Summary of previous work . . . 88
- 4.3 Experimental details . . . 95
  - 4.3.1 Experimental setup . . . 95
  - 4.3.2 Measurement details . . . 97
- 4.4 Results and discussion . . . 100

4.4.1 Behavioral states and a critical jump condition 100
4.4.2 Time-dependent behavior 106
4.4.2.1 Transition to state II 106
4.4.2.2 State III behavior 110
4.4.3 Three-dimensional shape 114
4.5 Summary and conclusions 118

5 Summary of contributions and future work 120

A Wave growth rate 124

List of Tables

2.1 The parameters of the five wave-maker motions used with the dispersive focusing technique. 21
2.2 The parameters used for the three waves generated using the sideband instability mechanism. 23

3.1 The wave-maker and carriage parameters used for the cross-stream profile experiments. 49

List of Figures

2.1 Schematic of wave tank with wave-maker, wind tunnel and instrument carriage. . . . 19
2.2 Images of wave crests at incipient breaking from high-speed movies in three separate experiments. . . . 27
2.3 Crest profiles of the three waves shown in figure 2.2. . . . 29
2.4 Average and standard deviation of the scaled and rotated bulge profiles for all 18 waves studied herein. . . . 31
2.5 Plots showing the variation of (a) L_s and (b) t_p with the local slope parameter, m. . . . 32
2.6 Measurements and analysis of the length of the first capillary wave upstream of the toe, λ_c. . . . 34
2.7 Contour plot of the slope m as a function of the dimensionless wave phase speed c_p/c_{min} and the non-dimensional average growth rate P/c_p. 36

3.1 Schematic of the setup for measuring the cross-stream profiles. . . . 51
3.2 Images taken by the cross-stream camera during a typical breaking event. . . . 55
3.3 Plots of the nondimensional horizontally averaged wave height $\bar{z}/\bar{\lambda}$ and nondimensional standard deviation of the cross-stream wave profile $\sigma/\bar{\lambda}$ versus nondimensional time t/T. . . . 56
3.4 Figure showing how large cross-stream asymmetries in the breaker profiles can affect the measurement of the smaller ripples. . . . 57
3.5 Figure 14 from [1] showing the streamwise profile history for a spilling breaker generated by the dispersive focusing technique. . . . 59
3.6 Plots of $\bar{z}/\bar{\lambda}$ and $\sigma/\bar{\lambda}$ versus nondimensional time t/T for three different values of $\bar{f}$. . . . 60
3.7 Plot of $\bar{\sigma}/\bar{\lambda}$ versus We, where $\bar{\sigma}$ is the value of σ from figure 3.6 averaged over the range $0.4 < t/T < 0.7$. . . . 61
3.8 Cross-stream profile histories for three different frequencies with a normalized wave-maker amplitude $A/\bar{\lambda} = 0.0522$. . . . 65
3.9 Cross-stream spectra history for three different frequencies with a normalized wave-maker amplitude $A/\bar{\lambda} = 0.0522$. . . . 68
3.10 Plot $\bar{z}/\bar{\lambda}$ and $\sigma/\bar{\lambda}$ versus t/T for $\bar{f} = 1.26$ Hz and with 5 different wave-maker amplitudes. . . . 71
3.11 Plot of $\bar{\sigma}$ versus $A/\bar{\lambda}$ for $\bar{f} = 1.26$ Hz. . . . 72
3.12 Cross-stream spectra history for $\bar{f}$=1.26 Hz and four different wave-maker amplitudes $A/\bar{\lambda}$. . . . 76
3.13 Histories of the cross-stream amplitude and its varioius derivatives for one run with $\bar{f} = 1.15$ Hz and $A/\bar{\lambda} = 0.0522$. . . . 81
3.14 A schematic showing a possible model for the distribution of vorticity in the shear layer produced by a spilling breaker showing the location of high shear regions in the troughs of the streamwise ripples 84

4.1 Figure 1 from [2] showing a lump solution to the KP equation for $Bo > 1/3$. 91
4.2 Schematic of the experimental setup used in the solitary wave experiment. 97
4.3 Images of the wave pattern taken from above the water surface with the high-speed camera. 101
4.4 Shadowgraph images showing the shape of the wave pattern for several values of the speed parameter α for $\epsilon = 0.43$. 102
4.5 Normalized peak depth of the wave pattern, h_{min}/h_0, versus α for $\epsilon = 0.43$. 104
4.6 Normalized peak depth of the wave pattern h_{min}/λ_{min} versus the speed parameter α. 105
4.7 Plot of the normalized peak depth of the wave pattern h_{min}/h_0 as a function of time for $\epsilon = 0.43$ and various values of α. 107
4.8 Plot of the normalized peak depth of the wave pattern h_{min}/h_0 as a function of time for $\epsilon = 0.30$ (upper plot) and $\epsilon = 0.51$ (lower plot) for various values of α. 108
4.9 Plot of the normalized peak depth of the wave pattern h_{min}/h_0 as a function of time for $\epsilon = 0.43$ and $\alpha = 0.905$. 110
4.10 Sequence of images showing the "shedding" oscillation of the wave pattern in state III from above the water surface for $\epsilon = 0.43$ and $\alpha = 0.981$. 112
4.11 Sequential shadowgraph images taken from below the water surface showing the oscillation of the wave pattern for $\epsilon = 0.51$ and $\alpha = 0.958$. 113
4.12 A typical surface plot obtained using the LIF method with $\epsilon = 0.43$ and $\alpha = 0.95$. 116
4.13 Streamwise (solid) and cross-stream (dashed) profiles at the center of the surface pattern shown in figure 4.12. 117
4.14 Top view (x-y plane) of the reconstructed wave pattern for $\epsilon = 0.43$ and at three different values of α. 118

A.1 Non-dimensional height ($z(t)/z_{t=0}$) versus non-dimensional time ($t\bar{f}$) for the dispersively focused breakers. 125

List of Abbreviations

τ	fluid surface tension
ρ	fluid density
g	gravity
λ	wavelength
f	wave frequency
T	wave period
k	wavenumber ($\equiv 2\pi/\lambda$)
c_p	wave phase velocity ($\equiv \omega/k$)
c_g	wave group velocity ($\equiv \partial\omega/\partial k$)
ω	radian frequency ($\equiv 2\pi f$)
l_{gc}	gravity-capillary length scale $(\tau/g\rho)^{1/2}$
λ_{min}	minimum wavelength of linear gravity-capillary waves $= 2\pi(\tau/g\rho)^{1/2}$
c_{min}	minimum phase speed of linear gravity-capillary waves $= (4g\tau/\rho)^{1/4}$
U	characteristic velocitiy scale
L	characteristic length scale
H	fluid depth
Fr	Froude number ($\equiv U^2/gL$)
We	Weber number ($\equiv \rho U^2 L/\tau$)
Bo	Bond number $\tau/(\rho g H^2)$
$\bar{f}$	average frequency in the dispersive focusing method
$\bar{\lambda}$	average wavelength in the dispersive focusing method
A	amplitude of the wave-maker in the dispersive focusing method
$z(t)$	wave crest height as a function of time
Δz	vertical distance from the crest toe to the point of maximum height
λ_c	wavelength of the primary capillary wave upstream of the crest toe
m	surface slope at the crest toe
L_s	length of the crest bulge
t_p	thickness of the crest bulge
q_t	flow speed at the crest toe
P	average wave growth rate prior to breaking
f_0	initial frequency in the side-band instability method
k_0	initial wavenumber in the side-band instability method
a_0	average initial amplitude in the side-band instability method
f_+	upper side-band frequency in the side-band instability method
f_-	lower side-band frequency in the side-band instability method
γ	side-band amplitude parameter
$\bar{z}$	cross-stream averaged wave height
σ	measure of the cross-stream ripple amplitude
α	ratio of the speed of the pressure forcing to the minimum phase speed
α_c	critical value of α where the transition between states I and II occur
h_0	depth of the surface depression when the carriage is stationary
h_{min}	peak depth of the wave pattern when the carriage is moving

Chapter 1

Introduction

1.1 Waves on a liquid free-surface

The study of waves on a liquid free-surface is one of the oldest and scientifically richest areas of fluid mechanics. With origins dating as far back as the work of Sir Isaac Newton, extended through the 18th and 19th centuries by such luminaries as Laplace, Cauchy and Stokes, and aided in no small part over the centuries by societal dependence on shipping needs, surface wave theory has revealed itself to be a seemingly endless supply of complex phenomena. For a truly absorbing review of the historical developments of surface wave theory see [3, 4].

In an ideal sense, a liquid surface is considered to be "free" if it is exposed to an atmosphere of gas or vapor and subject only to a constant normal stress, like pressure. A more realistic scenario is one in which the atmosphere can also interact with the surface through shear, heat flux and mass flux [5]. This second, more complicated surface is sometimes referred to as a liquid-gas interface. Placing the peculiarities in appellation aside, in this thesis we consider a "free liquid surface" to be of the second type, where the liquid surface is free to interact with a vapor or gaseous atmosphere, as opposed to a liquid-solid or liquid-liquid boundary. The most ready examples of such free surfaces are open bodies of water such as lakes, oceans and rivers. Free surfaces also arise in many other fluid mechanics applications such

as film and coating flows, liquid jets, droplets, and open channel flows. Regardless of the application, when a liquid free surface is disturbed from equilibrium, wave motion can result. This wave motion is typically due to the action of two restoring forces: gravity and capillarity (i.e. surface tension). Which force dominates depends on the scale of the motion. To see this mathetmatically, consider first the Navier-Stokes equation

$$\frac{D\mathbf{u}}{Dt} = -g\hat{\mathbf{k}} + \frac{1}{\rho}\boldsymbol{\nabla} \cdot \overline{\overline{\boldsymbol{\sigma}}} \tag{1.1}$$

where $\mathbf{u}$ is velocity, g is gravity, $\hat{\mathbf{k}}$ is the vertical unit vector, ρ is the fluid density, and $\overline{\overline{\boldsymbol{\sigma}}}$ is the stress tensor with components given by

$$\sigma_{ij} = -P\delta_{ij} + \mu\left(\frac{\partial u_i}{\partial x_j} + \frac{\partial u_j}{\partial x_i}\right) + \delta_{ij}\lambda\frac{\partial u_k}{\partial x_k} \tag{1.2}$$

where P is pressure, δ_{ij} is the Dirac delta function, μ is the coefficient of shear viscosity, u_i are the components of velocity, and λ is the coefficient of dilational viscosity. For water, the liquid can be considered incompressible ($\nabla \cdot \mathbf{u} = 0$) so the last term in equation 1.2 is zero. Water waves are also typically considered to be inviscid ($\mu = 0$), although in reality there is a very small viscous boundary layer near the free-surface. However, it will be shown in section 1.3 that this boundary layer is typically quite small in comparision to the wavelength of the waves, except for very small capillary waves ($\lesssim 1$ mm), so the inviscid assumption is often quite accurate and $\sigma_{ij} = -P\delta_{ij}$. For an inviscid, irrotational, incompressible fluid, equation 1.1 can be written as Bernoulli's equation

$$P = P_{atm} - \rho g z - \rho\left[\frac{\partial \phi}{\partial t} + \frac{\nabla\phi \cdot \nabla\phi}{2}\right] \tag{1.3}$$

where P_{atm} is the pressure in the gaseous atmosphere at the free surface, z is the depth below the free surface (taken as negative moving downwards), and ϕ is the velocity potential, such that $\mathbf{u} = \nabla\phi$. Because of incompressibility, the velocity potential is governed by Laplace's equation $\nabla^2\phi = 0$. The fluid motion is then prescribed by Laplace's equation subject to appropriate boundary conditions at the free surface.

If we are considering fluid motion near a free surface $z = \eta(x, y, t)$, the forces on an element of the free surface must balance. If the fluid is considered to have constant surface tension τ, then the normal force balance on the surface yields [6]

$$P_\eta + \tau\left(\frac{1}{R_x} + \frac{1}{R_y}\right) = P_{atm} \tag{1.4}$$

where P_η is the pressure in the fluid evaluated at the free surface and R_x and R_y are the radii of curvature of the free surface in the x and y directions, respectively, with positive curvature concave upwards. Equation 1.4 shows that the pressures on the two sides of the surface are equal except for a capillary pressure term.

Evaluating Bernoulli's equation at the free surface, making use of equation 1.4 and rearranging yields a *dynamic boundary condition* at the free surface, namely

$$\left[\frac{\partial\phi}{\partial t} + \frac{\nabla\phi\cdot\nabla\phi}{2}\right]_\eta + g\eta - \frac{\tau}{\rho}\left(\frac{1}{R_x} + \frac{1}{R_y}\right) = 0 \tag{1.5}$$

Using U and L as velocity and length scales, respectively, we can write equation 1.5 in nondimensional form as

$$\left[\frac{\partial\phi}{\partial t} + \frac{\nabla\phi\cdot\nabla\phi}{2}\right]_\eta + \frac{1}{Fr}\eta - \frac{1}{We}\left(\frac{1}{R_x} + \frac{1}{R_y}\right) = 0 \tag{1.6}$$

where all the quantities are now nondimensional. The nondimensional groups in

equation 1.6 are the *Froude number* $Fr = U^2/gL$ and *Weber number* $We = \rho U^2 L/\tau$. Equation 1.6 shows that for large length scales ($Fr \to 0$) the gravity term is dominant, while for small length scales ($We \to 0$) capillary forces are most important. The two effects are of the same order near the *gravity-capillary length scale*, $l_{gc} = (\tau/g\rho)^{1/2}$.

Since both ϕ and η are unknown in equation 1.6, it is necessary to have a second boundary condition in order to form a closed system for solving Laplace's equation. This second boundary condition is obtained by noting that fluid particles move with the free surface. The resulting *kinematic boundary condition* is

$$\left[\frac{\partial \phi}{\partial z}\right]_\eta = \frac{\partial \eta}{\partial t} + \left[\frac{\partial \phi}{\partial x}\right]_\eta \frac{\partial \eta}{\partial x} + \left[\frac{\partial \phi}{\partial y}\right]_\eta \frac{\partial \eta}{\partial y}. \tag{1.7}$$

Equation 1.7, along with equation 1.5 and Laplace's equation forms a closed set of equations for the fluid motion. Note that equations 1.5 and 1.7 are evaluated at the free surface, which is unknown *a priori*. One can see that equations 1.5 and 1.7 are greatly simplified if they are evaluated at the undisturbed water surface and if we ignore the nonlinear terms. The conditions for this simplification are met when $\nabla\phi$ and $\nabla\eta$ are small, e.g. when the amplitude of the wave motion is small in comparison to the wavelength [7]. We can define a *slope parameter* $\epsilon = ak$ where a is the wave amplitude and k is the wavenumber $k = 2\pi/\lambda$, where λ is the wavelength. For $\epsilon \ll 1$ or infinitesimal waves, the wavemotion is said to be *linear*. When the wave amplitude is finite, the resulting wave motion is said to be *nonlinear*. As we shall see, the interplay between gravitational, capillary and nonlinear effects is very important in controlling the surface wave dynamics.

1.2 Pure gravity waves

For the case of pure gravity waves (i.e. $\tau = 0$) it can be shown that, for small amplitude (i.e. $\epsilon \ll 1$), solutions of the form $\eta = acos(\mathbf{k} \cdot \mathbf{x} - \omega t)$ are possible. Here $\mathbf{k}$ is the wavenumber vector, $\mathbf{x}$ is the position vector and ω is the angular frequency, $\omega = 2\pi/f$. For waves over a flat impermeable bottom, in order to satisfy the free surface boundary conditions and Laplace's equation, ω and k must be related by the *linear dispersion relation* [8]

$$\omega^2 = gk \tanh(kH) \tag{1.8}$$

where H is the total depth of the fluid. For the case where the fluid depth is much larger than the wavelength (i.e. $kH \to \infty$), the gravity-wave phase-speed c_p ($\equiv \omega/k$) is $c_p = (g/k)^{1/2}$ so that longer wavelength (smaller k) waves propogate faster than shorter wavelengths. While this dispersion relation is derived for the case of linear gravity waves, nonlinear effects only slightly modify this relation so that, to a good degree of approximation, the linear theory can often be used.

For pure gravity waves of *finite* amplitude, the free surface begins to deviate from a sinusoidal shape. This problem was originally considered by Stokes [7] who showed that for a monochromatic wave train the wave shape formed broader troughs and sharper crests as ϵ increased, approaching a limiting form of a 120° corner flow at the crest (i.e. the "Stokes limit"). Stokes's solution essentially amounts to the appearance of increasingly higher harmonics in the wave profile as the degree of nonlinearity is increased. It has since been shown that real gravity waves are unstable at slopes below the Stokes limit [9], and waves can evolve to "breaking",

with the formation of a fluid jet that issues from the wave crest and then impacts the wave front face. This jet impact encapsulates a large amount of air and some of the energy of the initially irrotational wave is converted into turbulent energy near the free surface, as well as producing spray and bubbles in the breaking zone.

If we are considering waves on deep bodies of water such as lakes and oceans, such steep gravity waves can be generated by a variety of mechanisms. In cases where the free-surface is subject to wind, waves can be driven directly by the wind motion and several models of this process have been proposed, such as the resonance of pressure fluctuations for small amplitude waves [10] or a "sheltering" pressure at larger amplitude [11]. Generally speaking, the energy input rate from the wind to the waves appears to increase with the difference between the wave phase speed and the wind speed. Because of the combined effects of nonlinearity and dispersion, water waves also exhibit a phenomenon known as wave-wave interaction. This idea was first put forth by Phillips [12], [13] who demonstrated that a continuous transfer of energy between different Fourier components of interacting wave fields was possible through a type of resonant interaction at third order in the wave slope. A similar approach was used by Benjamin and Feir [14] who showed that, to second order in the wave slope, a monochromatic wave train is unstable to upper and lower "side-band" frequencies that grow exponentially in time. This wave-wave interaction is a slow process that occurs over many wave periods. Many experiments ([15], [16], [17], [18, 19], [20], [21]) and numerical calculations [22] have confirmed the existence of these unstable side-bands, as well as observing that the initially uniform wave train degenerates into wave groups as the process develops. The steepness of individual

wave crests increases as a wave moves through these groups and for significantly modulated wave trains the waves can break.

1.3 Capillary effects

When we begin to consider capillary effects on surface waves, some interesting dynamics begin to emerge. First, it can be shown that with surface tension, the dispersion relation (equation 1.8) is modified to include a capillary dispersion term [8]

$$\omega^2 = \left(gk + \frac{\tau}{\rho} k^3 \right) \tanh(kH). \tag{1.9}$$

As was mentioned in section 1.1, water waves are typically considered to be inviscid, though in reality there is a small viscous layer that forms near the free surface with a thickness on the order of $\delta = (2\nu/\omega)^{1/2}$ where ν is the kinetmatic viscosity ($\equiv \mu/\rho$). The inviscid assumption therefore requires that the quantity $k\delta \ll 1$[1]. One can use equation 1.9 to convince oneself that, in deep water, such a condition is adequately satisfied for all but the smallest of waves ($\sim$ 1 mm or less). As the wave steepness increases viscous effects can begin to play a role [23], but to leading order in the wave slope the inviscid approximation is often sufficient. In the experiments discussed herein, the waves are considered to be inviscid, except for the discussion on gravity-capillary solitary waves in Chapter 4, where recent theoretical models show the inclusion of viscous effects to be important in capturing the qualitiative surface features observed in the experiments.

[1]The quantity $k\delta$ can also be thought of in terms of the Reynolds number based on the gravity wavelength and phase speed. This is because $k\delta = (2\nu k^2/\omega)^{1/2} = (\frac{4\pi\nu}{c\lambda})^{1/2}$, $k\delta \propto 1/\sqrt{Re}$.

Dividing both sides of equation 1.9 by k^2 and using the fluid depth H as a length scale and $U = (gH)^{1/2}$ as a velocity scale, we can write an equation for the dimensionless phase speed c'_p as

$$c_p'^2 = \left(1 + Bok'^2\right) tanh(k') \tag{1.10}$$

where the primes denoted dimenless quantities and Bo is the *Bond number* $Bo = \tau/(\rho g H^2) = l_{gc}^2/H^2$. $Bo = 0$ corresponds to the deep-water limit while $Bo \to \infty$ is the shallow-water limit. An interesting feature of this dispersion relation is that the phase velocity, c_p, obtains a minimum that depends on the value of the Bond number. For $Bo \gg 1/3$ (shallow water), the minimum occurs in the long-wave limit, $k_m = 0$, and has a minimum phase speed $c_{min} = (gH)^{1/2}$. For $Bo \ll 1/3$ (deep water), the minimum occurs at a finite wavenumber, $k_m = (\rho g/\tau)^{1/2}$, with minimum phase speed $c_{min} = (4g\tau/\rho)^{1/4}$. For deep water with a surface tension of 73 dynes/cm, $c_{min} \approx 23$ cm/s. The importance of such phase-speed minima can be seen by taking the derivative of c_p with respect to k, namely

$$\frac{dc_p}{dk} = \frac{d\omega/dk}{k} - \frac{\omega(k)}{k^2} = \frac{1}{k}(c_g - c_p) \tag{1.11}$$

where c_g is defined to be the group, or energy velocity $\partial\omega/\partial k$. At any extrema, $dc_p/dk = 0$, and equation 1.11 shows that $c_p = c_g$ at this point. Extrema of $c_p(k)$, where the phase and group velocities are equal, are known bifurcation points of non-linear solitary waves [24], [25], [26], [2], [27], [28]. In fact, similar such solitary waves have been observed in other areas of physics [29], [30], [31], and research into the wave behavior near such minima offers new insight into the physics of nonlinear waves

in dispersive media. Therefore, recent experiments on the generation of gravity-capillary solitary waves will be discussed in Chapter 4.

In addition to altering the dispersion relationship, capillary forces can also affect the dynamics near the crests of steep gravity waves, where the curvature of the free surface is high. For gravity wavelengths typically less than about 1 m, the crest jet found in long-wavelength breaking waves may be replaced by a rounded bulge and capillary waves on the front wave face [32], [33]. In such cases, the breaking process is triggered by the appearance and growth of a small separated shear layer near the free surface [34, 35, 36]. This small turbulent patch is driven downwards by gravity and "spills" down the front wave face, generating capillary-scale ripples on the free surface. Although they lack the significant air-entrainment of their larger wavelength counterparts, these "micro-breakers" [37] are prevalent on the ocean surface under typical conditions and are known to play an important role in processes in the upper ocean such as air-sea interaction and energy dissipation [38, 39, 40, 41, 42, 43, 44], as well as effecting remote sensing devices through the generation of small-scale surface ripples [45, 46, 47, 48]. Because of their ubiquity and importance in such areas, Chapters 2 and 3 will discuss two experiments looking at the effects of surface tension on short-wavelength spilling breakers.

1.4 Thesis outline

Needless to say, research on nonlinear waves and capillary flows extend well beyond the topics of wave breaking and gravity-capillary solitary waves, and the

above discussion is meant to highlight just two fluid dynamic examples of ways in which capillary forces can affect wave dynamics on a free surface. However, the importance and applicability of these flows to areas of fluid mechanics, physical oceanography and nonlinear wave theory makes them a topic worthy of scientific inquiry, the results of which could contribute in a variety of disciplines. While this section is designed to give an introduction to the overarching physics of the problem, the remainder of this dissertation will focus on relevant background and experiments related to three specific topics. The first two topics are similar in nature, and are both related to the effects of surface tension on the dynamics of short-wavelength breaking waves. Chapter 2 is an investigation of the streamwise wave shape at the point of incipient breaking. Emphasis is placed on how the capillary-induced crest geometry changes with both the wavelength and the method used to generate the wave, and what these results might contribute to the development of a breaking criterion for unsteady brekaers. Chapter 3 is concerned with the dynamics of the free surface once breaking begins and focuses on the growth of cross-stream surface fluctuations, which are dominated by the interaction of capillary-forces with the turbulent structure in the underlying fluid. The third topic, discussed in Chapter 4, examines the generation of non-linear capillary-gravity solitary waves near the minimum phase speed. Experimental results are presented that show how such waves may be excited by the motion of a small pressure source on the free surface, and several distinct response states are found. Chapter 5 provides a summary of the work and conclusions.

Chapter 2

Streamwise profile measurements of spilling breakers at incipient breaking[1]

2.1 Abstract

In this set of experiments, the profiles of incipient spilling breaking waves with wavelengths ranging from 10 to 120 cm were studied experimentally in clean water. Short-wavelength breakers were generated by wind while longer-wavelength breakers were generated by a mechanical wave-maker using either a dispersive focusing or side-band instability mechanism. The crest profiles of these waves were measured with a high-speed cinematic laser-induced fluorescence technique. For all the wave conditions reported herein, wave breaking was initiated with a capillary-ripple pattern as described in [1]. The results show that several geometrical parameters used to describe the crest change with the relative wavelength of the wave, but remain insensitive to the breaker method used. Although the crest shape does vary, it is found to be self-similar with two geometrical parameters that depend only on the slope of a particular point on the front face of the gravity wave. The scaling relationships appear to be universal for the range of wavelengths studied and hold for waves generated by mechanical wave-makers and by wind. The slope measure is found to be dependent on the wave phase speed and the rate of growth of the crest

[1]Some of the work presented in this chapter can also be found in Diorio *et al.*, *Journal of Fluid Mechanics*, 2009 [49]

height prior to incipient breaking.

2.2 Summary of previous work

As was discussed in Chapter 1, surface tension plays an important role in short wavelength and/or weak breakers causing the formation of a rounded crest and capillary waves appearing on the front wave face. This phenomenon has been investigated over the years through a combination of experiments, theories and numerical calculations. Some of the earliest works were by Schooley [50] and Cox [51], who reported on measurements of high-frequency capillary waves on the front face of gravity waves in wind-wave flumes. The gravity wavelengths studied were in the range of about 1–10 cm. The measurements in [51] also revealed the presence of these waves even in the absence of wind. Longuet-Higgins [52] produced a theory to explain the existence of these capillary waves, considering surface tension as a small perturbation to the flow inside a steep gravity wave. It was shown that the capillary waves derive their energy from the larger gravity wave, giving rise to the nomenclature of "parasitic" capillary waves. Later, Crapper [53] offered a different theory, considering the case of non-linear capillaries on a variable stream. More observations of small wavelength wind-waves have been reported, although very few measurements of precise wave profiles are available. Okuda [54] used flow visualization to investigate the velocity distributions near the surface of a wind-wave field. The results showed a thickened vorticity layer near the crest of waves whose height was near or greater than the significant wave height. Photographs

of laboratory wind waves reported by [55] showed the presence of a bulge and a train of small capillary waves on the leeward side of the wave crest and streaky patterns on the wind-ward side that were likely due to the high vorticity layer found in [54]. Reference [55] also used the specular reflection of a light source to measure the wavelength of the capillary waves as a function of distance from the crest, and compared these measurements to the theory of [52]. It was shown that there was qualitative agreement between the theory and experiment when the surface drift velocity was taken into account.

Reference [33] calculated the effect of surface tension on the development of a breaking wave generated due to a side-band instability. For wavelengths less than about 0.5 m, a small bulge is formed, and small capillary waves appear upstream of the leading edge. Calculations by Longuet-Higgins [56] on the effect of surface tension on the crest instability of the almost-highest wave showed similar results: a bulge forms on the crest, and a train of capillary waves appears upstream of the toe. A particularly important result of these calculations was that in the presence of surface tension, the non-dimensional length of the bulge L_m/λ (where L_m is the distance from the toe to the point of maximum height) increases as the wavelength decreases. Improving on his earlier theories, Longuet-Higgins [57] also theorized that the capillary-bulge pattern formed near the crest of steep waves is part of a "capillary jump" system. It was suggested that this jump is connected to the existence of solitary capillary-gravity waves [24], where the height of the wave is related to the phase speed. If the fluid particle speed upstream of the jump exceeded $1.414(g'\tau/\rho)^{1/4}$, a stream of capillary waves would occur. Here g' is an "apparent

gravitational acceleration" felt by a short ripple riding on a longer gravity wave and is given by $g' = gcos(\theta) - \kappa q^2$, where θ is the angle of tilt of the surface, κ is the local surface curvature and q is the particle speed. In the theory, the wave steepness required to meet such a jump condition decreased with the wavelength of the wave. The jump in height is thought to be located at the point on the wave profile where the gradient in the surface velocity reaches its minimum value. This theory was verified in a semi-quantitative fashion by the calculations of Y. Yao that are included in [57]. In addition to supporting the theory, the numerical calculations showed that the shape and size of the capillary waves scale with $(\tau/\rho g)^{1/2}$ rather than with the length of the gravity wave. Similar profiles were reported in [58] and [59] in computations employing a pressure forcing (to simulate wind) and viscous dissipation. Good agreement with laboratory experiments of mechanically generated waves with lengths in the range of 5-10 cm was also reported.

In detailed experiments, Duncan and colleagues [32, 60, 1] used a photographic technique that employed a laser light-sheet and a high-speed camera to make profile measurements of two-dimensional mechanically generated waves. Very weak breakers with wavelengths in the range of 80–120 cm were investigated in this study. For these waves in clean water, a bulge-capillary wave system formed on the forward face of the wave crest, even though the wavelengths were relatively long. These profiles were qualitatively similar to the profiles computed by Longuet-Higgins [23, 57, 56] and Tulin [33] for times up to just before the wave began to break. In [1] the crest profiles just before the onset of turbulent flow were found to be independent of wave frequency, giving further evidence that the crest flow is dominated by gravity and

surface tension in weakly spilling breakers, and should scale with $(\tau/\rho g)^{1/2}$. The experiments of Duncan *et al.* also qualitatively highlighted the breaking process and the production of turbulence. A short time after the formation of the bulge-capillary system, the toe begins to move down the front face of the wave, and longer turbulent ripples replace the bulge and capillary waves. This turbulent patch grows in size and eventually covers a significant portion of the wave crest. Particle image velocimetry (PIV) measurements reported in [36] revealed the presence of vorticity near the toe of the wave just as the toe started to move down the wave front face. The size of this vortical region increased as the toe progressed. It was theorized [23] that the capillary waves upstream of the toe are a substantial source of vorticity that may be advected into the crest region, although the boundary layer thickness proposed in this theory was too thin to be verified in [36]. In another experiment [61] wave-height gauges were used to measure the wave slope close to the crest of "near-breaking" wind waves and found the slope to be independent of the wavelength, indicating a self-similarity in the asymmetric profile shape. The same similarity was found even for waves generated mechanically. The authors used this result to imply that beyond a certain point of the wave evolution, the breaking process is controlled by factors other than the wavelength or the wind speed. These results, combined with the numerical and experimental observations that 2-D breakers scale as $(\tau/\rho g)^{1/2}$, lend evidence that the crest profile shapes for breaking wind waves should also be scale invariant, depending only on the surface tension and gravity. However, no detailed measurements exist to fully support this claim.

Clearly, the wave shape and flow field at the moment before breaking begins are

critical aspects of breaking waves. However, a general incipient breaking condition for unsteady waves has been elusive, and the most successful work has been with steady waves. This work began with Stokes [7] who showed that the limiting form of the crests of a steady periodic gravity wave train is a corner flow with an included angle of 120° and a stagnation point at the crest. In [62] it was found that steady waves produced by towing a two-dimensional hydrofoil at constant depth, angle of attack and speed would continue to break once disturbed if the slope of the wave's forward face was greater than 17°. The stagnation point idea was also used by Banner and Phillips [37] in considering the effect of a surface wind drift layer on the breaking criterion for a steady wave. In experiments with hydrofoil produced waves and a turbulent surface wake [63], it was found that the breaking criterion had the same functional form as in the Banner and Phillips theory, but was reached when the flow speed at the crest was 50 percent of the wave phase speed. Work to determine a breaking criterion for unsteady waves has been less successful. This is partly because the wave goes through a range of shapes as it breaks and both the theory and the experiments are more difficult than in steady waves. Recent work in this area includes [64], [65] and [66] which focus on waves breaking within modulating wave packets. These studies emphasize the role of the rate of increase of energy at the maximum height of the wave packet envelope on the breaker type (spilling to plunging). Also, [67] found through numerical calculations that in deep-water modulating gravity wave trains, a wave crest will evolve quickly to breaking whenever the local maximum particle speed exceeds one-half the phase velocity of the dominant wave train. The relationship between this latter breaking criterion for

unsteady waves and that of [63] for steady waves is not known, even though both occur when the particle speed reaches one-half the wave phase speed.

In view of the previous work discussed here, one of the goals of the current work is to measure the crest shape for spilling breakers at incipient breaking for a range of breaker wavelengths and under a variety of breaking conditions. Results of such experiments would offer insight into the breaking process, including testing the appropriateness of the crest scaling length $(\tau/\rho g)^{1/2}$ and aiding in the development of a general incipient breaking criterion for unsteady waves. Therefore, the results of 2D profile measurements for various waves generated by different techniques, including wind, are presented in this chapter.

2.3 Experimental details

2.3.1 The wave tank

The experiments were carried out in a wind-wave tank that is 11.6 m long by 1.22 m wide and 2.1 m tall with a water depth of 0.91 m, see figure 2.1. The tank includes a programmable wave-maker that spans the width of the tank with a vertically oscillating wedge with a wedge angle of 30 degrees. The wedge is located at one end of the tank and mounted to the laboratory wall. A servo-motor, which is controlled by a PC, can drive the wedge vertically while a position sensor monitors the current wedge location. The position information is fed back into the servo-motor to actively correct any errors in the motion. This feed-back system controls the wedge position to within a run-to-run rms error of $\pm 0.1\%$. The facility also

features an instrument carriage which rides on top of the tank. This carriage is supported by four hydro-static oil bearings to reduce vibrations on the tank walls and is towed by a towing cable cranked via a second servo-motor. A second position sensor monitors the location of the carriage, also providing feedback to the carriage motor. The same PC controls both the wedge and carriage motors so accurately coordinated motions between the two can be obtained.

The tank also includes a wind tunnel which is positioned in front of the wave-maker. The tunnel is powered by two 5.6 kW fans that are mounted to the ceiling of the laboratory and drive air toward the wave-maker. An entrance section consisting of ducting, two sets of turning vanes, three screens and a honeycomb is used to condition and redirect the air flow so that it moves parallel to the water surface in the direction away from the wave-maker. Measurements of the mean air flow leaving the entrance section were made using a pitot tube and it was found that the mean air velocity varied by less than 7% over the cross section of the tank at the fastest fan speed. After passing through this entrance section, the airflow is contained by the side walls of the water tank, a series of clear Acrylic plates that form the lid, and the water below. The lid plates are positioned 0.78 m above the mean water level and end 1 m before the end of the tank to allow the air to exit. The bottom of the entrance section of the wind tunnel is 10.2 cm above the mean water level. This gap allows waves generated by the wave-maker, which is located behind the entrance section, to enter the tank. The area between the wave-maker and the back of the wind tunnel is sealed with flexible material in order to minimize reverse air flow under the entrance section. The mean air-speed at a point halfway down the

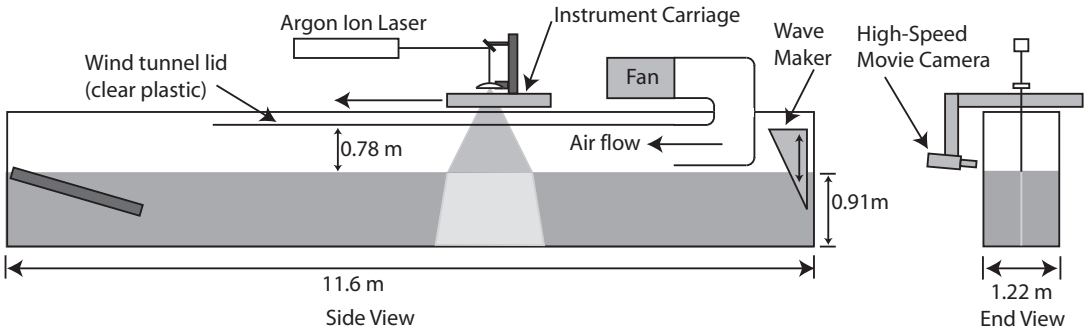

Figure 2.1: Schematic of wave tank with wave-maker, wind tunnel and instrument carriage.

tank was measured with a pitot tube and the maximum value was found to be about 9.1 m/s (or about 18 knots).

At the far end of the tank, a small beach comprised of a horse-hair mat on a tilted Acrylic plate was placed below the wind tunnel exit to damp wave reflections. When the wedge is used to produce waves, the breaking process occured before any waves reflected back into the measurement area. When the wind is on, the driving force of the wind quickly damps any upstream travelling wave reflections, in addition to the damping effect of the beach. The measurement section is also kept far enough away from the beach that the effect of reflected waves is negligible.

Because of the importance of surface tension in these experiments, a combination of a surface skimmer and a diatamacious-earth water filtration system is used to keep the surface free of any contaminants and surfactants. For waves generated mechanically, this filtration system is kept on in between runs, typically about 30 minutes. For these waves, a custom-built Langmuir trough is placed in the tank and surface tension measurements are made *in situ* using a Willhelmy plate. For the wind-wave experiments, the Acrylic plates that form the lid of the wind tunnel

make *in situ* measurement infeasible, so a small bench top tank was constructed for measuring the surface tension. First the surface is skimmed for at least an hour before the wind is turned on. Once the wind is turned on, and before any experiments begin, a sample of water is taken from the bulk near the exit of the wind tunnel and placed in the bench top tank. The surface tension is then measured using the same Langmuir trough-Willhelmy plate device mentioned above. In all of these experiments, the surface tension was measured to be 73 dynes/cm and the water was considered to be relatively free of any surfactants.

2.3.2 Wave generation

Waves were generated using three different methods. The first method was a dispersive focusing technique similar to that used in [68]. Briefly, in this method a packet of waves with varying frequency is generated in such a manner that the packet converges as it travels down the tank. This convergence causes the remaining waves in the packet to increase in amplitude, and a breaking wave may form if the initial amplitudes are large enough. Linear deep-water gravity wave theory is used to compute the motion for the wave-maker, though the resulting wave motion is highly nonlinear when the packet converges. The wave packet consists of the sum of N sinusoidal components and the wave-maker motion to produce these waves is given by

$$z_w = w(t)\frac{2\pi}{N}A\sum_{i=1}^{N}\frac{1}{k_i}cos\left(x_b\left(\frac{\omega_i}{\bar{c_g}} - k_i\right) - \omega_i t + \phi\right) \tag{2.1}$$

Case No.	No. of runs	$\bar{f}(Hz)$	$\bar{\lambda}(cm)$	$A/\bar{\lambda}$
1	3	1.15	118.06	0.0505
2	1	1.26	98.34	0.0505
3	1	1.42	77.43	0.0505
4	1	1.42	77.43	0.0496
5	1	1.42	77.43	0.0487

Table 2.1: The parameters of the five wave-maker motions used with the dispersive focusing technique. In this table, $\bar{f}$ is the average frequency of the wave packet, $\bar{\lambda} = g/(2\pi\bar{f}^2)$ is the wavelength of the average frequency according to linear theory, and $A/\bar{\lambda}$ is the non-dimensional amplitude of the wave-maker motion. Note that the first case was done three times, yielding seven experiments total. The value of the other parameters used in equation 2.1 are as follows: $N = 32$, $x_b = 6\bar{\lambda}$ and $\phi = 90°$. The windowing function $w(t)$ is described in [1].

where A is an adjustable constant called the wave-maker amplitude, x_b is the horizontal position of the breaking event, t is time, k_i and ω_i are the wavenumber and radian frequency of each component, $\bar{c_g}$ is the average of the group velocities of the N wave components, and ϕ is a phase shift, typically taken to be $\frac{\pi}{2}$. w is a windowing function that is designed to give the wave-maker zero motion when the sum of the components results in very small motion (see [1] for further details). For each motion, we can define an average wavepacket frequency $\bar{f}$ and a non-dimensional wave-maker amplitude $A/\bar{\lambda}$, where $\bar{\lambda} = g/(2\pi\bar{f}^2)$ is the wavelength of the average frequency. Five different wave-maker motions were studied with this technique and the values of the parameters used can be found in table 2.1.

In the second method, the wave-maker is used to generate a sinusoidal wave

train of initial frequency f_0 and initial slope a_0k_0, where a_0 is the wave amplitude (different from the parameter A above) and k_0 is the wavenumber according to linear theory. The amplitude a_0 is the average height of the waves produced by a given wave-maker motion, and is measured 5 m away from the wave-maker using a capacitance-type wave height gauge. According to the theory of Benjamin and Feir [14], a sinusoidal gravity wave train is unstable to upper and lower "side-band" perturbations with frequencies in the range $f_\pm = f_0(1 \pm \sqrt{2}a_0k_0)$, with the fastest growing instability located at $f_\pm = f_0(1 \pm a_0k_0)$. These side-band frequencies interact with the main carrier wave, causing an initially uniform wave train to modulate into wave groups. If the envelope of these groups is sufficiently steep, waves may begin to break as they pass through the group. This theory has since been slightly modified to include a parameter β, such that the fastest growing instabilities are located at $f_\pm = f_0(1 \pm \beta a_0k_0)$, where the value of β is dependent on the wave slope and the specifics of the wave-maker [69], [16], [18]. In our facility, waves were first generated with the primary component only and the frequency spectra were computed from the measured wave height data. It was found that the fastest growing side-bands were typically located at $f_\pm = f_0(1 \pm 0.75a_0k_0)$ or $\beta = 0.75$. However, the wave tank is not long enough to let these side-bands grow naturally (i.e. more wave periods are needed for the wave train to modulate sufficiently to cause breaking). Therefore, the wave-maker is run again but with the side-band frequencies superimposed on the main wave train at an amplitude γa_0 where $\gamma \ll 1$. The values of the parameters used with this method are summarized in table 2.

In the third method, the wind was used to generate waves. In the conditions

No. of runs	$f_0(Hz)$	a_0k_0	$f_+(Hz)$	$f_-(Hz)$	γ
3	2.3	0.30	2.81	1.79	0.015

Table 2.2: The parameters used for the three waves generated using the side-band instability mechanism. In this table, f_0 is the frequency of the main wave train, a_0k_0 is the measured wave slope, where a_0 is the amplitude of the initially unmodulated sinusoidal wave train measured at a distance of 5 m from the wave-maker using a capacitance probe, and k_0 is determined from f_0 via linear theory. f_+ is the frequency of the upper side-band, f_- is the frequency of the lower side-band, and γ is the ratio of the side-band input amplitudes to the input amplitude of the main wave train.

studied herein, the wind speed at the center line of the wind tunnel ranged from 6.0 to 7.2 m/s and the fetch at the location of the measurements ranged from 3 to 5.5 m from the beginning of the wind-tunnel test section. The wind velocity profile as a function of height above the water surface was measured with a pitot tube, starting 2 cm above the mean water level. An estimate of the friction veloctiy at the water surface was obtained by computing dU/dy at the mean water level via a linear fit to these wind-profile measurements. It was found that $U_\tau \approx 1.8$ cm/s and the waves are considered to be over-driven (i.e. the wave phase speed is much lower than the wind speed at the centerline of the tank). Capacitance-type wave-height gauges were used to measure the dominant wave frequencies under these wind conditions. The peak frequencies ranged from roughly 2.5 to 3.5 Hz, which, via linear theory, yield wavelengths in the range of 10 to 25 cm. In all, measurements for 18 different breakers are reported in this section (7 generated by dispersive focusing, 3 generated by side-band instabilities and 8 generated by wind).

2.3.3 Wave profile measurement

The profiles of the breaking waves were measured photographically with a Laser-Induced-Fluorescence (LIF) method that employs a high-speed digital movie camera. A beam from an Argon-Ion laser operating at 7 W is directed through a series of mirrors to optics that are mounted on the instrument carriage. These optics redirect the light sheet downward and a cylindrical lens spreads the beam into a thin vertical light sheet. This light sheet is located at the center plane of the tank and is 25 cm wide (in the streamwise direction) and 1 mm thick (in the cross-stream direction) at the mean water level. In order to make the light sheet visible at the water surface, Fluorescene dye was mixed into the tank water. A high-speed camera (Phantom v9, Vision Research), mounted on the side of the carriage, images the intersection of the laser sheet and water surface from the side and slightly above and in front of the wave crest. Images of a patterned checkerboard placed in the plane of the light sheet were used to calibrate the camera images and to test for any parallax error caused by the slight viewing angle. The camera was set to record 1632-by-1200 pixel images with 8 bit grey levels at 250 images per second. Because the optics that form the light sheet and the camera are mounted to the carriage, images can be taken of the breaking wave crests as they propagate down the tank. The camera runs on an internal clock and is triggered by the start of the wave-maker (which also triggers the start of the carriage motion). For the cases with mechanically generated waves, the carriage motion was synchronized with the wave motion by trial and error by varying the carriage starting position, the starting

time relative to the wave-maker motion, the acceleration and the final speed from run-to-run. For cases where the wind was used to generate waves, the approximate phase speed of the waves was determined at the fetch of interest and the carriage was run repeatedly at this speed. A run was considered successful when a wave was seen to break in the camera's field of view. It is emphasized that the geometrical and propagation characteristics of breaking wind waves measured at the same wind speed and fetch vary from one event to another.

Wave crest profiles were extracted from each image by use of a MATLAB routine consisting of a series of steps. First a threshold function is applied to convert low gray levels to black and high gray levels to white to create a uniform dark background and enhance image intensity. Next, the gradient of the image intensity field in both the x and y directions was obtained by applying a centered difference mask at each pixel. A threshold is applied to this gradient image to create a binary image where high magnitude gradients are considered edge pixels and assigned a value of 1 (white) and all other pixels are assigned a value of 0 (black). This binary image shows no edge pixels in the air but many edge pixels from the water surface downwards, particularly at the air water interface. Lastly, starting from a surface edge pixel at the far left of the image, the program searches the nearest neighbor pixels in a clockwise fashion to find other edge pixels that are to the right of the starting pixel. If another edge pixel is found, the program joins consecutive pixels and the process continues, snaking the edge of the image from left to right. Due to the high resolution of the camera and the presence of bright and dark spots cause by surface curvature, this technique can sometimes lead to spurious edges or

gaps in the profile. This problem is fixed by allowing certain pixels of the profile to be manually inserted or removed by the user. The accuracy of the wave profile depends on the quality of the image and the resolution of the camera. Different camera lenses with various magnifications were used depending on the desired field of view (wider angle lenses tended to be used for the wind-wave experiments so as to capture more potential breaking events). In the well-focused images prior to breaking, the free surface can typically be located to within one pixel, which was 0.3 mm in the physical plane for the lowest magnification used.

2.4 Results and discussion

2.4.1 Crest geometry

Figure 2.2 contains LIF images of the crest region of three waves at the point of incipient breaking (defined as the last frame before the toe point begins to move and referred to as $t = 0$ herein) during three different experiments. The images have been cropped to show a 5-by-2-cm region near the wave crest and all the waves are moving from right to left. The wave in figure 2.2(a) was generated using the dispersive focusing technique, and has an average wavelength $\bar{\lambda}$ of roughly 120 cm and an amplitude of 8 cm as measured from the undisturbed water level to the crest. The wave in figure 2.2(b) was generated by the side-band instability method and has a wavelength $\lambda_0 = 2\pi/k_0$ of roughly 30 cm and an amplitude of 1.8 cm. The wave in figure 2.2(c) was generated directly by the wind and has a wavelength of approximately 13 cm (as measured by the high-speed camera) and a crest height

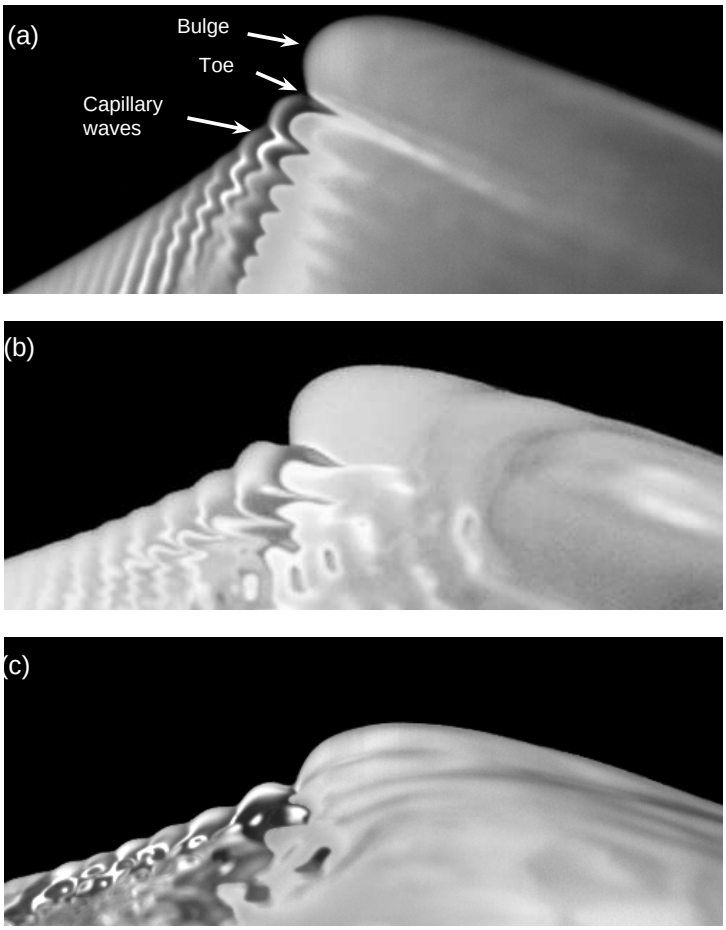

Figure 2.2: Images of wave crests at incipient breaking from high-speed movies in three separate experiments. Each image shows a 5 cm x 2 cm section near the wave crest, and the waves are moving from right to left. Each wave was generated using a different method and has a different wavelength (λ) and amplitude (a). a) Dispersive focusing, $\bar{\lambda} = 120$ cm, $a = 8$ cm. b) Side-band instability, $\lambda_0 = 30$ cm, $a = 1.8$ cm. c) Wind-driven, $\lambda = 13$ cm, $a = 0.7$ cm. The wavy boundary between the black region at the top of each image and the non-uniform grey region below is the wave crest profile at the intersection of the light sheet and the water surface. The light and dark patterns seen below this boundary are the result of two refraction processes: the first as the light sheet enters the water creating a non-uniform pattern in the fluorescing dye and the second as the non-uniform light intensity in the glowing dye within the light sheet is viewed through the water surface between the camera and the light sheet.

of 0.7 cm above the mean water level in the tank before the wind was turned on. As can be seen from the figure, a capillary-bulge pattern appears in all the images (see figure 2.2(a) for nomenclature). This pattern includes a round bulge formed on the forward (left) face of the wave crest and a train of capillary waves upstream (to the left) of the leading edge (toe) of the bulge, as described in section 2.2. At the instant in time after the images shown, the toe, which was stationary relative to the wave crest prior to these images, begins to move down the wave face and a turbulent flow ensues, see [1] and [36].

Figure 2.3(a) shows the wave crest profiles taken from the images in figure 2.2. In this plot, the profiles are aligned at the toe point to remove the large differences in wave crest height and thereby allow better comparison of the crest profiles. As can be seen from the figure, though the shape of the profiles are qualitatively similar, the variations in the slopes of the free surface upstream of the toe and the curvature of the bulge are quite pronounced. Generally speaking, both of these quantities increase with the wavelength of the breaking wave. This trend in local surface slope is qualitatively similar to the theory of [57]. In this theory, a capillary jump, which forms the capillary-bulge system, occurs at the point on the wave profile where the flow speed in the reference frame of the crest equals the minimum phase speed of capillary-gravity waves and the gradient of the flow speed at the surface is high. In [57] it was shown that the surface slope at this point decreases with decreasing gravity wavelength. The profile shapes shown in figure 2.3(a) are also qualitatively similar to those found in numerical calculations of short-wavelength steep waves [70], [58], [59], [33] and [56].

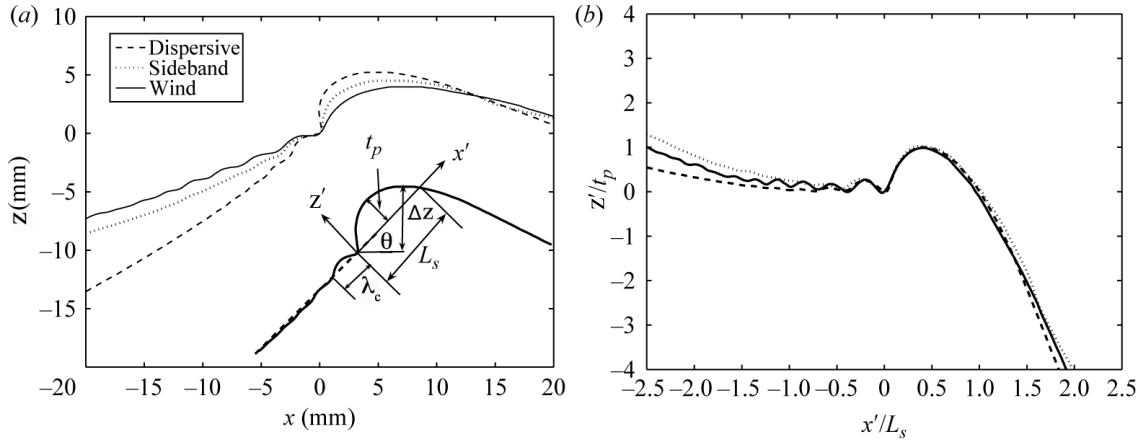

Figure 2.3: Crest profiles of the three waves shown in figure 2.2. (a) After aligning the profiles at the toe point. (b) After rotating each profile so that the slope of the front face at the toe is horizontal, and scaling the horizontal and vertical axes by L_s and t_p, respectively (see insert in (a)).

In order to compare the profile shapes quantitatively, a few geometric parameters are defined. These parameters include the vertical distance (Δz) from the maximum height of the profile to the toe point, the length of the first capillary wave (λ_c) upstream of the toe, a mean surface slope at the toe (m), a bulge length (L_s) and a bulge thickness (t_p), see the inset in figure 2.3(a). In order to obtain values for m, a polynomial (anywhere from 2nd to 4th order) was fit to the front wave face from the toe to a point 3 cm upstream of the toe. This polynomial was forced to pass through the toe point which is defined numerically as the point in the profile with maximum upward curvature. The purpose of this polynomial is to follow the overall shape of the front face of the gravity wave near the crest, while ignoring the undulations due to the capillary waves. A typical fit is shown in the inset of figure 2.3(a). The slope of this polynomial at the toe point is then chosen as $m = \tan\theta$ (see the inset in figure 2.3(a) for the definition of θ). The values of m measured in

this study were found to be between 0.3–1.5, which correspond to $\theta = 17$–56 degrees (note that θ at the crest of a limiting form Stokes wave is 30 degrees). The length of the bulge, L_s, is defined as the distance from the toe to the crest profile following a straight line with slope m. The bulge thickness t_p is defined as the maximum perpendicular distance from the line forming L_s to the surface of the bulge.

Using the parameters m, L_s and t_p measured for each wave at incipient breaking, the crest profiles are plotted in figure 2.3(b) in the local scaled coordinate system $X'/L_s - Z'/t_p$ where X' is directed from the toe along the line L_s and Z' is perpendicular to X'. When viewed in this non-dimensional way, the similarity of the profiles in the crest region is quite striking, considering the large differences in gravity wave amplitude, wavelength and generation method. The scaled crest profiles for all the other incipient breaking waves studied herein are similar to these, but are not shown here in order to make the plot clearer. Instead, a plot of the average scaled profile and the standard deviation distribution computed from all 18 waves is shown in figure 2.4. The mean profile has a single maximum at $X' \approx 0.42 L_s$ and goes to zero at $X' = 0$ and L_s. The standard deviation reaches a peak of 12% on the front face of the wave; however, careful analysis of the processing techniques indicates that much of this variation can be attributed to the selection of the incipient breaking image frame and the toe position. The precise image frame when breaking begins is difficult to define because it is the frame before the toe starts moving from rest. Thus, its initial motion between frames is quite small. The toe position is taken as the point of maximum upward curvature of the profile. While its determination is done with a consistent numerical procedure, the result is sometimes a little off the

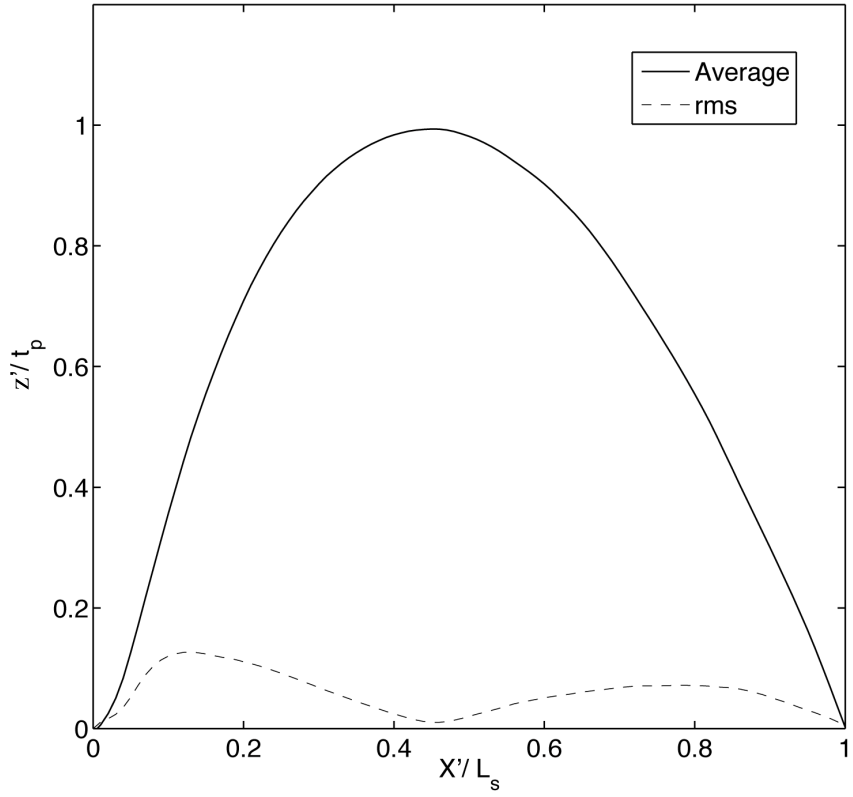

Figure 2.4: Average and standard deviation of the scaled and rotated bulge profiles for all 18 waves studied herein. A 3rd order polynomial of the form $Z'/t_p = p_1(X'/L_s)^3 + p_2(X'/L_s)^2 + p_3(X'/L_s) + p_4$ was fit to the averaged data with coefficients $p_1 = 2.143, p_2 = -7.297, p_3 = 5.253$ and $p_4 = -0.08123$.

position one might choose by eye. The primary effect of changing both the incipient breaking image frame and the toe position is a slight horizontal shift of the peak in the profile. This results in a right-left shift of the nearly vertical parts of the profile near $X'/L_s = 0$ and 1, thus creating the large standard deviations there.

The parameters L_s and t_p are plotted versus m in figures 2.5(a) and (b), respectively. As can be seen in figure 2.5(a), the data appear to follow a single curve, independent of the method used to generate the wave. The curve has a negative slope that decreases with increasing m. The values of t_p (figure 2.5(b))

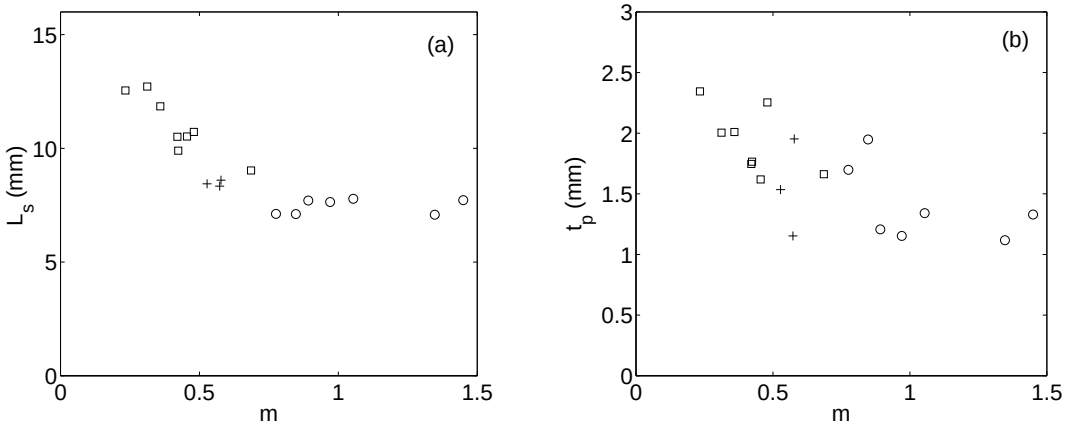

Figure 2.5: Plots showing the variation of (a) L_s and (b) t_p with the local slope parameter, m. $\square$ wind waves, $+$ side-band waves, and $\circ$ focused waves.

show a fair amount of scatter but generally t_p decreases with increasing m. This scatter is primarily because t_p is a very small quantity that changes rapidly as the waves approach breaking and because errors in the measurement of the slope m cause changes in t_p.

In the numerical calculations for steady waves ($\lambda \approx 0.5$ m) in a liquid with a very high surface tension (9 and 16 times the surface tension of water) presented in [57], the shape of the bulge and, of course, lengths describing the capillary-ripple system, scale only with the gravity-capillary lengthscale $(\tau/\rho g)^{1/2}$, see figure 18 in [57]. A similar result was found in the experiments of [1] for unsteady mechanically generated breakers with wavelengths ranging from 70 to 118 cm, see their figure 23. In contrast, the present results, which cover a wide range of wavelengths and a single value of $(\tau/\rho g)^{1/2}$, indicate that L_s and t_p increase substantially as m decreases. However, it should be noted that at the higher values of m, where the wavelengths are the same as those studied in [1], L_s and t_p are relatively constant.

Using the measured Δz data, estimates to the underlying flow speed at the toe point q_t were obtained by using the steady Bernoulli equation (see equation 1.3) and by assuming that there is a stagnation point at the crest of the wave. While the flow is clearly unsteady and there is no experimental verification of the stagnation point at the crest, the above result is used here in an attempt to gain some understanding of the flow and capillary waves. The result is $q_t = \sqrt{2g\Delta z}$. A plot of the estimated values of q_t versus wave slope m is shown in figure 2.6(a). A linear fit to the data yields a y–intercept of roughly 25 cm/s. This last result is rather interesting because on a flat water surface (i.e. $m = 0$) a train of (linear) gravity-capillary waves has a minimum phase speed of roughly 23 cm/s (see Chapter 1). This means that, in a frame of reference moving with the wave train, the underlying fluid speed is 23 cm/s. In a similar vain, the results here imply that as the wave slope approaches zero (i.e. flat water) the underlying fluid speed at the point where the capillaries form is roughly equal to this minimum. While by no means rigorous, the results of such a simple estimate to the flow speed near the crest appear to be consistent with what might be expected physically.

When possible, measurements were also made of the wavelength of the primary capillary wave upstream of the toe, λ_c. A plot of λ_c versus m is shown in figure 2.6(b). Due to a lack of spatial resolution and camera angle in some movies, measurements of λ_c are not available for several of the dispersively focused wave cases. The measured values of λ_c range from about 4 to 5 mm, decreasing slightly with increasing m. Because these capillary waves are stationary relative to the crest, the phase speed of these waves relative to still water must equal q_t. Using the estimated values of q_t from

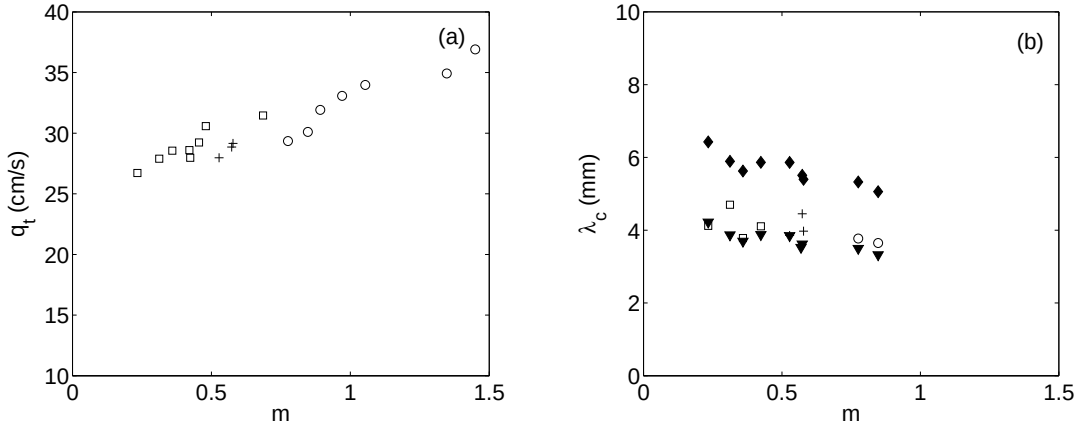

Figure 2.6: Measurements and analysis of the length of the first capillary wave upstream of the toe, λ_c. (a) The flow speed at the toe, q_t (as calculated from the measured Δz and Bernoulli's equation), versus local slope parameter m. The straight line is a least-squares fit to the data. (b) The wavelength (λ_c) of the first capillary wave upstream of the toe versus m. □ wind waves, + side-band instability waves, ○ focused waves, ♦ linear gravity-capillary wave theory, and ▼ nonlinear capillary wave theory (maximum amplitude). Due to a lack of spatial resolution in some images, measurements of λ_c were not made for several of the dispersively focused wave cases.

figure 2.6(a), capillary wavelengths were calculated using both the linear dispersion relationship for gravity-capillary waves ($q_t^2 = c_p^2 = g/k_c + (\tau/\rho)k_c$, where $k_c = 2\pi/\lambda_c$, see Chapter 1), and the non-linear dispersion relationship for capillary waves of maximum amplitude ($q_t^2 = c_p^2 = 0.657(\tau/\rho)k_c$, from [71]). To our knowledge there is no analytical solution for the nonlinear dispersion relationship for gravity-capillary waves of maximum amplitude. The results from these calculations are also shown in figure 2.6(b). As can be seen from the figure, in spite of the approximate nature of the theory, the wavelengths calculated using the linear and non-linear dispersion relationships bracket the measured values of λ_c with the estimates from the non-linear dispersion relationship providing the best estimate. Clearly the approximation for the underlying flow speed at the toe presented here has some physical validity.

2.4.2 The slope parameter, m

The above results have shown the importance of the slope parameter m in determining the wave crest shape at incipient breaking. The next question is: what determines m for a given breaker? Here we explore the hypothesis that m at incipient breaking is a function of both the phase speed, c_p, and the rate of change of the crest height just prior to breaking. The phase speed is chosen because it is related to the wavelength and, as discussed above, it appears on both theoretical and experimental grounds that m decreases with decreasing wavelength. In the present experiments, the wavelengths were typically too large to be measured directly by the high-speed camera, except for some of the wind-wave cases where the wavelength was smaller than the camera's field of view. However, the phase speed was measured directly by determining the speed of the crest as seen in the movies and then adding the known speed of the instrument carriage. The wave phase speeds fell in the range of 50–70 cm/s for waves generated by the wind and the side-band instability mechanism, and from 90–120 cm/s for the waves generated using dispersive focusing.

A useful measure of the rate of change of wave height at breaking is difficult to determine. This is because the rate of change of wave height, while strongly positive in the early stages of the approach to breaking, is close to zero (in some cases even slightly negative) the moment breaking begins for many of the waves. Based on data for the dispersively focused breakers as shown in Appendix A, an average wave crest growth rate $P = [z(0) - z(-0.23T)]/(0.23T)$ is used in the present work, where $z(t)$ is the maximum height of the wave profile at a given time and T is the wave

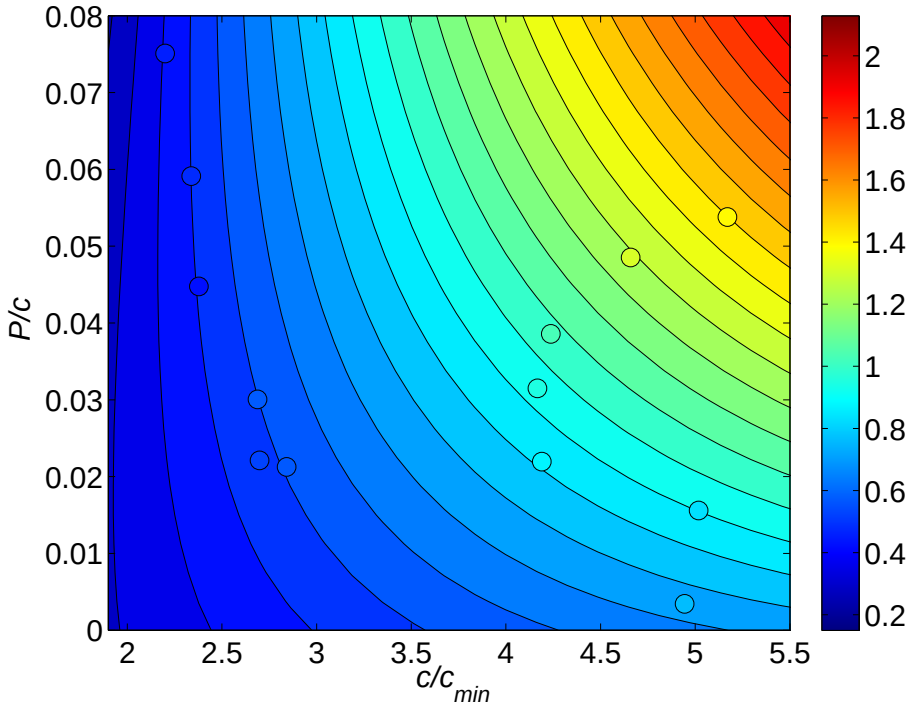

Figure 2.7: Contour plot of the slope m as a function of the dimensionless wave phase speed c_p/c_{min} and the non-dimensional average growth rate P/c_p. The contours are from a least-squares fit of a second-order polynomial, $m = a_1(c_p/c_{min}) + a_2(P/c_p) + a_3(c_p/c_{min})^2 + a_4(P/c_p)^2 + a_5(c_p/c_{min})(P/c_p)$, to the data. The shape of the contours is only supported by the experiments in the vicinity of the data points. The face color of each data point indicates its value of m according to the color legend at the right. Five of the data points for wind waves were not included in these plots because random surface fluctuations or insufficient movie frames prior to breaking prevented obtaining P by the method used here, see Appendix A. The values of the various coefficients of the fit are: $a_1 = 0.14, a_2 = -2.27, a_3 = 0.00, a_4 = -63.60, a_5 = 3.89$.

period. On intuitive grounds, a time of $0.25T$ was desired for this measurement; however, it turned out that $0.23T$ was the maximum value that could be used in the analysis of the largest number of high-speed movies due to the tank side columns. The values of P were then divided by the corresponding values of c_p to give an average dimensionless growth rate, which is essentially the rate of change of wave slope with dimensionless time t/T[2]. The values of c_p were divided by the minimum

[2]That is, $P/c_p = \Delta Ak/\Delta t\omega = \frac{1}{2\pi}\Delta\epsilon/\Delta(t/T)$.

phase speed of gravity-capillary waves, c_{min}. A least-squares fit of a second-order polynomial $m = f(c_p/c_{min}, P/c_p)$ to the data set was performed and the resulting contour plot of m on the c_p/c_{min}-P/c_p plane is given in figure 2.7. The data points on the plot are color coded on the same scale as the contours so that the accuracy of the fit can be estimated from visual inspection. The value of the fit parameters are given in the caption to figure 2.7. The root-mean-square error from the fit is 5.5% of the average of the measured values of m, indicating that the concept that m is a function of c_p and P has some validity. From this plot, it can be seen that for low wave phase speeds (shorter wavelengths) the growth rate has little effect on m, while for the highest phase speeds, m increases significantly with growth rate. This result is in agreement with our intuition that long waves with rapidly increasing amplitude become strong breakers. In particular, plunging breakers were never observed in the wind-generated and side-band instability waves, which have relatively short wavelength, while with appropriate wave generation parameters, plunging breakers (where the local surface slope becomes vertical during the approach to breaking) can be generated at longer wavelengths with the dispersive focusing technique.

The dimensionless crest height growth rate, P/c_p, used here should be distinguished from the parameter μ used by [64], [65] and [66] which is the average dimensionless growth rate of the local energy density at the peak of the wave packet envelope. In those previous works, the parameter μ is related to the evolution of the wave packet envelope while P/c_p is the rate of change of amplitude of a single wave crest as it moves through a packet.

2.5 Summary and conclusions

The crest profiles of spilling breakers with wavelengths in the range of 10–120 cm were investigated experimentally. These waves were generated with a mechanical wave-maker and with wind. It was found that the bulge-capillary wave system that appears on the forward faces of short wavelength spilling breakers is qualitatively similar for all the waves studied herein. The bulge was found to have a self-similar shape where its length and thickness are used as scaling parameters, which in turn are found to be functions of the slope (m) of the mean water surface just upstream of the leading edge (toe) of the bulge. This scaling seems to be independent of wave generation method, leading one to believe that at least some features of mechanically generated and wind waves are quite similar. It was found that m is a function of the wave phase speed c_p and the average growth rate P of the wave amplitude before breaking begins. The data indicate that for the low-phase-speed waves m is independent of P while for the higher-phase-speed waves m increases with increasing growth rate. Finally, estimates of the length of the first capillary wave upstream of the toe that were made. A simple theory based on estimates of the flow speed at the toe and the capillary-gravity wave dispersion relationship compared well with the measured values. The results of this study show that breaking is a multi-scale nonlinear phenomenon in which the local gravity wave (10 to 120 cm wavelength) slope controls the surface-tension-dominated crest shape ($\approx$ 1 cm wavelength). The fact that the scaling parameters are unaffected by wind supports the theory [23] that the dynamics of the capillary-ripple pattern at the crest are dominated by energy

transfer from the gravity wave rather than the wind. The fact that various crest paramaters were found to be dependent on wavelength implies that the concept of using $(\tau/\rho g)^{1/2}$ as a definitive crest length scale should be reinterpreted. Furthermore, our data lend strength to the idea of using wave phase speed and wave growth rate as a breaking criteria, a result which could prove beneficial in more realistic ocean environments.

Chapter 3

Cross-stream profile measurements of unsteady spilling breakers

3.1 Abstract

The results in the previous chapter discussed the shape of the wave crest just prior to breaking and the role of surface tension in altering the wave dynamics. Up until this point in the wave evolution both the underlying flow and the wave profile remain remarkably two-dimensional. However, once breaking begins the formation of near-surface shear layers introduces vorticity into the flow, and the capillary-bulge pattern gives way to a more complex three-dimensional surface ripple pattern. However, little information exists regarding the shape of the surface in the cross-stream direction during breaking, in particular when the scale of the flow (and hence the relative effect of surface tension) is changed. Therefore, in these experiments, the cross-stream profiles of spilling breakers with wavelengths 80 – 120 cm were measured. A mechanical wave-maker was used to generate breakers via dispersive focusing and a cinematic Laser Induced Fluoresence (LIF) technique measured the 2D cross-stream wave profile. The results show the generation of "quasi"-2D streamwise ripples in the breaking zone. However, superimposed on the larger streamwise ripples are smaller cross-stream ripples. In the early stages of breaking these cross-stream ripples are small, but they grow as breaking develops and can be almost equal in amplitude to the streamwise ripples in the strongest

breakers studied. The cross-stream ripples have wavelengths in the range of 1 to 4 cm, a range where capillary forces are important, and their amplitude is found to scale with the breaker wavelength to the third power and linearly with the amplitude of the wave-maker motion. Measurements of various 1D surface gradients show the presence of "scar"-like surface features that appear to be generated in the troughs of the streamwise ripples, indicating perhaps the presence of cross-stream spatial structure. A possible vortical mechanism to help explain these observations is conjectured.

3.2 Summary of previous work

As was discussed in the previous chapter, the effect of surface tension on short wavelength and/or weak breakers is quite profound, with the commonly observed "plunging jet" being replaced by a rounded crest and capillary waves appearing on the downstream wave face. A short time after the capillary-bulge pattern forms at the crest, vorticity appears in the sub-surface flow and the wave quickly transitions to turbulence. This process is most readily seen in the PIV measurements presented in [36] that show the growth of a vortical region near the toe of the crest bulge at the moment breaking begins. The precise source of this vorticity is still unknown, although several interpretations have been proposed. It has been argued [23] that the parasitic capillary waves are a substantial source of vorticity in the crest region, and this vorticity is much larger than the vorticity contributed by the gravity wave itself. Lin an Rockwell [34], in a PIV experiment with a steady breaker produced

by a submerged hydrofoil, stated that the fluid deaccleration around the sharply curved surface of the breaker was the largest source of vorticity. Reference [35] offered further analysis using PIV measurements of a steady breaker produced by flow through a honeycomb. It was asserted that the major source of vorticity is the deacceleration of a thin free-surface fluid layer prior to breaking, and that this vorticity is then injected to the rest of the flow through the action of viscosity.

The initial vorticity produced in the breaking region grows rapidly and large coherent vortical structures begin to emerge in the sub-surface flow as breaking develops. In a field of waves, such as wind-waves on the ocean surface, this can lead to fully developed turbulence in the sub-surface motions. The turbulence statistics of such flows has been studied in the field ([72], [73], [74]) and in experiments ([75], [76]). In laboratory measurements, 2D PIV has been one of the most common methods used to visualize vortex structures beneath breakers, and much work has been done in this area, in particular by Siddiqui and colleagues ([77, 43, 78]), as well as [36], [79], [80], and [81]. [82] and [83] investigated the connection between such coherent motions in the unstable shear flow beneath breakers and the streamwise ripples generated on the water surface. In [82], the physics generating the ripples in the wake of a submerged hydrofoil were explored using a linear stability analysis of the shear flow in the breaking region. Measurements of the frequencies of the ripples in the wake and the wavelengths of the ripples at the breaker were captured well with this linear stability analysis. [83] employed a 2-D, two-fluid Navier-Stokes solver with a level-set technique to study the near surface flow and surface fluctuations produced by a submerged hydrofoil. This work captured the effect of surface tension under

weaker breaking conditions. Spectra of the free surface fluctuations were found to be in good agreement with the experiments of [82]. The presence of an intense shear flow at the toe, which gives rise to coherent vortex-structures near the breaker crest, was also reported.

Coherent structures and ripples that occur in streamwise planes (i.e. with vorticity oriented in the cross-stream direction) are ostensibly the dominant features in breakers, as the largest fluid velocities and highest surface curvatures are in the streamwise direction. However one of the hallmarks of turbulence is the rapid reorientation of vorticity and in many canonical turbulent flows, streamwise oriented structures are dynamically significant (e.g. the "braid" vortices in free-shear layers and "low-speed streaks" in boundary layer turbulence). It is no surprise therefore that the sub-surface flow and surface ripples produced by breakers are 3D in nature, and a few groups have looked into various aspects of this problem. [45] used wave height gauges to measure the cross-stream ("lateral") and streamwise ("longitudinal") coherence levels of surface fluctuations at several locations along a steady breaker produced by a submerged hydrofoil. Lateral coherence levels were found to decrease very rapidly within less than 50 mm separation between probes, while longitudinal coherence remained significant over almost half the wavelength. This led to the description of breaking zones as comprised of "laterally compact, incoherent sources, which radiate longitudinal oscillations". [84] reported measurements of the cross-stream profiles of waves, also generated by a submerged hydrofoil. They found that no clear cross-stream wavelength emerged and that the flow essentially remained 2D, although the amplitude of the cross-stream oscillations did increase

with Froude number. [85] used PIV to measure the streamwise oriented vorticity in a wind-wave field to understand the development of surface streaks (Langmuir circulations). The measurements showed very clearly the development of streamwise vortex structures, although these structures took many wave periods to develop, and were not necessarily the result of individual breaking events. [86] used the results of a 3D LES computation to develop a model for the structure of vorticity in plunging and spilling breakers with no surface tension (i.e. a jet is formed at the crest). It was found that streamwise oriented "scars" formed on the jet, and the location of these scars corresponded to voids in streamwise oriented "rib" vortices. [87] also developed a hybrid stereo-PIV system to look at the 3D flow structure under shallow water plunging breakers, showing the existence of braid-like vortices over the top of larger roller vortices created by the jet impact. An interesting set of results was published by [88] who developed a 3D Navier-Stokes solver that handled the non-linear boundary conditions at the free surface without approximation through the use of a coordinate transformation. Because the boundary conditions are satisfied exactly, [88] showed the applicability of their numerical scheme to wind driven gravity-capillary waves by means of an applied pressure forcing similar to that of [58]. The results show a clear cross-stream structure near the crest of steep gravity waves with parasitic capillaries on the forward face. [88] also identify cross-stream "streaks" in the crest region that are aligned in the flow direction with average intervals of roughly 0.6 cm, which is close to the earlier experimental observations made by [55] for waves in a wind-wave flume. The location of these streaks appears to correspond with the location of cross-stream surface undulations.

Part of the problem with understanding the formation of cross-stream surface structures is that it is still not quite known exactly how the sub-surface turbulence interacts with a real free surface (i.e. with waves and surface tension present), particularly in a transient event like breaking where the turbulence is not fully developed, highly anisotropic and located very close to the free surface. A comprehensive review of this problem, along with a categorization of different surface flows based on turbulent length and velocity scales, is given in [89]. Much of our knowledge about turbulence near a free surface comes from studying canonical flows such as vortex rings, axisymmetric jets or homogenous turbulence. [90] provides an extensive review of early work in this area, including details of different mechanisms of vortex reconnection at a free surface and the various treatments of free-surface boundary conditions. Since this review, additional experiments on vortex rings interacting with a clean and contaminated free surface were presented by [91], and [92]. [93] further studied the problem of an obliquely rising vortex ring with a numerical calculation of the Navier-Stokes equation with a viscous free surface. It was found that while surface depressions did form near the center of the surface connected vortices, in general the surface elevation did not correlate well with the vertical component of vorticity, ω_z, in particular when the vorticity distribution was not vertically axisymmetric. In experiments on a vertically oriented free-shear layer interacting with a free surface, [94] and [95] used simultaneous PIV and surface gradient measurements to correlate the component of normal vorticity to the surface elevation. The raw results showed low correlation levels, ~ 0.2, seemingly in agreement with [93]. However [95] showed that conditionally correlating the vertical vorticity and surface

height, to take into account the appropriate sign of each, revealed much higher correlation levels, ~ 0.8, leading to the conclusion that the ripples on the surface are the result of surface-connected vortices. In contrast [96], in numerical simulations of open channel turbulence, showed that free surface "splats" (turbulent upwelling) and "antisplats" (turbulent downwelling) were created by streamwise oriented, counter-rotating vortex pairs ejected off the bottom boundary, and that surface connected vortices had little do with the existence of these surface features. In recent works by Savelsberg & Van de Water ([97], [98]), the correlation between the surface fluctuations and sub-surface flow was studied experimentally. A scanning laser technique was used to measure the gradient of the surface fluctuations while 2D PIV was used to measure the flow near ($\approx$ 1mm below) the free surface. It was found that the convective acceleration field $\xi = -(u \cdot \nabla)u/g$ and the surface gradient field correlated fairly well for the irregular flow behind a submerged cylinder, but poorly for homogenous grid generated turbulence. [98] broke the convective acceleration field into strain and rotational components to determine the effect of each type of motion on the surface fluctuations. For the irregular flow behind a cylinder, both strain and rotation type motions contributed equally, while rotation type motions were slightly stronger in homogenous turbulence. The authors used this result to conclude that the model of surface dimples above vertically oriented turbulent eddies may be too simple in homogenous turbulence.

The prevalence of three-dimensional vorticity under breaking waves coupled with the complicated manifestations of vorticity on free surfaces and the effects of surface tension on the dynamics makes the study of cross-stream surface structures

produced by breaking waves a relevant research question. Therefore, in this chapter detailed measurements of cross-stream surface profiles of unsteady spilling breakers are presented.

3.3 Experimental details

3.3.1 Wave generation: isolating the effect of surface tension

The facility used in these experiments is the same as described in Chapter 2. The waves in this study were generated using the dispersive focusing technique similar to that used by previous authors ([68], [1]) and as described also in Chapter 2. Three different average wavepacket frequencies $\bar{f}$, with five different wave-maker amplitudes A were used. Because the small surface ripples generated during breaking are strongly affected by surface tension, we would like to isolate this effect[1]. In order to do this, all of the relevant experimental parameters (such as the water depth, submergence of the wedge wave-maker, the amplitude of the wave-maker motion, etc.) were scaled with the nominal wavelength $\bar{\lambda}$ $(= g/2\pi\bar{f}^2)$. Defining the Froude number as $Fr = U^2/gL$, where U and L are characteristic velocity and length scales, respectively, we note that if $L \propto \bar{\lambda}$, and $U^2 = L^2\bar{f}^2 \propto \bar{\lambda}$, then the Froude number is independent of the wavelength[2] . A constant Fr implies a ratio between inertial and gravitiy effects that is scale independent. That is, in the absence of surface tension,

[1]Viscosity also plays a role in damping the motion of the surface rippples but, for reasons discussed in Chapter 1, we shall ignore such affects here.

[2]Linear deep water gravity waves naturally have constant Froude number that is independent of wavelength. This can be seen, for example, by taking $U^2 = c_p^2 = g\lambda/2\pi$ and $L = \lambda$. Here we are merely pointing out that the experiments have been scaled so that dispersively focused wave-packets generated with different $\bar{f}$ all have the same Froude number.

the resulting non-dimensional wave motions in z/T–t/T coordinates are identical (here z is the wave height and T the wave period). However, in real waves with surface tension, the Weber number $We = \rho U^2 L/\tau$ is not wavelength independent, and the capillary restoring force is stronger for smaller waves than for larger ones. Thus using Froude scaled breakers allows us to investigate the effect of surface tension on the breaking process.

The values of the different parameters used for each case are given in table 3.1. Other details of the experimental parameters are given in the table caption. For each condition, several side-view images (like those in Chapter 2) were also taken to determine the height of the wave at breaking h_b. It should be noted that changing $A/\bar{\lambda}$ does not affect the breaking wave height dramatically (typically only a few percent), but it does affect the visual "strength" of the breaker. With these wave-maker amplitudes, the breakers range from very weak spillers at $\bar{f} = 1.40$ Hz and $A/\bar{\lambda} = 0.0514$, to strong spillers where a jet nearly forms at the wave crest at $\bar{f} = 1.15$ Hz and $A/\bar{\lambda} = 0.0522$. Taking $U^2 = \bar{U}^2 = g\bar{\lambda}/2\pi$ (i.e. the phase speed of the average component of the wave packet), $L = h_b = 0.07\bar{\lambda}$, $\tau = 0.073$ N/m, $\rho = 1000$ kg/m^3, and $\nu = 1 \times 10^{-6}$ m^2/s, the important nondimensional groups are found to be $Fr \approx 2.3$ for all waves, and $We = (1.35, 2, 2.97) \times 10^4$ for $\bar{f} = 1.40, 1.26$ and 1.15 Hz, respectively. It should be noted that the large values of We are a result of using $\bar{U}$ and $\bar{\lambda}$ as the velocity and length scales, although surface tension effects are most important near the wave crest, where there is no definitive velocity or length scale. Perhaps a more revealing nondimensional number to highlight the effect of surface tension is the ratio of the minimum gravity-capillary

$\bar{f}$ (Hz)	$\bar{\lambda}$ (cm)	U_c (cm/s)
1.40	79.58	94.49
1.26	98.24	102.11
1.15	117.94	112.80

Table 3.1: The wave-maker and carriage parameters used for the cross-stream profile experiments. $\bar{f}$ is the average frequency of the wave packet, $\bar{\lambda}$ is the wavelength of the average frequency, and U_c is the final speed of the carriage. For each frequency, five different values of $A/\bar{\lambda}$ (the normalized wave-maker amplitude) were used: 0.0514, 0.0516, 0.0518, 0.0520, 0.0522. For each frequency, the carriage delay time from the start of the wave-maker motion, t_d, was 12.22, 12.47 and 13.23 seconds for $\bar{f} = 1.40, 1.26, 1.15$ Hz, respectively. Other motion parameters include: the normalized submergence of the wedge $h_s/\bar{\lambda} = 0.358$, normalized water depth $H/\bar{\lambda} = 0.9308$, the normalized breaker distance $x_b/\bar{\lambda} = 6.2$, the phase of the wave-maker motion $\phi = -90°$, and the acceleration of the carriage $\ddot{U} = 50.0$ in$/s^2$. Note that the depth of submergence of the wedge was controlled by changing the offset of the wedge position sensor so that the tip of the wedge was the appropriate distance below the mean water level when the position sensor read zero.

wavelength $\lambda_{min} = 2\pi(\tau/g\rho)^{1/2}$ to the gravity wavelength $\bar{\lambda}$. Such a ratio yields $0.022, 0.018, 0.015$ for $\bar{f} = 1.40, 1.26$ and 1.15 Hz, respectively. Regardless of the form, it is clear that the smaller wavelengths (higher frequencies) are more affected by the fluid surface tension.

3.3.2 Wave profile measurement

As in the experiments of Chapter 2, the profiles of the breaking waves were measured photographically with a Laser-Induced-Fluorescence (LIF) method that employs a high-speed digital movie camera. However, in this set of experiments, the carriage optics spread the laser beam into a sheet oriented *across* the width of the

tank. This sheet spans the width of the tank and is 1 mm thick in the streamwise direction at the mean water level. Another difference is that the high-speed camera (Phantom v9, Vision Research) is now mounted to the instrument carriage on the inside of the tank, see figure 3.1. The camera is located downstream of the light sheet, and looks upstream at the intersection of the light sheet and water surface from above. Both the camera and light sheet are mounted to the carriage which is set to move with the approximate speed of the breaking wave crest. The carriage parameters are adjusted so that the light sheet is located at the wave crest when breaking begins, see below.

One experimental difficulty that must be overcome with this setup is finding a location and look-down angle for the camera that provides a trade off between an unobstructed view of the light sheet and vertical resolution of the image. As the wave breaks, large turbulent ripples generated in front of the laser sheet (that is, between the laser sheet and camera) can cause the line of sight to the crest profile to become blocked and lead to errors in the profile measurements. This was observed in the measurements of unsteady spillers reported by [99]. In order to obtain high-quality images the camera must be high enough to see into any ripple troughs, which requires a large lookdown angle. Because of the large look down angles, when the wave height changes during breaking the distance from the crest to the camera lens changes, which can cause profiles to be out of focus. This problem is mitigated by the use of a tilt-shift lens which is used in all of the experiments. Large viewing angles, however, reduce the vertical resolution of the images so small amplitude ripples may not be resolved. Finally, the camera has to be positioned a

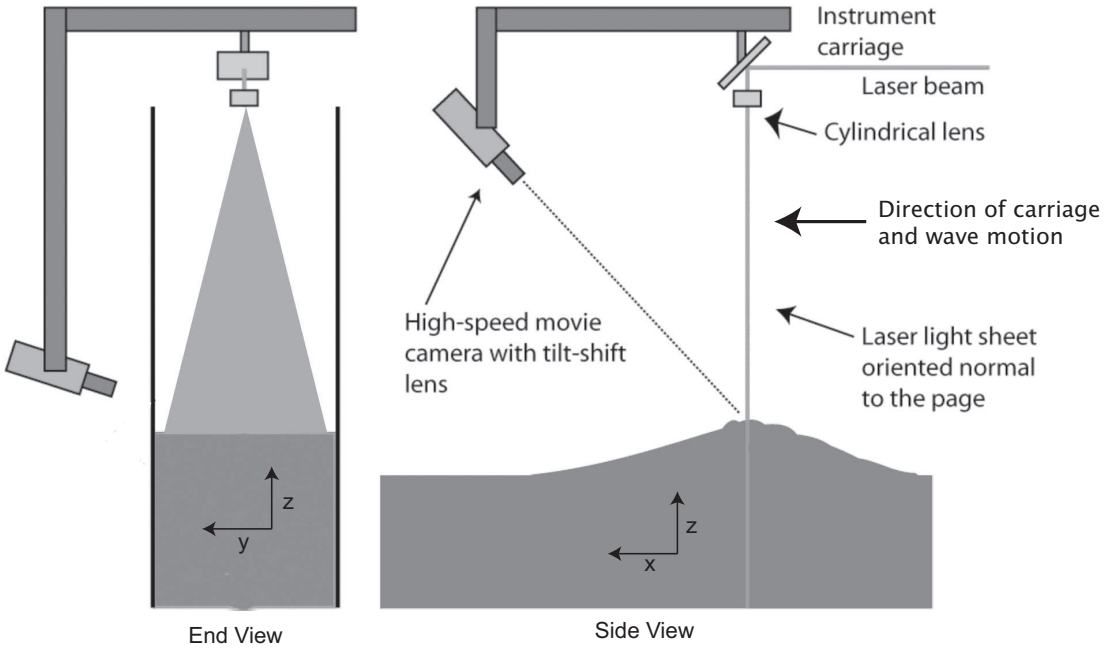

Figure 3.1: Schematic of the setup for measuring the cross-stream profiles. The laser light sheet is oriented across the tank, and a high-speed camera images the intersection of the laser sheet and water surface from the front (downstream) side of the breaker. Both the camera and light sheet optics are mounted to the carriage and move with the speed of the breaking wave crest. The camera has a tilt-shift lens mounted on it to handle the large look down angle. A second camera, also attached to the carriage but positioned outside the tank, images the position of the laser sheet relative to the wave crest from the side.

safe distance above the mean water level to prevent water droplets or spray from collecting on the camera body and lens. Unfortunately, as with the viewing angle dilemma, mounting the camera too high again reduces vertical resolution; for a given viewing angle θ, and height h, the distance from the camera sensor to the light sheet is given by $L = h/sin(\theta)$.

The interplay between all of these factors was dealt with by trial and error. The camera was mounted at a fixed horizontal distance from the light sheet, and was initially positioned at a "safe" distance above the mean water level (roughly three times the typical wave amplitude used in the experiments $\sim$ 20 cm). The camera was

then angled downwards until the mean water level was in the center of the image. A patterned checkerboard was placed underneath the laser sheet and the tilt-shift lens and camera focus were adjusted until both the top and bottom of the checkerboard image were sharp. A breaking wave was then generated and recorded and the movie was investigated for any visual signs of blockage, which appear as dark patches or out of focus edges in the profile. If the movie was unsatisfactory, the camera would be raised, the viewing angle increased, the tilt-shift lens and focus would be adjusted, and another movie would be taken. This process was continued until the recorded movies appeared to be free of blockage. For these experiments, the camera was placed a horizontal distance of 1 m from the light sheet, and anywhere from 76–89 cm above the mean water level, with the tilt-shift lens set in the range of 40–45 degrees tilt; the precise height and angle depended on the frequency and amplitude of the wave being investigated. With this configuration, one camera pixel corresponded to roughly 0.2 mm in the physical plane. Profile measurements are extracted from the camera images using the processing and edge-detection techniques described in Chapter 2.

Because the laser sheet and high-speed camera measure the cross-stream profile at a single streamwise location, it is important to ensure that the light sheet is located at or near the crest of the wave of interest when breaking begins. Therefore, in addition to the profile camera located inside the tank, a second camera (Phantom v4, Vision Research) is mounted to the carriage on the outside of the tank; see figure 3.1 (end view). This camera, which is synchronized with the profile camera, is used to locate the approximate position of the light sheet relative to the wave crest as

the wave breaks. The second camera views the light sheet from the side and is back lit with white light so that the location of the wave crest is clearly visible. Using this side-view camera the carriage speed can be chosen emprically to match the approximate speed of the wave crest as it breaks. Here we say the "approximate" speed because the wave crest is rather flat and its shape changes as it approaches breaking, so precisely defining what point on the wave is "the crest" can be a bit ambiguous. Furthermore, the crest speed does change slightly in the approach to breaking and although the carriage motion could be made more complex to perhaps mimic these changes, for simplicity the carriage is run at constant speed. However, it is possible to repeatedly and accurately position the light sheet very near the (apparent) crest at the moment breaking begins. This is accomplished by varying the delay time between the carriage motion and the wave-maker motion, t_d, and the various delay times used are reported in the caption to table 3.1. While this carriage motion is highly repeatable, there is a natural variation in the streamwise location of the breaking event, which can be as high as 2 cm, see [1]. The result is that if the laser sheet is too close to, or perhaps slightly ahead of, the wave crest, it is possible for the wave to begin breaking *behind* the light sheet. As the toe and ripples advance down the front face they "pierce" the light sheet, causing a sudden jump in the surface height that is not processible. In order to avoid this problem, the start delay of the carriage relative to the wave-maker was adjusted so that the light-sheet was located just behind, but not quite at, the wave crest when breaking began, so the leading edge of the breaking zone is located in front of (downstream) of the light sheet. Using the images from the side-view camera, and considering the

natural variation of the breaker, we estimate the light sheet to typically be located in the range 1–3 cm behind the wave crest when breaking begins, a range of about 0.03 wavelengths for the smallest breakers investigated.

3.4 Results and discussion

3.4.1 Frequency dependence: the effect of Weber number

Figure 3.2 shows a sample of images recorded by the cross-stream profile camera for $\bar{f} = 1.26$ Hz and $A/\bar{\lambda} = 0.0522$. The width of each image in the physical plane is 22 cm (a little less than a quarter of a wavelength). Each image corresponds to a different time after the wave begins to break (defined as when the toe begins to move down the front face). In these images, the horizontal is the cross-stream (y) direction, while the vertical is the z direction, see the axes in figure 3.1. Herein the term "cross-stream ripples" refers to the variation of the wave profile in the cross-stream (y) direction, while the term "streamwise ripples" refers to variation in the streamwise (x) direction. The images in figure 3.2 clearly show the development of cross-stream ripples as the breaking progresses. Images such as these were processed to obtain a 2D cross-stream profile at each moment in time. Quantities such as the horizontally averaged mean water level, the ripple amplitude, and the ripple wavelength were obtained from these profiles.

Figure 3.3 (upper curves) shows the cross-stream averaged wave height $\bar{z}$ as function of time t for three different runs with $\bar{f} = 1.26$ Hz and $A/\bar{\lambda} = 0.0522$. In this plot, $\bar{z}$ is scaled by $\bar{\lambda}$ and t is scaled by the wave period T. Because $\bar{z}$ is averaged

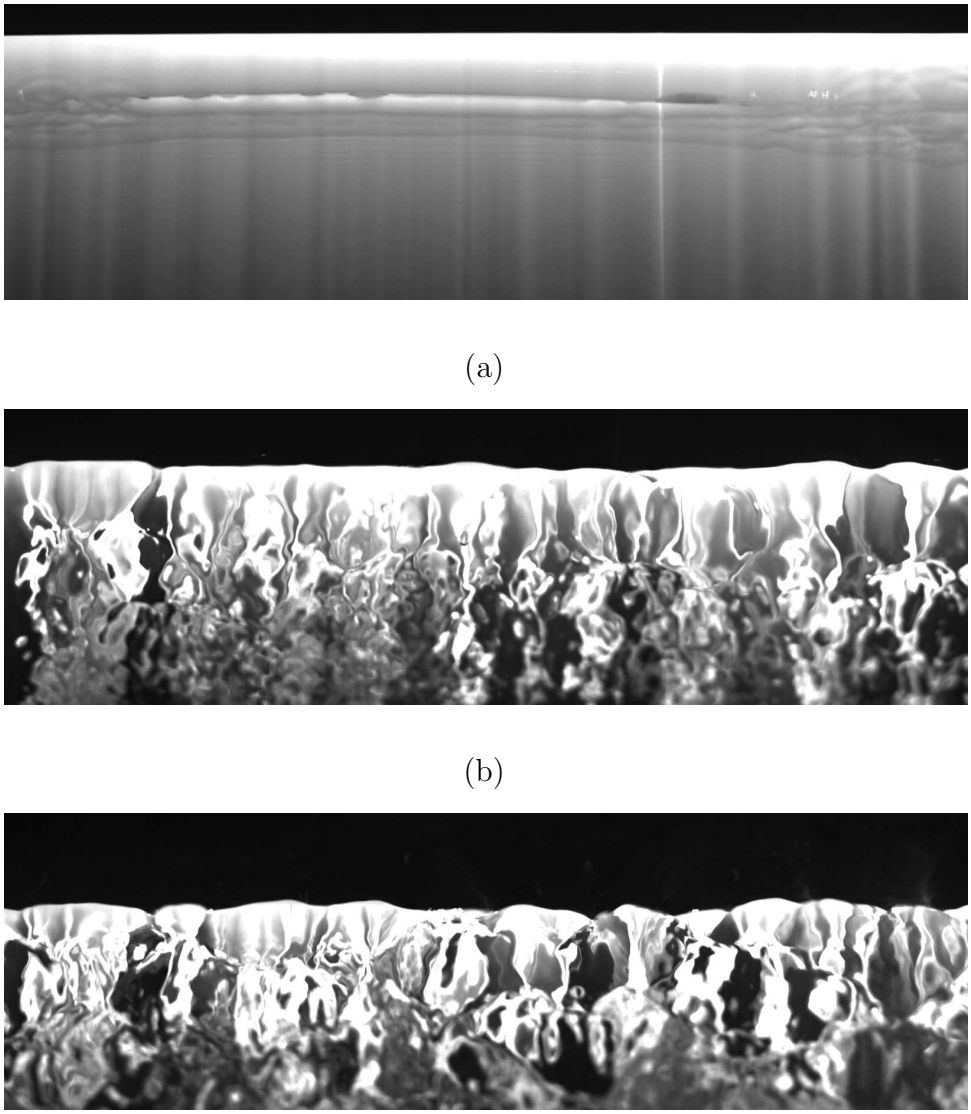

(a)

(b)

(c)

Figure 3.2: Images taken by the cross-stream camera during a typical breaking event. The camera looks at the wave from the front and moves with the speed of the crest. For these three images, $\bar{f} = 1.26$ Hz and $A/\bar{\lambda} = 0.0522$. The intersection of the main dark and light regions near the top of the image is the cross-stream wave profile at the intersection of the laser sheet and water surface. The bright and dark spots in the lower part of the images are due to two refraction effects. First, the laser light enters the water and is refracted by the rippled surface. Next, this refracted light is being viewed by the camera looking through the rippled surface that is between the light sheet and camera. Each image corresponds to a different time after the toe begins to move: (a) 0.1 wave periods. The toe is spilling down the front face. (b) 0.3 wave periods. The turbulent region has advanced farther and the profile begins to show cross-stream undulations. (c) 0.5 wave periods. The cross-stream ripples are more numerous and larger in amplitude.

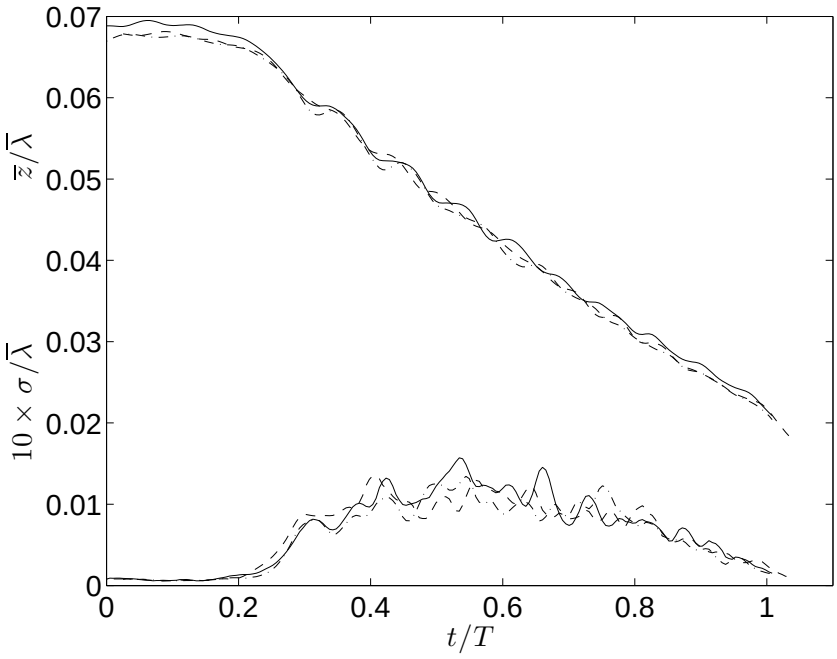

Figure 3.3: Plots of the nondimensional horizontally averaged wave height $\bar{z}/\bar{\lambda}$ (upper curves) and nondimensional standard deviation of the cross-stream wave profile $\sigma/\bar{\lambda}$ (lower curves) versus nondimensional time t/T. Data are presented from three separate runs with $\bar{f} = 1.26$ Hz and $A/\bar{\lambda} = 0.0522$. Note that σ is scaled by a factor of 10.

horizontally, variations in $\bar{z}$ are the result of 2D streamwise ripples. Also plotted on the same set of axes is a measure of the typical amplitude of the cross-stream ripples σ (lower curves). An obvious choice for σ would be the standard deviation of the cross-stream profile, as this would remove the effect of changes in $\bar{z}$ and capture only the cross-stream fluctuations. However, it was found that for most of the waves the breaking process does not begin uniformly across the tank, with some parts of the wave crest breaking before others. That is, the waves have a slight three-dimensional shape to them at breaking, something that is commonly observed even in wave tanks. This slight asymmetry causes one side of the profile to be higher or lower than the other side during the early stages of breaking, creating large standard

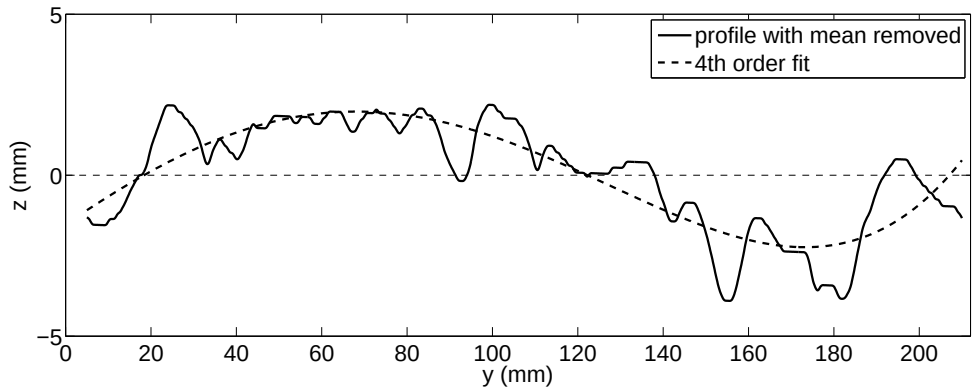

Figure 3.4: Figure showing how large cross-stream asymmetries in the breaker profiles can affect the measurement of the smaller ripples. The solid curve is a cross-stream wave profile with the mean removed. Notice the average value on the left is higher than on the right so that if the rms is taken about zero an unphysically large value of rms is recorded. The dashed line is a 4^{th}-order polynomial fit to the profile that captures the long-wavelength undulation. Taking the rms about this fit yields a more physically reasonable rms.

deviations even when no cross-stream ripples were visibly present, see figure 3.4. In order to remove this effect, after subtracting the value of $\bar{z}$, the resulting profile was fitted with a 4^{th}-order polynomial. The goal of this polynomial fit was to capture the long-wavelength undulations of the profile created by the asymmetric breaking. The value of σ was then computed as the rms of the difference of the actual profile (with $\bar{z}$ removed) from this fitted profile. This technique of using a higher order polynomial is essentially a high-pass filter, reducing the amplitude contributions of the longest wavelength waves and the spurious peaks in the value of σ. The order of the polynomial was chosen by repeatedly increasing the leading order until the difference between successive fits was small and the peaks of σ remained unchanged. For this data, the rms of the difference between using a 4^{th} and 5^{th}-order fit was typically only a few percent of the maximxum value of σ, and the heights and

locations of the peaks were nearly identical. As a final check, we also compared the temporal location of the peaks of σ with the corresponding images from the high-speed camera for several cases. The surface indeed showed more ripples at these times and we are confident that using a 4^{th}-order fit retains the high frequency cross-stream structure while reducing the large scale three-dimensional breaking effects. The effectiveness of this method at reducing contributions from longer wavelengths while not degrading those from shorter wavelengths implies a certain separation of length scales in the cross-stream direction. A similar technique was employed for computing the cross-stream wave spectra (see below).

The curves of $\bar{z}$ in figure 3.3 show the repeatability of the wave motion from run-to-run. The curves are remarkably similar, in particular in the early and later stages of breaking ($t/T < 0.4$ and $t/T > 0.8$). In between these limits, the mean water level undergoes a series of oscillations. For a given wave these oscillations are fairly regular, but the profiles show some variation from run-to-run. These oscillations in $\bar{z}$ are due to "quasi-2D" streamwise ripples, or "rollers", that are generated at the leading edge of the breaking region and are oriented parallel to the wave crest. Because of their slower phase speed relative to the wave crest, these ripples are swept back over the crest and measured in the plane of the light sheet as it passes by. To help explain this, figure 3.5 shows *streamwise* profile measurements made by [1] (their figure 14). The profiles are from a wave with $\bar{f} = 1.42$ Hz and $A/\bar{\lambda} = 0.0487$, conditions which were not studied in the present work. The profiles are taken in a frame of reference moving with the wave crest and each successive profile is plotted 1 mm above the previous profile for clarity (i.e. moving upward in the

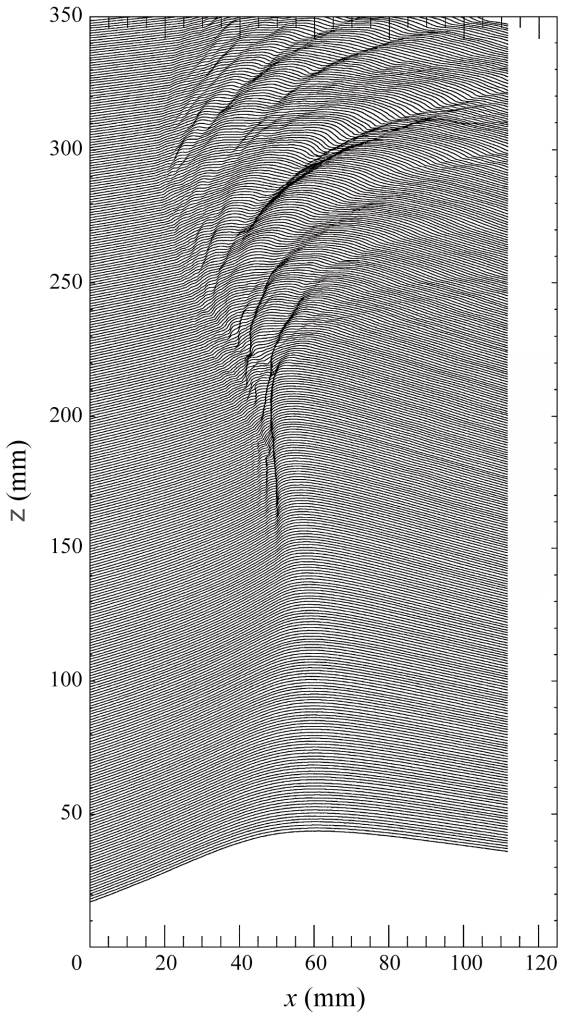

Figure 3.5: Figure 14 from [1] showing the streamwise profile history for a spilling breaker generated by the dispersive focusing technique. In their experiment, $\bar{f} = 1.42$ Hz and $A/\bar{\lambda} = 0.0487$. Each profile has been offset 1 mm from the previous profile for clarity. Note the periodic generation of streamwise ripples in the breaking zone.

plot is moving forward in time). The profile history clearly shows the development of periodic streamwise ripples that move slower than the wave crest. The location of these streamwise ripples in the current experiments is also visually supported by the second high-speed camera which images the breaking process from the side. At times when $\bar{z}$ is at a local minimum, the laser sheet is observed to be in the

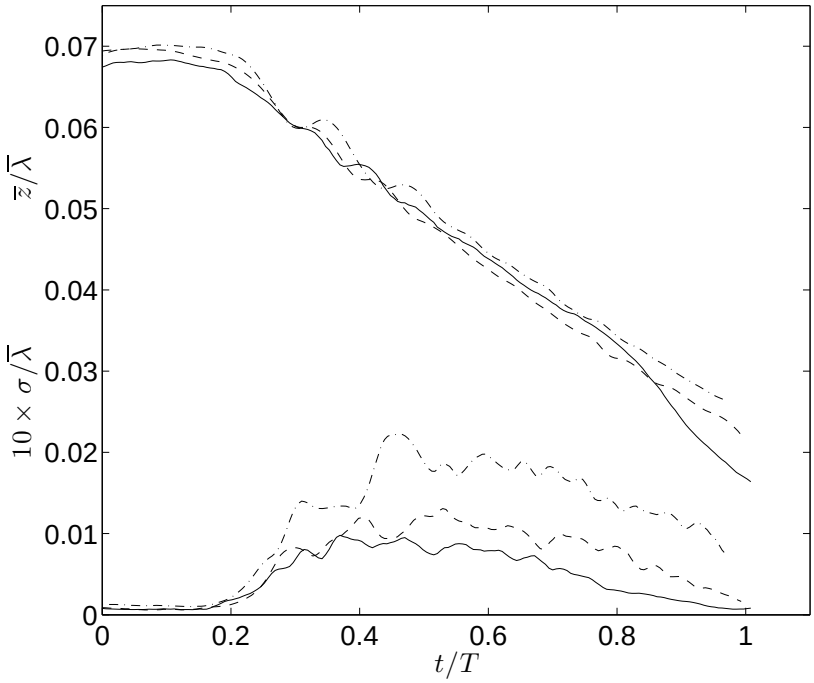

Figure 3.6: Plots of $\bar{z}/\bar{\lambda}$ and $\sigma/\bar{\lambda}$ versus nondimensional time t/T for three different values of $\bar{f}$. Data are from runs with $A/\bar{\lambda} = 0.0522$ and $\bar{f} = 1.40$ Hz (solid curve), 1.26 Hz (dashed curve) and 1.15 Hz (dashed-dotted curve). Each curve is the average of three runs. Note that σ is scaled by a factor of 10.

"troughs" of these rollers. We term these streamwise ripples "quasi-2D" because while on average they extend across the measurement area, they are not uniform in the cross-stream, but instead are rippled as evidenced by the non-zero values of $\sigma/\bar{\lambda}$ in figure 3.3. Like the curves for $\bar{z}$, the general shape of the curves for σ are reproducible, but the details vary from run-to-run in the middle of the breaking process (say $0.4 < t/T < 0.8$). The value of σ shows peaks as well, and these peaks are nearly coincident with the location of the local minima of $\bar{z}$ indicating that the strongest cross-stream fluctuations are at the troughs of the larger streamwise ripples. This will be discussed in more detail in section 3.4.3.

Figure 3.6 shows $\bar{z}/\bar{\lambda}$ and $\sigma/\bar{\lambda}$ versus t/T for three different frequencies all with

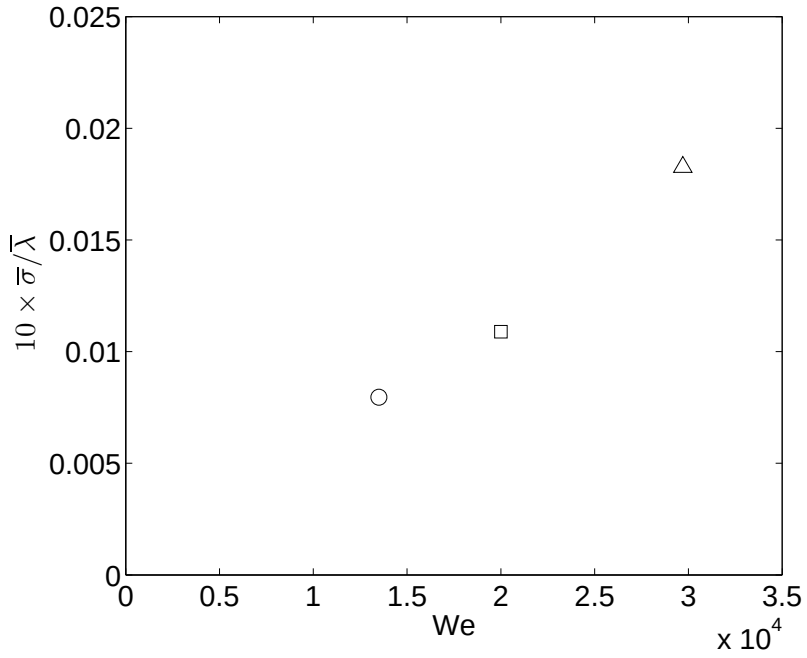

Figure 3.7: Plot of $\bar{\sigma}/\bar{\lambda}$ versus We, where $\bar{\sigma}$ is the value of σ from figure 3.6 averaged over the range $0.4 < t/T < 0.7$. Note that $\bar{\sigma}$ is scaled by a factor of 10. A linear relation between $\bar{\sigma}/\bar{\lambda}$ and We implies $\bar{\sigma} \propto \bar{\lambda}^3$.

$A/\bar{\lambda} = 0.0522$. Each of the curves in figure 3.6 is obtained from the average of 3 runs at each condition. The curves of $\bar{z}/\bar{\lambda}$ have been adjusted slightly so as to coincide at a common feature, in this case the beginning of the streamwise oscillations (at $t/T \approx 0.3$). This helps to make the effect of the Froude scaling more apparent. As was mentioned in section 3.3.1, without surface tension or visocity (or breaking), the wave profiles should collapse in $z/\bar{\lambda} - t/T$ coordinates. We see that this is mostly true for these waves, as the general shape of the curves are quite similar. The occurence of the quasi-2D ripples, however, do not appear to Froude scale, as both the amplitude and period of the ripple oscaillations increase. For example, for $\bar{f} = 1.40$ Hz, the spacing between the fist two minima of $\bar{z}$ is $\Delta t = 0.075T$, whereas for $\bar{f} = 1.15$ Hz, $\Delta t = 0.13T$, an increase of more than 70%. This lack

of scaling matches intuition as the ripples are not simply governed by gravity and inertia alone, but instead are generated by the shear layer at the leading edge of the breaker and are influenced by surface tension and viscosity, which have a stronger effect at smaller wavelengths. For a clearer picture of this shear layer see the PIV measurements of [34] and [36]. In addition to the growth of the streamwise ripples with $\bar{\lambda}$, the typical amplitude of the cross-stream ripples also increases with $\bar{\lambda}$, as is shown by the plots of $\sigma/\bar{\lambda}$ in figure 3.6. The shape of the curves of σ show general similarity, with growth in the cross-stream ripple ampltiude occuring at around 0.2 wave periods after breaking, peaking near 0.5 wave periods and then a slow decline. For $\bar{f} = 1.15$ Hz, the cross stream ripples still have significant amplitude even up to one full wave period after breaking begins[3]. Again it is found that the location of the peaks in the values of σ coincide with the local minima of $\bar{z}$ for each condition. This is more clear in figure 3.6 where each curve is the average of several runs, so some of the variation from run-to-run has been smoothed out. Furthermore, the cross-stream ripples appear to have a large jump in amplitude between $\bar{f} = 1.26$ and 1.15 Hz, indicating a non-linear relationship between the gravity wavelength $\bar{\lambda}$ and the size of the cross-stream surface fluctuations. To illustrate this, the values of σ were averaged over the range $0.4 < t/T < 0.7$, the approximate range over which the maximum of σ occurs. The result $(\bar{\sigma}/\bar{\lambda})$ is plotted versus the Weber number in figure 3.7. While only three points are available, the data appear fairly linear. It is worth noting that with the definition of We given in section 3.3.1,

[3]We remind the reader that this data is taken in a frame of reference moving with the wave crest. When the crest stops breaking there is a decrease in the surface ripples. There may, however, still be turbulence and ripples left behind the wave crest at a stationary location.

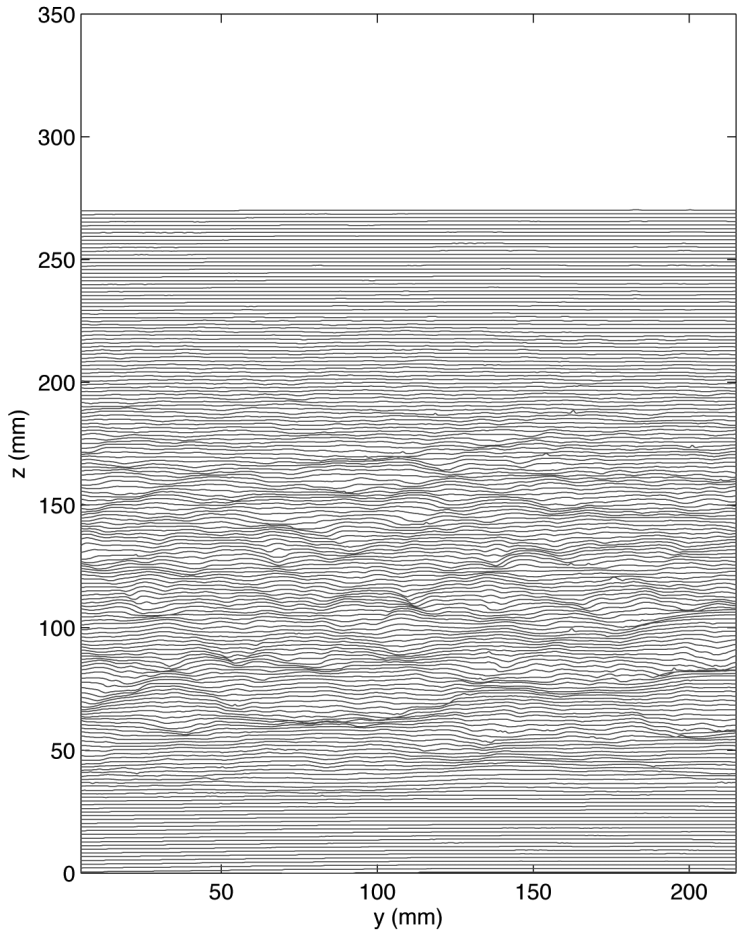

(a) For caption see page 65

Figure 3.8

$We \propto \bar{\lambda}^2$ (because $U^2, L \propto \bar{\lambda}$). Therefore, a linear relation between $\bar{\sigma}/\bar{\lambda}$ and We implies that $\bar{\sigma} \propto \bar{\lambda}^3$. This result is somewhat significant when we consider that the amplitude of the gravity wave scales directly with the wavelength, but the scale of the three-dimensional deformations shows a more sensitive dependence.

Figure 3.8 shows profile histories for the three different wave frequencies all with $A/\bar{\lambda} = 0.0522$. In these plots, the mean of each profile has been removed, and each profile has been plotted 1.5 mm above the previous profile for clarity (that

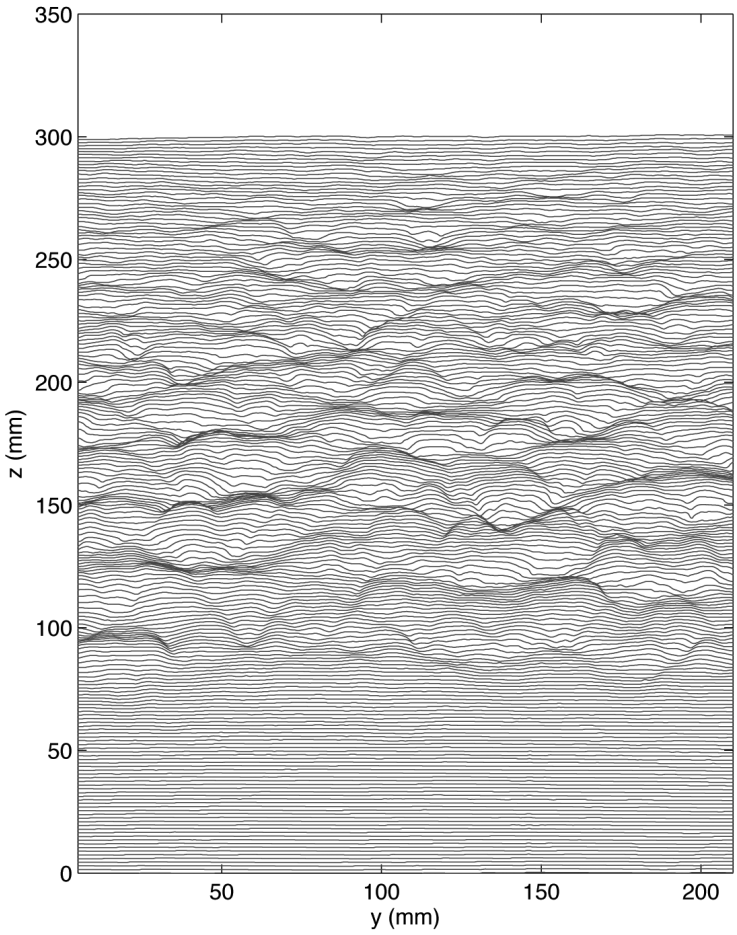

(b) For caption see page 65

Figure 3.8

is, moving upward in these plots is moving forward in time). Each profile history extends from the frame where breaking begins to one wave period post-breaking. Each figure has the same size and range so comparison between various features can be made directly. In these histories, the slope of a line connecting a feature from profile-to-profile indicates its speed relative to the camera. For example, the streamwise profile histories presented in [1] and reproduced here in figure 3.5 clearly show some streamwise ripples that are moving slower than the wave crest. In the

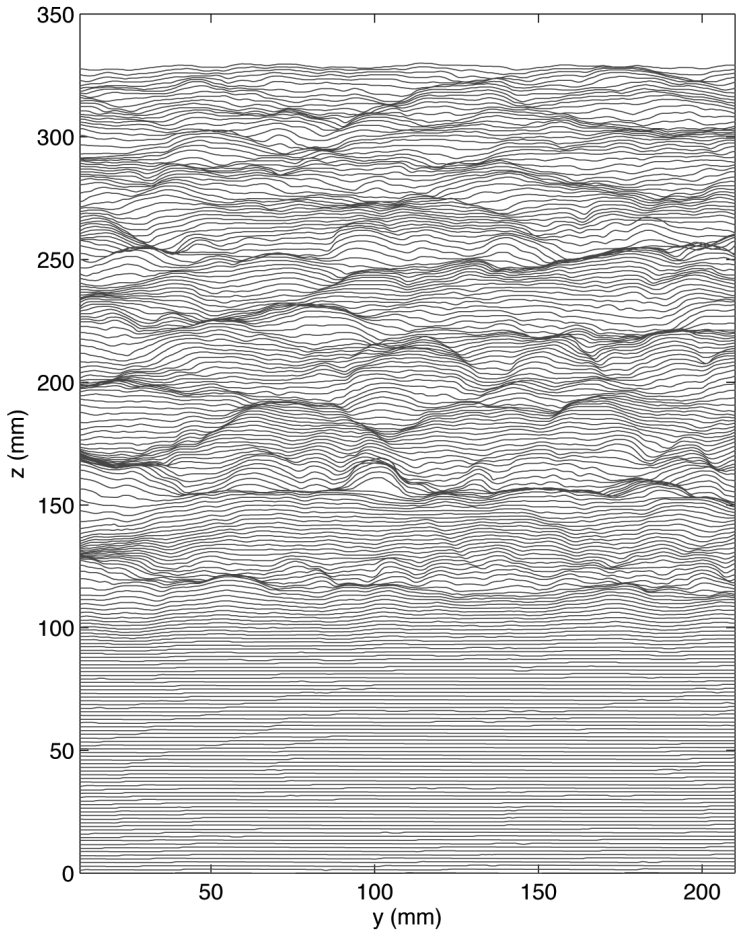

(c)

Figure 3.8: Cross-stream profile histories for three different frequencies with a normalized wave-maker amplitude $A/\bar{\lambda} = 0.0522$. (a) $\bar{f}$ = (a) 1.40 Hz, (b) 1.26 Hz, (c) 1.15 Hz. The horizontally averaged mean has been removed and each profile has been offset from the previous one by 1.5 mm in the vertical. Each figure shows profiles for one wave period post-breaking.

cross-stream profile histories of figure 3.8 the largest energy (amplitude) features appear more as standing waves, as evidenced by the lack of any clearly sloped ridges. Taking a closer look we see there do appear to be some small scale features that move laterally across the field of view; for example, see figure 3.8(b) from about 100 to 150 mm on the vertical axis where light "V" shaped ridge lines appear. The

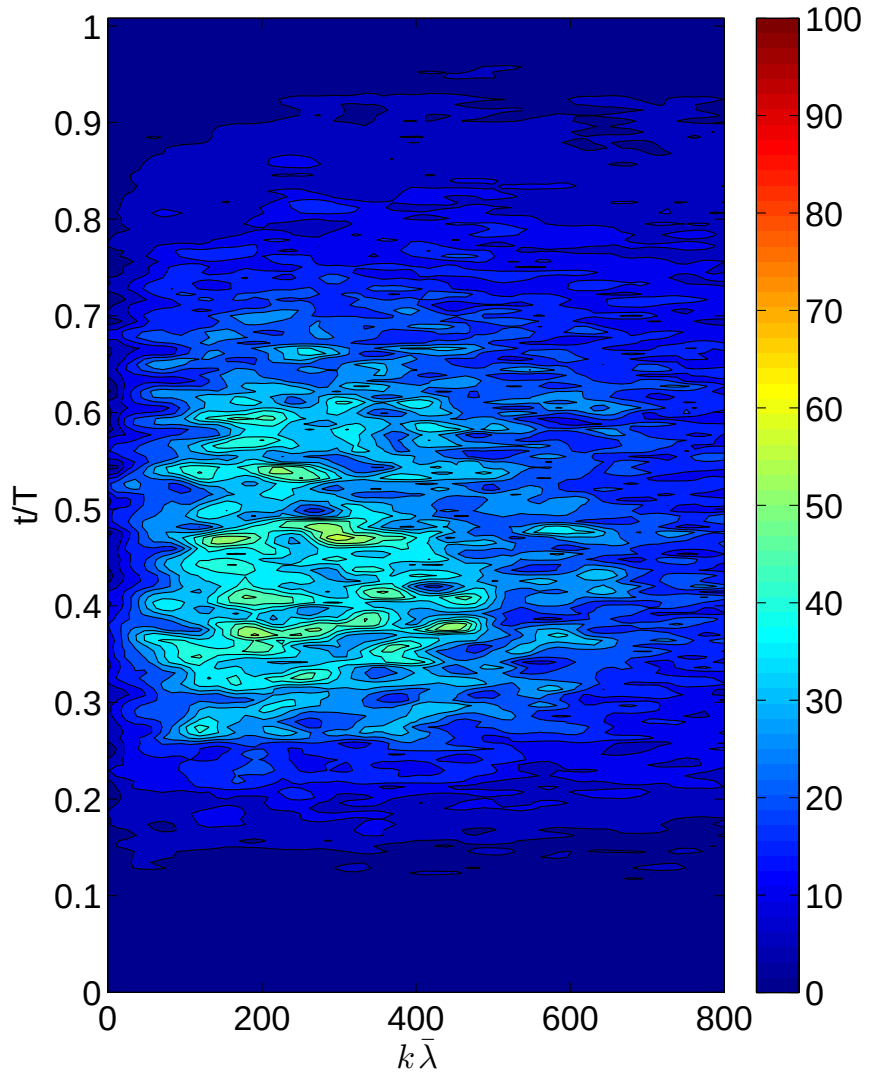

(a) For caption see page 68

Figure 3.9

shape of these features will be discussed more in section 3.4.3. Looking at the profile histories in figure 3.8, the wavelength of the cross-stream ripples appears to increase with wavelength. To quantify this, we can compute the slope spectrum of each profile to get a measure of the dominant wavelengths present. As was mentioned above, cross-stream non-uniformity in the early stages of breaking causes long-wave

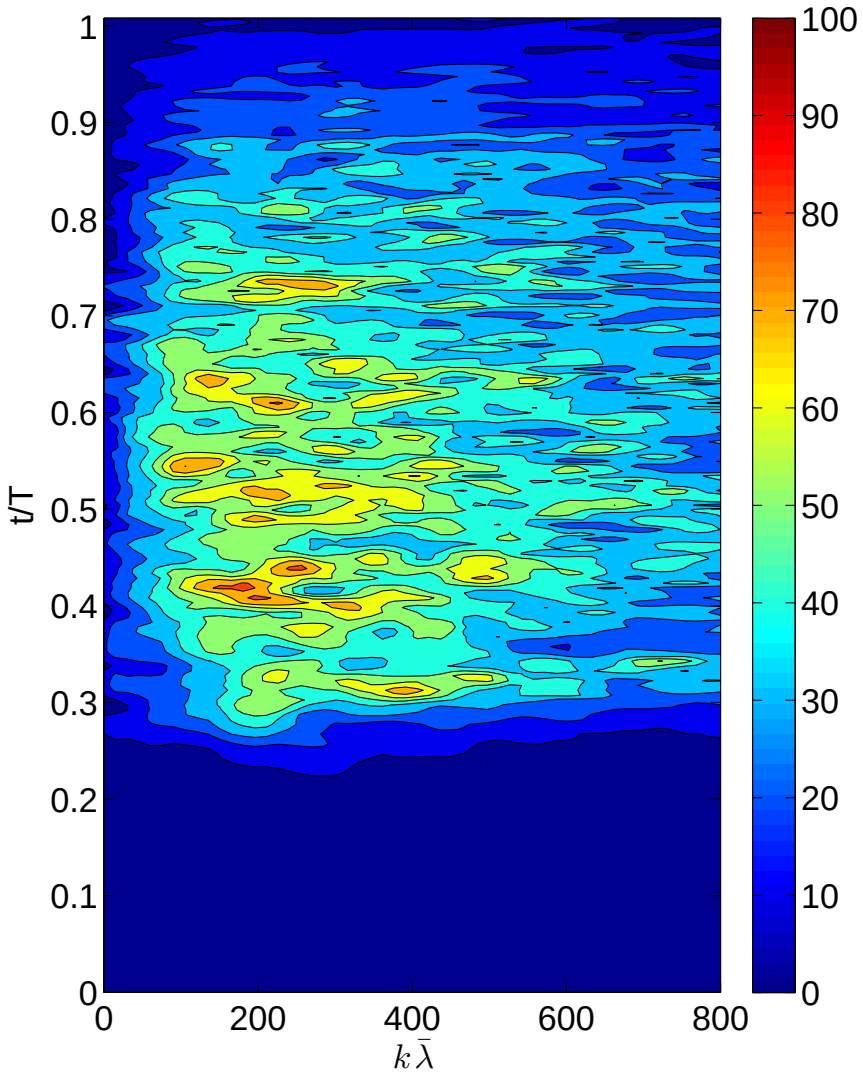

(b) For caption see page 68

Figure 3.9

contributions to the spectra. To lessen this effect, the mean of the profile was removed, and a straight line was fit to the result. This fit was then subtracted out of the profile, and the result from that was used in computing the slope spectrum. The 1D spectra were computed as $|\Omega(k)| = |DFT(z')|$ where z' is the derivative in the cross-stream direction and DFT is the discrete Fourier transform. This technique of

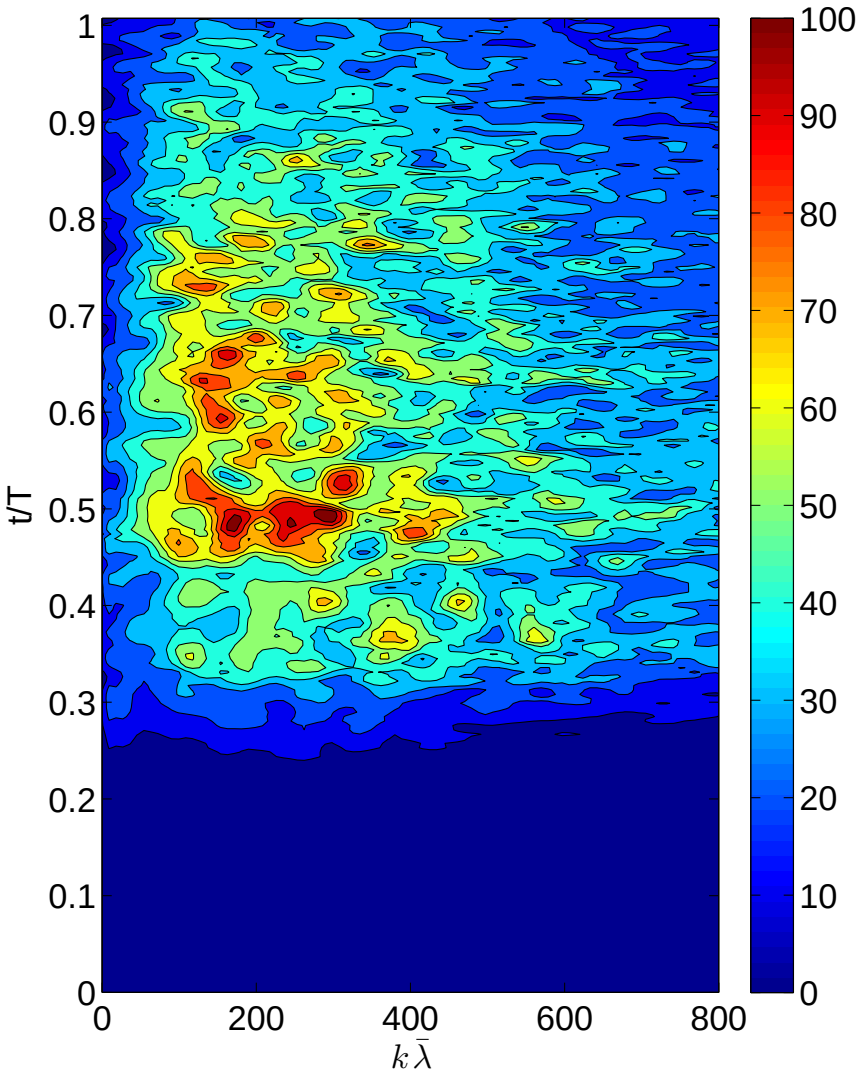

(c)

Figure 3.9: Cross-stream spectra history for three different frequencies with a normalized wave-maker amplitude $A/\bar{\lambda} = 0.0522$. Data are plotted as contour plots where red indicates large values and blue indicate lower values (note the scale color scale is the same in the three plots). Data are for $\bar{f}$ = (a) 1.40 Hz, (b) 1.26 Hz, (c) 1.15 Hz. Each plot is the average of 3 runs at the same condition and shows spectra for one wave period post-breaking.

subtracting out a linear fit and taking the transform of the slope weights the higher wavenumber contributions more heavily, and essentially removes the contributions of longer wavelengths (lower wavenumber). Performing these operations on each

profile, we can create a "spectra history", which shows the behavior of the cross-stream wave spectrum as a function of time after breaking. Results showing the nondimensional spectra $k\bar{\lambda}$ versus nondimensional time after breaking t/T for three different frequencies with $A/\bar{\lambda} = 0.0522$ are shown in figure 3.9. The spectra in figure 3.9 are the averaged result from three runs at each condition. The spectra are plotted as contour plots with the horizontal axis corresponding to non-dimensional wavenumber and the vertical axis corresponding to wave period (moving upwards is moving forward in time). Each of the figures has the same vertical color scale. Although these spectra do not show any clearly dominant wavelengths, some general observations can be made. Comparing the spectra for $\bar{f} = 1.40$ and 1.26 Hz (figures 3.9(a) and (b), respectively) we see significantly broader peaks that stretch to higher wavenumber, implying an assortment of smaller wavelength ripples (note that for $\bar{f} = 1.26$ Hz, $k\bar{\lambda} = 200$ implies a ripple wavelength of about 3 cm). For $\bar{f} = 1.26$ Hz the peaks are also more elongated in the vertical direction, indicating that these wavelengths persist for longer times during breaking. Comparing $\bar{f} = 1.26$ and 1.15 Hz (figures 3.9(b) and (c), respectively) we see the emergence of much stronger peaks in the range $200 < k\bar{\lambda} < 300$. These wave components gradually fade out as breaking progresses.

Finally, it seems worth noting that the time delay between when breaking begins (again, defined as when the toe first starts to move) and the emergence of significant peaks in the spectra appears to grow with the wavelength. In (a) peaks begin to appear at around $t/T = 0.3$ while for (b) and (c) they appear at around 0.35 and 0.4, repectively. This means that it takes an increasingly longer time for

the cross-stream ripples to be measured by the light sheet, which is approximately at the wave crest when breaking begins. It is unclear what exactly causes this increased delay; perhaps it takes longer for the breaking region to develop, or the surface ripples have a higher phase-speed relative to the carrier wave, so it takes them longer to be "swept" back over the crest. We believe this increase in delay time to be a real, however it should be noted that it is difficult to determine the precise distance between the crest and the laser sheet, in particular because the crests are highly rounded due to surface tension and the wave shape is continuously deforming. A better understanding of this phenomenon might require further investigation.

3.4.2 Amplitude dependence

Figure 3.10 shows plots of $\bar{z}/\bar{\lambda}$ and $\sigma/\bar{\lambda}$ for five different wave-maker amplitudes with $\bar{f} = 1.26$ Hz. Each curve is the average of at least two runs and they have been slightly adjusted horizontally so that the location of the first local minima of $\bar{z}$ coincide. Finally, the curves of $\bar{z}$ have been offset in the vertical for clarity. The plot shows that as the wave-maker amplitude increases, the period of the streamwise ripples increases. For example, for $A/\bar{\lambda} = 0.0514$ the spacing between the first two minima of $\bar{z}$ is roughly $\Delta t = 0.08T$ whereas for $A/\bar{\lambda} = 0.0522$, we find $\Delta t = 0.10T$, an increase of about 25%. While the actual amplitude of the wave does not increase substantially with $A/\bar{\lambda}$ the breaker appears noticeably stronger, almost forming a small jet at $A/\bar{\lambda} = 0.0522$. The typical cross-stream ripple amplitude also increases with wave-maker amplitude, as is evident from the curves of σ in

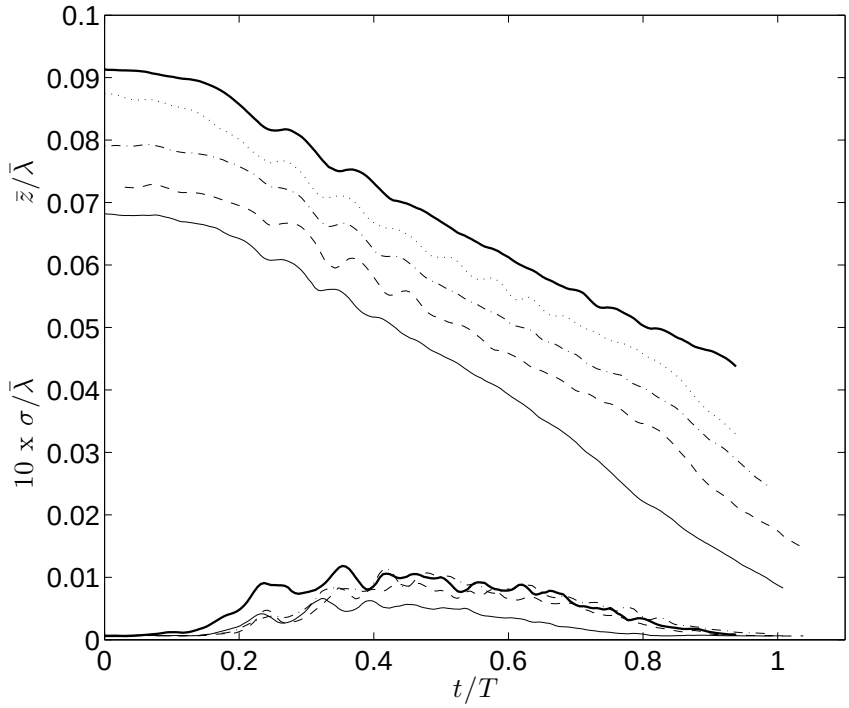

Figure 3.10: Plot $\bar{z}/\bar{\lambda}$ and $\sigma/\bar{\lambda}$ versus t/T for $\bar{f} = 1.26$ Hz and with 5 different wave-maker amplitudes. The curves of $\bar{z}$ have been offset successively by 0.04 in the vertical for clarity. Starting from the bottom they are $A/\bar{\lambda} = 0.0514$ (solid), 0.0516 (dashed), 0.0518 (dashed-dotted), 0.0520 (dotted), and 0.0522 (bold solid). Note that the values of σ have been scaled by a factor of 10. Each curve is the average of at least 2 runs.

figure 3.10. Averaging the values of σ over the time-period from the location of the first maximum of σ to the time when breaking begins to slow (say from roughly $t/T = 0.24$ to $t/T = 0.5$), we find that the averaged maximum $\bar{\sigma}$ increases fairly linearly with wave-maker amplitude $A/\bar{\lambda}$, see figure 3.11, ranging from about 0.5 to 1.0 mm. Note that in figure 3.11, $\bar{\sigma}$ is dimensional.

Slope spectral histories for these five different wave-maker motions are shown in figure 3.12. The wavenumber is nondimensionalized by the wavelength $\bar{\lambda}$ and time by the wave period T. Each set of contours is the average result of at least

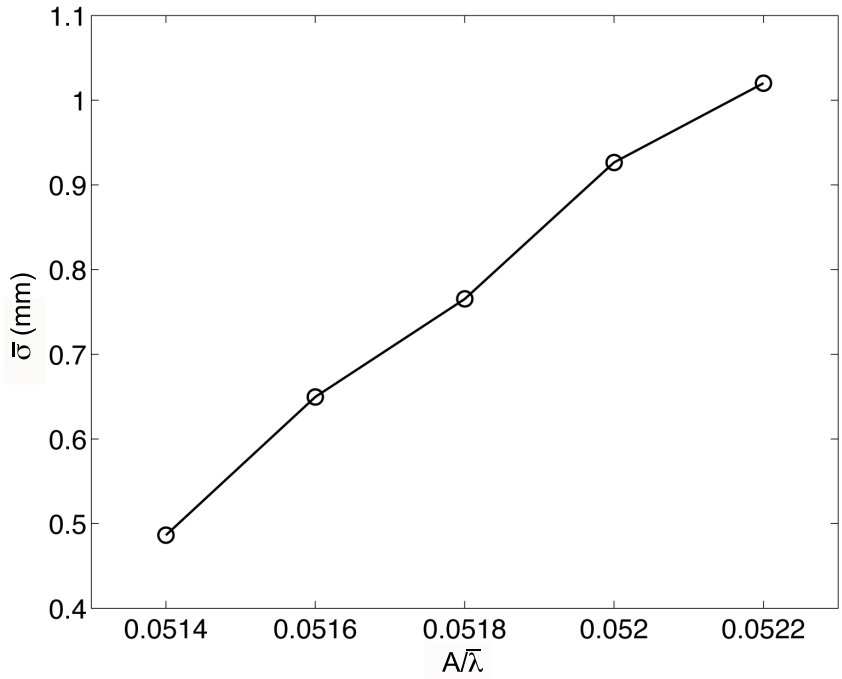

Figure 3.11: Plot of $\bar{\sigma}$ versus $A/\bar{\lambda}$ for $\bar{f} = 1.26$ Hz. $\bar{\sigma}$ is the value of σ from figure 3.10 averaged over the range $0.24 < t/T < 0.5$. The solid line connects consecutive points. Note that $\bar{\sigma}$ is dimensionl.

two runs and each has the same vertical scale. For these wave conditions, $k\bar{\lambda} = 200$ corresponds to a wavelength of roughly 3 cm. As the wave-maker amplitude is increased, clearer peaks begin to emerge in the wave spectra. These peaks are concentrated mostly in the range of $150 < k\bar{\lambda} < 400$, or about 4 cm down to about 1.5 cm in wavelength.

3.4.3 History of the surface gradient and curvature

In addition to profile and spectral histories, the time variation of the surface gradient, surface curvature, and the gradient of the surface curvature can also be computed. In addition to being useful quantities in their own right, as they are a

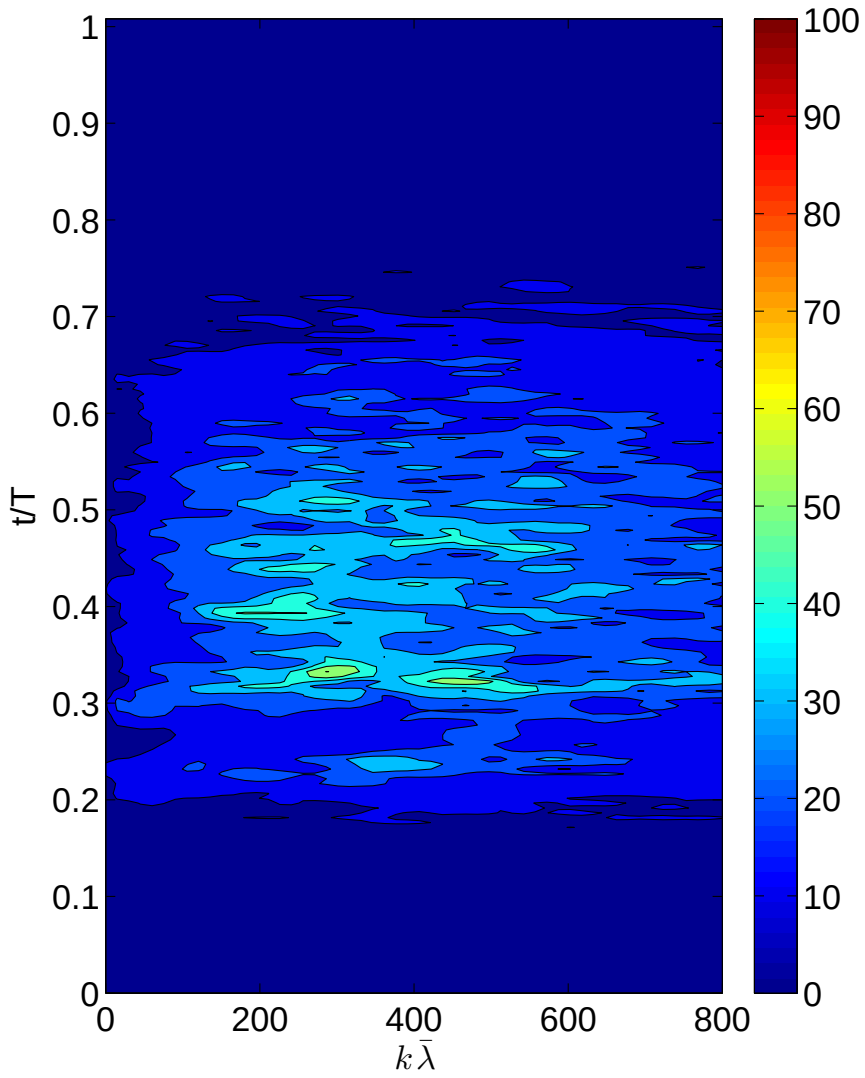

(a) For caption see page 76

Figure 3.12

measure of high-frequency surface components, measuring surface derivatives might provide some physical insight into the underlying flow. For example, as was discussed in Chapter 1, the pressure near a free surface can be broken down into terms involving the surface curvature (i.e. a jump in pressure caused by capillary forces),

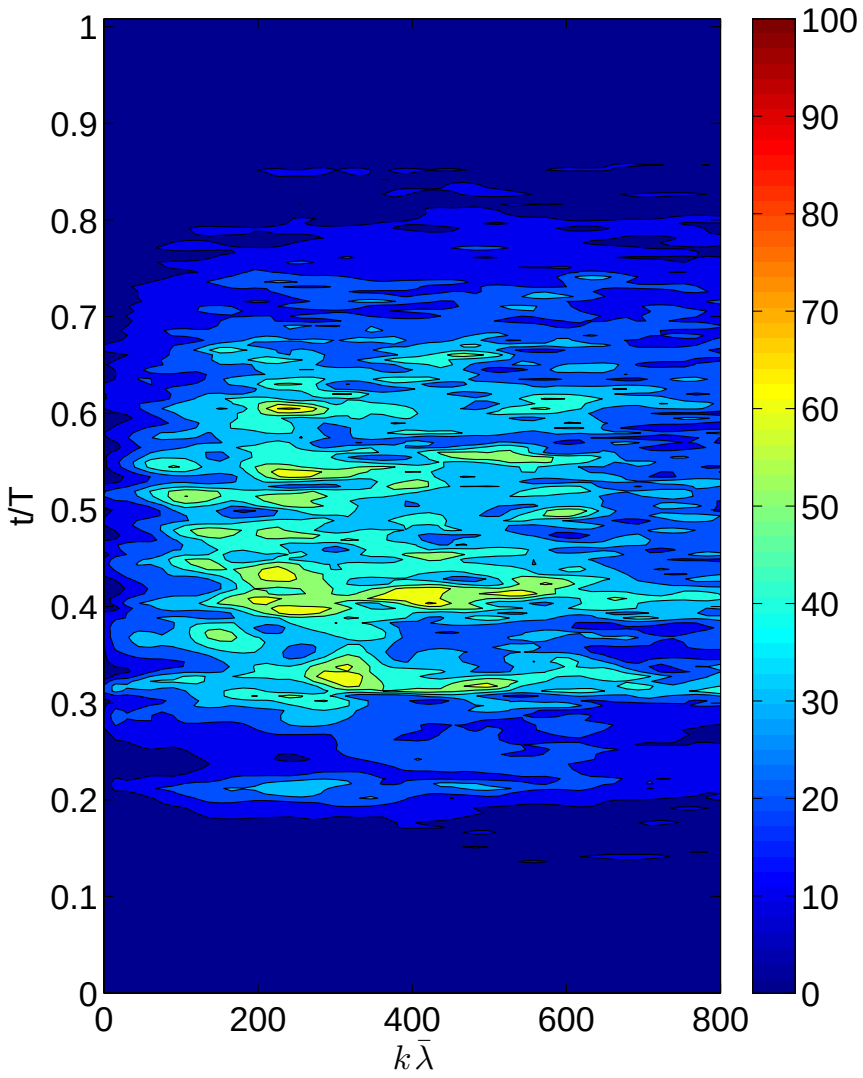

(b) For caption see page 76

Figure 3.12

the surface height (i.e. hydrostatic pressure) and residual dynamic pressure (see equations 1.3 and 1.6). Therefore, gradients of such quantities could be related to pressure gradients, which are in turn related to fluid accelerations. Such a connection between surface ripples and underlying fluid motions has been investigated by

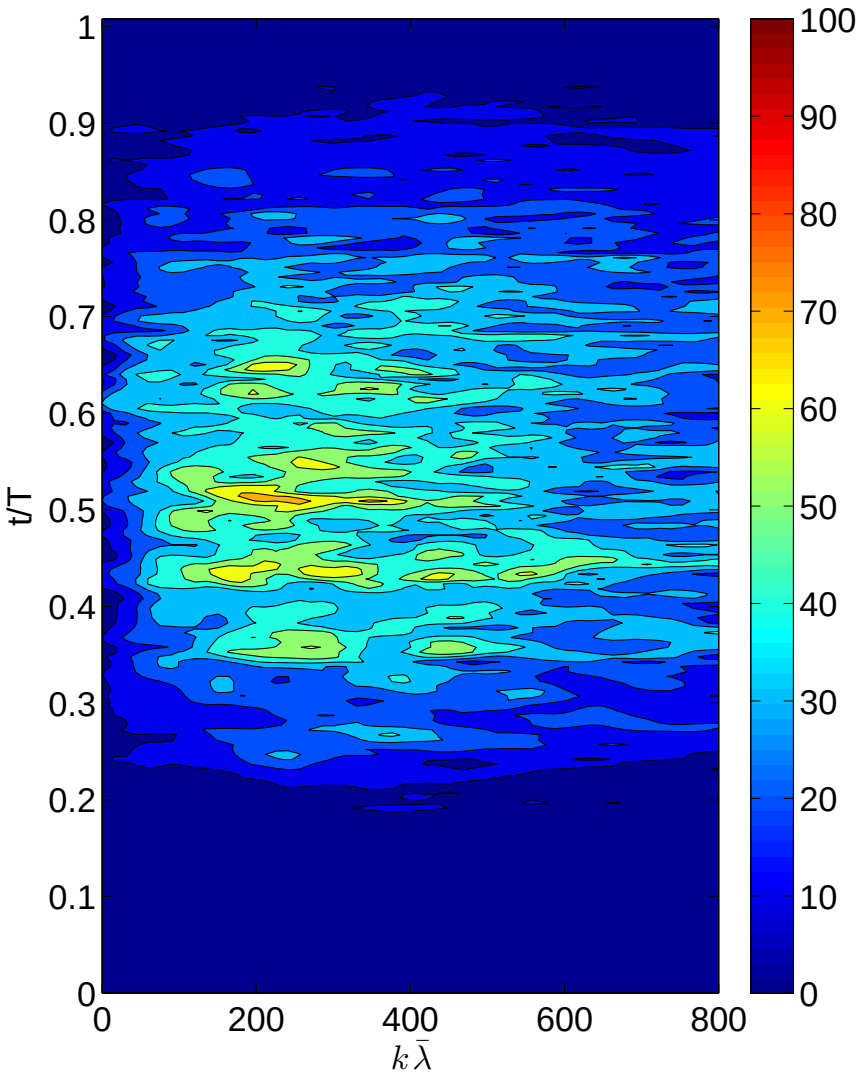

(c) For caption see page 76

Figure 3.12

other authors ([93], [94], [95], [96], [97, 98]), although no clear consensus on the precise origin of surface ripples has emerged, and the physics may be dependent on the details of the flow. Furthermore, in our experiments the flow field is highly unsteady and information is only obtained along one-dimension, so full measurements

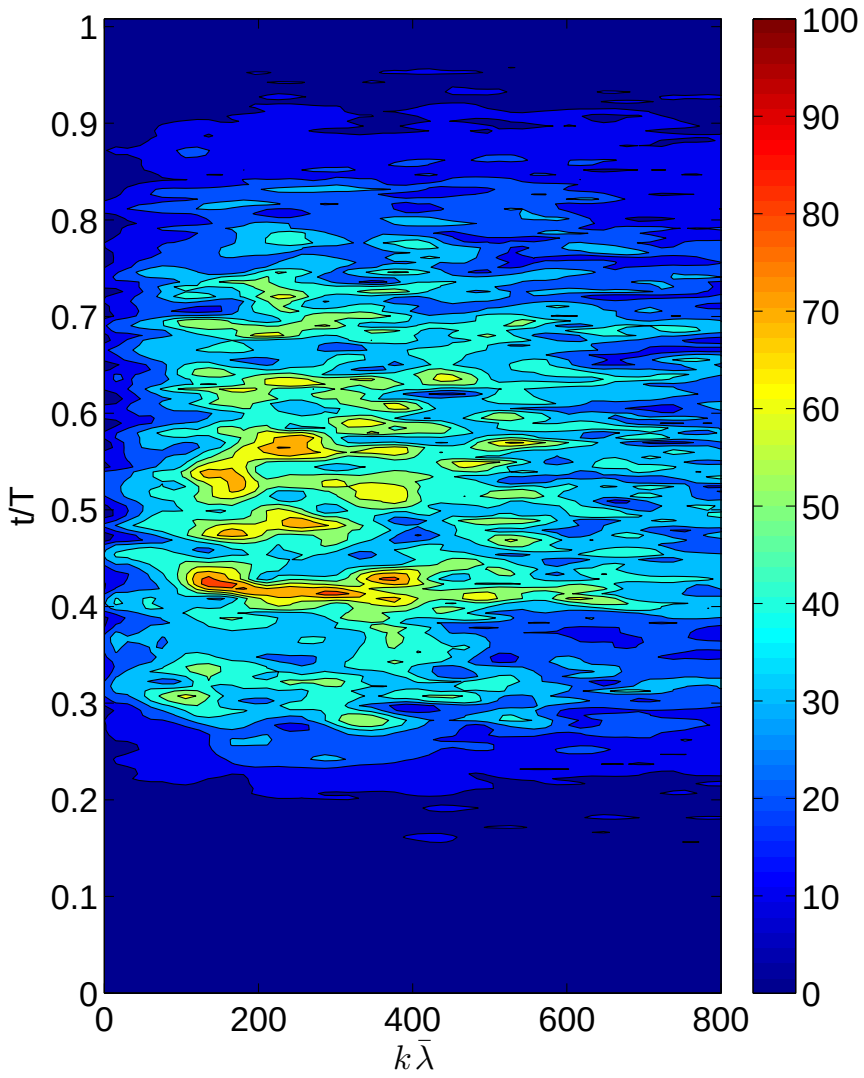

(d)

Figure 3.12: Cross-stream spectra history for $\bar{f}$=1.26 Hz and four different wavemaker amplitudes $A/\bar{\lambda}$. (a) 0.0514, (b) 0.0516, (c) 0.0518, (d) 0.0520. The case with $A/\bar{\lambda}$=0.0522 is shown in figure 3.9(b). Each plot shows spectra for one wave period post-breaking.

of surface gradients are not possible. Nevertheless, we found that profile histories of various 1D surface derivatives yielded some interesting results that may elucidate certain features of the cross-stream structure in the spilling zone.

The gradient, curvature, and gradient of curvature histories are created in the following way. For each raw cross-stream profile, the horizontally averaged mean was first removed, and derivatives along the y direction were computed numerically. Each time a raw gradient was computed, the result was smoothed using a moving average filter to reduce noise, and the subsequent gradient was computed from this smoothed result. Each resulting profile is then be plotted above the previous to create a history of that quantity (gradient, curvature, etc.) However, instead of plotting each profile as a separate line (as in the profile histories of figure 3.8), the profiles can be "meshed" together to form a surface in the $y/\bar{\lambda}$-t/T plane. This resulting surface is then colored according to its value on a gray scale, with white being the highest values and black being the lowest. Figure 3.13 contains a series of plots showing such histories for a particular experiment with $\bar{f} = 1.15$ Hz and $A/\bar{\lambda} = 0.0522$. The plots correspond to: (a) the surface height h (with the mean removed), (b) the surface gradient, (c) the surface curvature ($\kappa = \partial^2 h/\partial y^2/[1 + (\partial h/\partial y)^2]^{3/2}$), and (d) the gradient of the surface curvature. In the plots of figure 3.13, data at a constant t/T value are from one profile, while the data at a constant $y/\bar{\lambda}$ value are from profiles taken at different times. Therefore, these plots show the temporal behaviour of a 1D cross-stream profile and its 1D derivatives taken in a frame of reference moving with the crest, *not* an instantaneous view of the water surface or its 2D gradients.

The dashed black lines in figures 3.13(a)–(d) correspond to the time when the value of $\bar{z}$ is at a local minimum (see the discussion of figure 3.6). The history of the surface height (figure 3.13a) shows natural horizontal striations (at least for

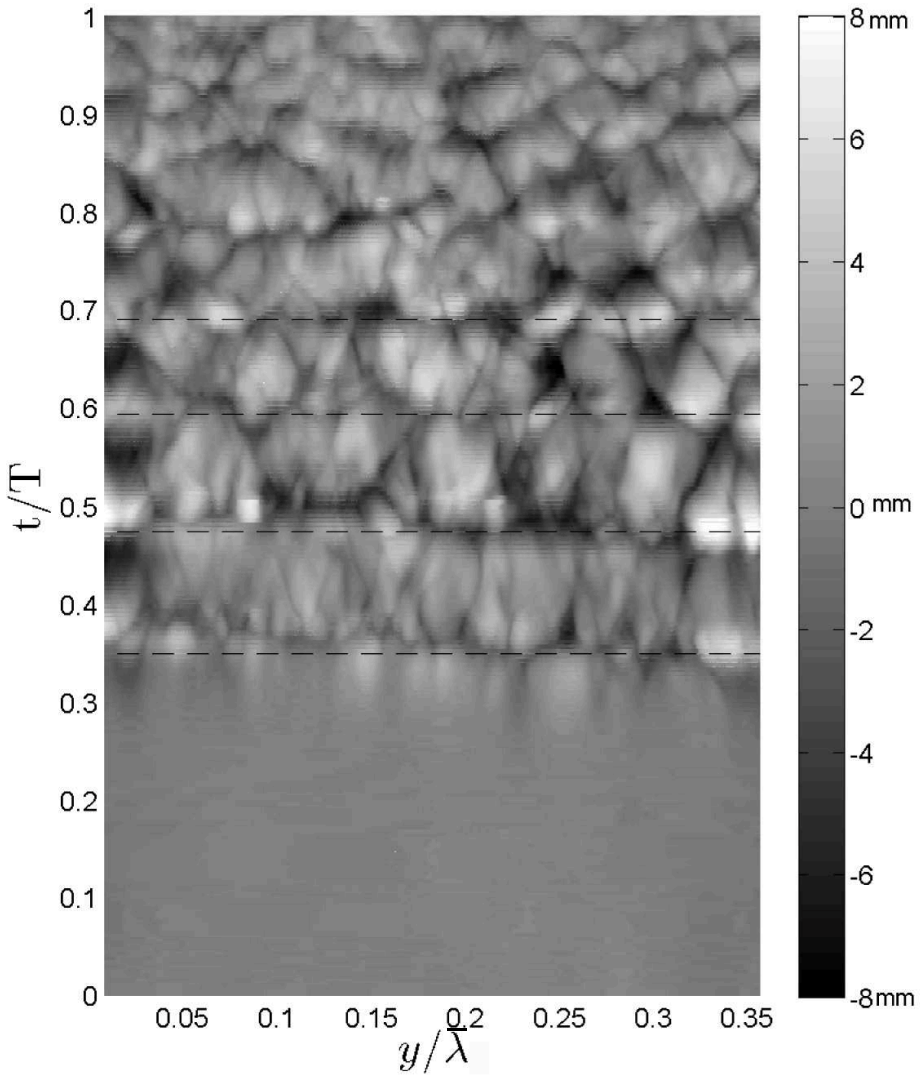

(a) For caption see page 81

Figure 3.13

$t/T < 0.5$) which appear to coincide with the minimum of $\bar{z}$. Interestingly, when $\bar{z}$ is a minimum, the cross-stream surface does not appear to have very many large amplitude surface features, even though σ peaks at these locations (see again figure 3.6). This means that when $\bar{z}$ is at a minimum, the cross-stream surface rippes

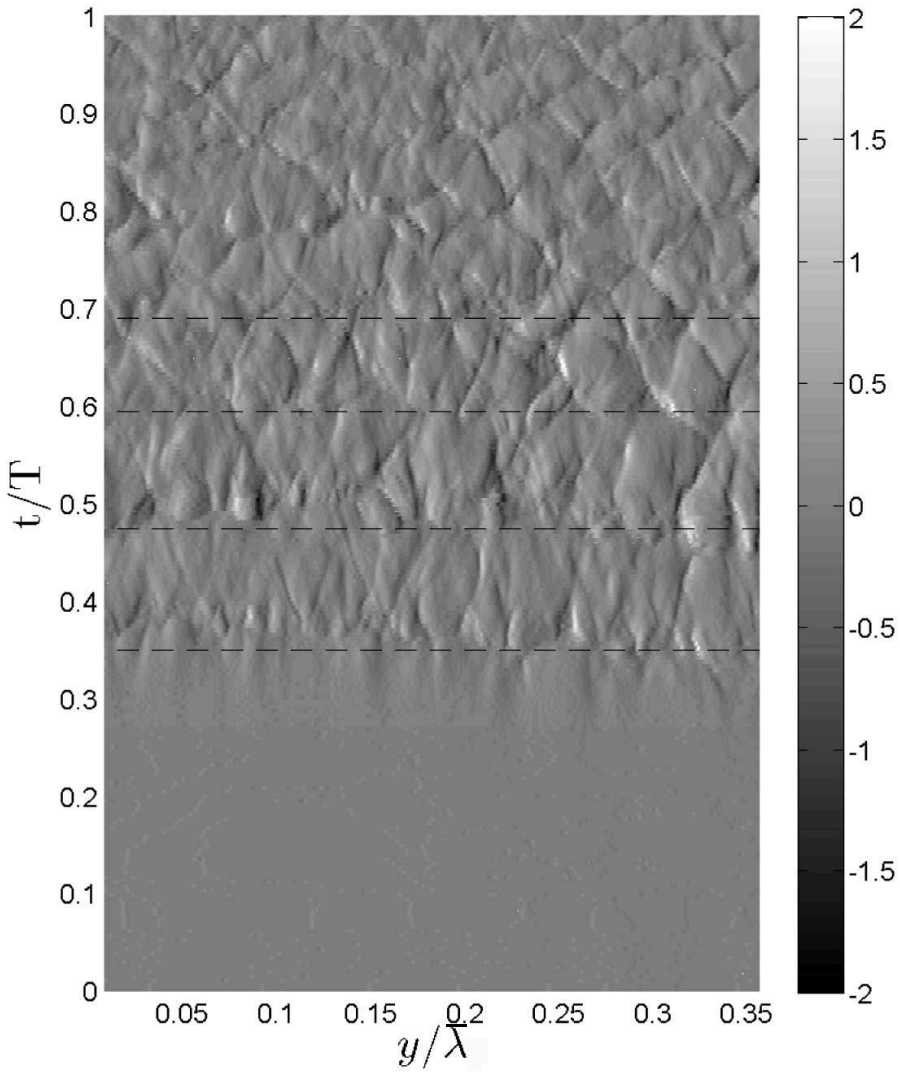

(b) For caption see page 81

Figure 3.13

are small, but numerous and highly fluctuating so as to create a large standard deviation. This conclusion is supported by the fact that the plots of the surface gradient and surface curvature (figures 3.13b and c) show large values near these locations. Furthermore, the histories of surface gradient, surface curvature, and the

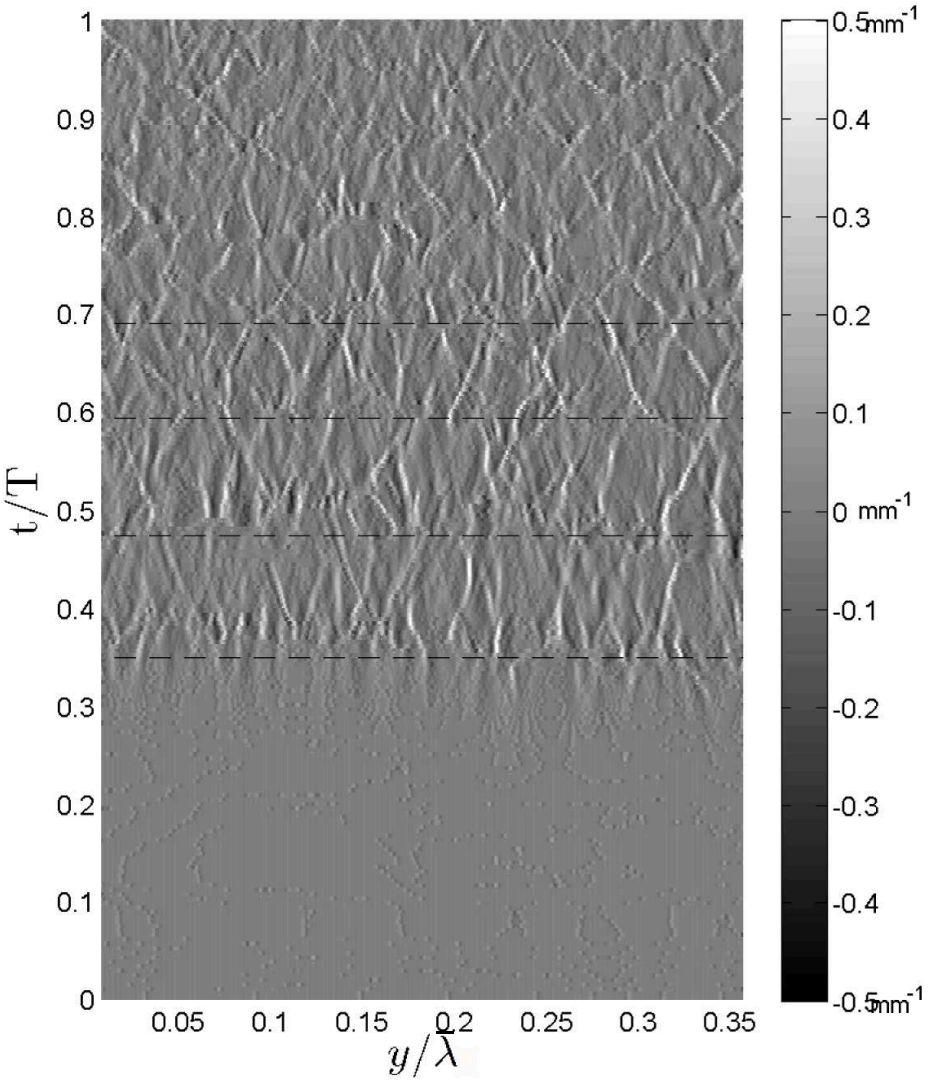

(c) For caption see page 81

Figure 3.13

gradient of surface curvature all show the presence of thin, "scar-like" lines where the surface shape changes sharply. Some of these scars have small y velocity components, as evidenced by their less than vertical slope in $y/\bar{\lambda}-t/T$ coordinates, but on average do not appear to have a preferential right-left direction. The generation of these scars

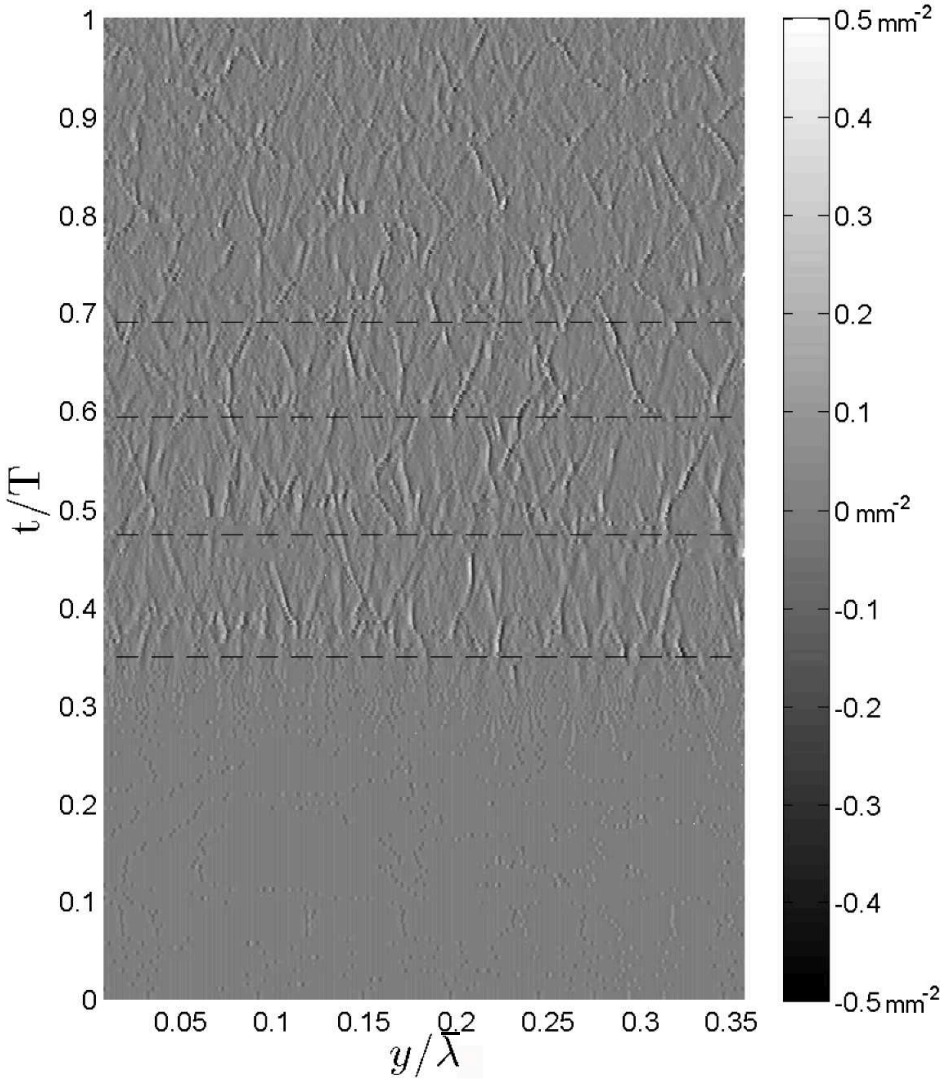

(d)

Figure 3.13: Histories of the cross-stream amplitude and its varioius derivatives for one run with $\bar{f} = 1.15$ Hz and $A/\bar{\lambda} = 0.0522$. (a) surface height h (with the mean removed), (b) surface gradient $\partial h/\partial y$, (c) surface curvature $\kappa = \partial^2 h/\partial y^2/[1+(\partial h/\partial y)^2]^{3/2}$, (d) gradient of surface curvature $\partial\kappa/\partial y$. The dashed black lines correspond to the time when the value of $\bar{z}$ is at a minimum.

seems to coincide with the location of the minimum of $\bar{z}$ and can persist for up to as much as one-tenth of a wave period in a frame of reference moving with the crest.

It is a bit difficult to accurately identify what exactly should be considered a scar or not, as their density, strength and length show variation across the image, so any method to determine their spacing would be rather coarse. Regardless, based off of visual inspection of the surface at around 0.35 wave periods, we measure an average spacing of roughly 0.026 wavelengths (3 cm). In as far as the sum of these quantities represents acceleration and deaccleration of the fluid in the cross-stream direction, it may be that the formation of these surface scars are connected with the presence of high or low speed "streaks" in the fluid near the free surface. Such streaks have been observed near the crests of steep waves in wind-wave experiments ([55]) and in more recent numerical calculations ([88]). The latter work identified an average spacing between the streaks to be about 0.6 cm for initial gravity wavelengths of 7.5 cm (a ratio of 0.08). Looking more closely at the curvature plot (figure 3.13c) we see that these thin scars are predominately positive, indicating regions of high-upward curvature. Such curvatures are reminscent of steep capillary waves which have large upward curvatures in the wave troughs, as opposed to gravity waves which have large negative curvature at the wave crests. Although the size of the cross-stream ripples precludes them from being pure capillary waves it is clear that the dominant contributions to the surface curvature are coming from the troughs of the cross-stream ripples. A better understanding of these surface features further investigation.

We conclude with a discussion of one possible mechanism that may account for the formation of the observed cross-stream ripple pattern. PIV measurements of both steady and unsteady breakers have shown the presence of a separated shear

layer just upstream of the breaking region. This shear layer introduces cross-stream oriented vorticity that viscously diffuses outward with distance away from the leading edge of the layer (and with time in the unsteady case); see for example the measurements of [36] or the experiments and numerical calculations of [86, 87]. Consider the simple scenario of a series of co-rotating vortices that are generated at the leading edge of the shear layer and located near the free-surface. Arrays of similar such vortices have been observed in PIV measurements of steady spillers ([34], [35]) and in the unsteady spillers of [36]. Next consider these vortices to be near the larger quasi-2D streamwise ripples, as depicted in figure 3.14. Although there is no definitive justification for such a choice, it was shown by [100] that an array of co-rotating vortices near a free surface would create a "vortex wave" with the wave elevated above the vortex core. We see that with such a configuration the troughs of the streamwise ripples are regions of very high shear, and one might expect large turbulence fluctuations (and hence ripple production) in these areas. Furthermore, such a scenario could result in the formation of smaller streamwise oriented vortices in the region between the main vortices, a situation analagous to the observed streamwise "braid" vortices that stretch between the larger turbulent rollers in mixing layer turbulence. The presence of elongated streamwise vortex structures could help explain the production of cross-stream ripples and surface scars in the troughs of the larger streamwise ripples.

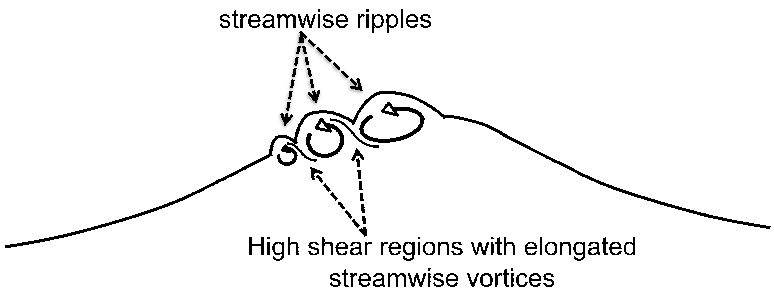

Figure 3.14: A schematic showing a possible model for the distribution of vorticity in the shear layer produced by a spilling breaker showing the location of high shear regions in the troughs of the streamwise ripples.

3.5 Summary and conclusions

In this work, the cross-stream structure of the rippled surface generated by short-wavelength spilling breakers was investigated experimentally. An LIF method was used to measure two-dimensional surface profiles in a frame of reference moving with the breaker crest. Three different wave-maker frequencies and five different wave-maker amplitudes were investigated. With these five amplitudes the waves vary from weak spillers to nearly plunging breakers at the largest amplitude and wavelength. The wave-maker motions were Froude scaled and the changes in the cross-stream statistics are the result of the turbulence generated in the breaker and surface tension. For all the wave conditions studied, it was found that the average cross-stream water height $\bar{z}$ shows periodic oscillations once breaking begins. These oscillations in wave height are due to the generation of larger, "quasi-2D" streamwise ripples that are oriented nearly parallel to the wave crest. These ripples do not Froude scale as they are generated by the underlying turbulent flow. Both the amplitude and the period of these larger ripples increase with wavelength and wave-maker amplitude, with the depedence on wavelength being the stronger of the

two. The standard deviation of the amplitude of the cross-stream ripples also show distinct peaks in the early stages of breaking. These peaks are found to coincide with the local *minima* of $\bar{z}$, indicating that the cross-stream ripples are strongest in the regions *between* the larger streamwise ripples. In these regions, the cross-stream ripples appear small and numerous with rapid changes in slope and curvature, rather than broad and large. A measure of the typical amplitude of the cross-stream ripples generated during breaking was found to increase with $\bar{\lambda}^3$ and linearly with the wavemaker amplitude A. In dimensional terms, the observed cross-stream ripples were in the range of 0.5 – 2.0 mm in amplitude. The cross-stream ripples, which are small in the initial stages of breaking, grow rapidly and are largest at about half a wave period after breaking begins. For the weakest breakers studied, the cross-stream ripples remain small relative to the streamwise ripples, and the flow remains essentially 2D. For the strongest breakers, the cross-stream ripples can grow to be almost half the height of the streamwise ripples, so 2D approximations in these larger breakers may fail to capture significant physics. Wavenumber spectra histories of the cross-stream profiles reveal the presence of broad spectral peaks, in particular at the intermediate wave condition, with wavelengths as low as 3 mm up to as high as 45 mm. The spectra appear much more concentrated at lower wavenumber for the largest wavelength studied.

Plots of the surface gradient and curvature show the presence of distinct surface "scars"; thin, persistent regions where the surface fluctuations are large. These features are primarily generated in the regions between the large streamwise ripples and remain for as long as 0.1 wave periods in a frame of reference moving with the

crest. The dominant observed features have high upward curvature, implying the presence of sharply curved troughs, similar to steep capillary waves. It is hypothesized that the scars might correspond to the location of near surface high and low speed "streaks" that are a common feature of many canonical turbulent flows and have been observed near the crest of steep gravity-capillary waves. Based on these observations, a simple model for the vortical flow near the crest of spilling breakers is conjectured.

Chapter 4

Non-linear gravity-capillary waves generated by a moving pressure source[1]

4.1 Abstract

The wave pattern generated by a pressure source moving horizontally over a free liquid surface was investigated experimentally using a combination of cinematic shadowgraph and laser induced fluoresence (LIF) measurements. The pressure source moves at speeds below the minimum phase speed for linear gravity-capillary waves c_{min}. At these speeds, freely-propogating, three-dimensional, nonlinear solitary waves, or "lumps", are known to exist theoretically. In the experiments, several distinct responses are found depending on the speed and magnitude of the applied forcing. At low speeds, regardless of forcing, the pattern exhibits no wave-like behavior and the response resembles the stationary state. However at a critical speed, but still below c_{min}, there is an abrupt transition to a wave-like state that features a marked increase in the response amplitude and the formation of a fully-localized solitary depression downstream of the pressure forcing. This solitary depression is steady, elongated in the cross-stream relative to the streamwise direction, and qualitatively resembles the freely-propogating solutions reported in numerical computions. The speed where this transition occurs decreases with increased forcing

[1]Some of the work presented in this chapter can also be found in Diorio *et al.*, *Physical Review Letters*, 2009 [101]

indicating that nonlinear effects are important over a wider range of the parameter space. For speeds very close to the transition point time-dependent oscillations are observed and their dependence on speed and forcing are reported. The amplitude of the solitary depression decreases with speed and is independent of the level of forcing, indicating a one-to-one relationship between amplitude and phase speed, a known feature of solitary waves. As the speed approaches c_{min} a second transition is observed. The steady solitary-depression gives way to an unsteady state characterized by the periodic shedding of localized depression waves from the tails of a "V" shaped pattern. These results are the first experimental evidence of the bifurcation of 3D gravity-capillary solitary waves and are discussed in connection with recent theoretical and numerical results on the nature of solitary waves in nonlinear dispersive systems.

4.2 Summary of previous work

As was discussed in Chapter 1, in the presence of both surface tension and gravity, water waves are governed by the well-known dispersion relation

$$\omega^2 = \left(gk + \frac{\tau}{\rho} k^3 \right) \tanh(kH) \tag{4.1}$$

where H is the fluid depth. This dispersion relation holds for a train of linear waves (i.e. infinitesimal amplitude). As shown in Chapter 1, an interesting feature of this dispersion relation is that the phase velocity obtains a minimum depending on the value of the Bond number, $Bo = \tau/(\rho g H^2)$. For $Bo \gg 1/3$ (shallow water), the minimum occurs in the long wave limit, $k_{min} = 0$, and has a minimum phase

speed $c_p^{min} = (gH)^{1/2}$. For $Bo \ll 1/3$ (deep water), the minimum occurs at a finite wavenumber, $k_{min} = (\rho g/\sigma)^{1/2}$, with minimum phase speed $c_{min} = (4g\sigma/\rho)^{1/4}$, or about 23 cm/s in clean water.

The physical implication of this phase speed minimum is that for an object moving moving at a constant velocity slower than c_{min}, no (linear) waves are generated. Knowledge of this minimum in the phase speed has certainly been noted (e.g. [102], [103]) but interest in the behavior of nonlinear waves near this condition has begun to generate more interest lately. Because the phase and group velocities are equal there (see Chapter 1), extrema of $c(k)$ are known as bifurcation points of non-linear solitary waves. In fact, long wavelength solitary waves in shallow or finite depth water, both for pure gravity and gravity waves with surface tension, are some of the oldest nonlinear phenomena in fluid mechanics ([104], [105], [106]). Solitary-type envelope solutions for pure gravity waves in deep water have also been reported ([107, 108], [109]). However, it was not until the late 1980s and early 1990s that researchers began to tackle the problem of gravity-capillary solitary waves in deep water. This began with the numerical computations of solitary-wave profiles by [24]. Later work made use of the Nonlinear Schrödinger (NLS) equation as a model to compute the wave amplitude near the minimum phase speed ([26] and [25]). One of the important results found was that at the minimum phase speed, linear periodic waves bifurcate into envelope-solitons of permanent form of which the profiles computed by [24] were merely a special case. Section 3 of [110] presents a comprehensive review of the early work in this area.

The early mathematics of gravity-capillary solitary waves mostly considered

2D solutions, that is, the variation of the amplitude along a 1D line[2]. However, many of the mathematical models being used, such as the NLS or KdV equations, have 3D analogs that permit solutions with weak cross-stream variation; the 2D NLS and Kadomstev-Petviashvili (KP) equation, respectively ([111]). Therefore, it would seem plausible that gravity-capillary solitary waves may exhibit 3D behavior as well. This 3D extension was applied to the water wave problem by [2] using a generalized Benney-Luke equation, an extension of the KP equation that included surface tension and topographical forcing. Their calculations showed a solitary wave whose streamwise profile resembled the 2D "plane wave" solutions, but also remained confined in the transverse (cross-stream) direction, see figure 4.1. These "lump" solutions, however, are typically computed from equations that depend on long-wavelength assumptions (KP equation), have arbitrary phase between the envelope and carrier wave (NLS), or are only weakly non-linear (KP and NLS) and therefore are not useful in deep water (where k_{min} is finite) or at larger amplitudes. Therefore, one of the main goals of recent research has been to develop models that capture the three-dimensional solitary wave physics in deep water (i.e. $Bo \ll 1/3$).

In 2005, three different groups presented advances in this area. [28] used an asymptotic approach, similar to that used by [112] and [113] for 3D gravity wave packets, to construct small-amplitude wave-packet lumps that travelled slightly below the minimum phase speed for Bo less than (but still near) 1/3. The results of this analysis showed that two solutions, one with a central depression and one

[2]Some authors refer to these types of waves as "1D solutions", and waves that vary in both x and y as "2D", so that the remaining dimension (z or height) is implied. Here we adopt the convention that the term 2D corresponds to height variation along a line, and the term 3D to height variation along a surface.

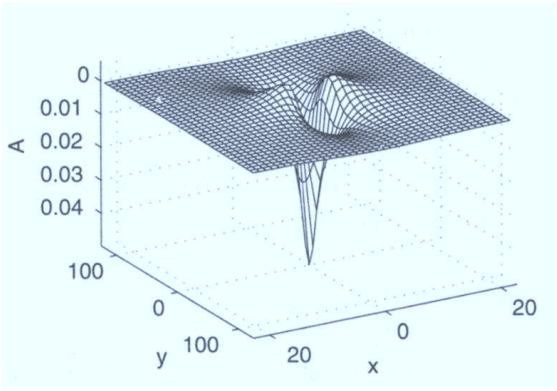

Figure 4.1: Figure 1 from [2] showing a lump solution to the KP equation for $Bo > 1/3$. Note that the scale in y is much larger than the scale in x so the wave is much broader in the y (cross-stream) direction.

with a central elevation, bifurcate at the minimum phase speed, analogous to the bifurcation of plane-waves in 2D. [27] also computed 3D localized wave packets on water of infinite depth from the full Euler equations by means of a boundary integral method. In the small amplitude limit, these waves behave like wave-packets, consistent with the asymptotic results of [28]. At higher amplitudes, the waves transform into completely localized disturbances, resembling the 2D solutions computed by [24]. Finally, [114] also showed that travelling solitary wave packets exist, with continuous solutions spanning the range from the long wave limit, where they are governed by the KP equation, down to the wave-packet limit, governed by the Davey-Stewartson model. [115] continued their work by studying the generation of lumps in a two-layer fluid system, where the upper layer is bounded by a rigid wall. This system also features a phase speed minimum at finite wavenumber and is governed by the 2D Benjamin equation ([116]). [115] showed that in the neighborhood of the minimum, the problem resembles that of free-surface lumps. [117]

investigated the same problem using their boundary integral method applied to the full non-linear equations, and confirmed the results of the weakly non-linear model of [115]. Most recently, [118] developed a new model equation that mimics the behavior of the Euler equations near the minimum phase speed and at a finite wave number (i.e. fully deep water limit). It was shown that all 2D solitary waves are unstable to transverse perturbations and evolve into lumps, analogous to transverse instabilities observed in shallow water. [118] also investigated the stability of the lump solutions themselves, showing that elevation type lumps are unstable, while depression type lumps are stable at larger amplitude. This last result is commensurate with the result of [119] who investigated the stability of lumps with $Bo \approx 1/3$ with a 5th-order KP equation.

Some numerical researchers have included forcing in their models in order to simulate a moving pressure source. [120] examined the surface waves generated by a moving pressure source with $Bo < 1/3$ but finite depth. A 2D boundary integral method was applied to the fully non-linear equations to show that depression and elevation type waves exist under both zero and non-zero forcing. [121] used a similar technique but in 3D and with the inclusion of an artificial viscosity. Although their work focused mostly on the super-critical case (i.e. $c > c_{min}$), the solitary waves profiles computed below c_{min} had a shape that was slightly asymetric with respect to the streamwise direction. The main wave trough moved slightly behind the forcing and the elevation of the leading edge became higher than the trailing edge. Their results also showed that the maximum amplitude of the wave pattern transitioned smoothly from $c < c_{min}$ to $c > c_{min}$. This is in contrast to their earlier work ([122])

for the case of zero viscosity which showed a minimum value $c^* < c_{min}$ such that no solutions existed for $c^* < c < c_{min}$, and time-dependent solutions could be expected.

A model that has been used in comparison with the current experiments is that developed recently by Cho and Akylas [101]. Instead of using the 2D fully nonlinear viscous water-wave equations, these authors employ a simple model equation that captures the interplay between nonlinear and dispersive effects in the region near the minimum phase speed. Briefly, following the work of [123], one can expand the dispersion relation to second order around k_{min} and add an imaginary part to represent the wave decay rate due to viscous damping, see [102]. This yields

$$\omega = -i\tilde{\nu}\,|\mathbf{k}|^2 - \frac{1}{4}sgn(k)(1 + 2\,|k| + k^2 + 2l^2) \tag{4.2}$$

where the parameter $\tilde{\nu} = \nu(4g)^{1/4}(\tau/\rho)^{3/4}$, ν being the kinematic viscosity; in cgs units, $\nu = 0.01$, $g = 981$, $\rho = 1$ and $\sigma = 73$, so $\tilde{\nu} = 0.003$. Equation 4.2 can be combined with a moving pressure forcing, $A'p(\xi, y)$, $\xi = x + \alpha t$, where α is a nondimensional speed parameter $\alpha = c/c_{min}$ where c is the speed of the applied pressure forcing. Assuming quadratic nonlinearity [123], the following equation for the free-surface elevation $\eta(\xi, y, t)$ is obtained

$$\eta_t - \tilde{\nu}(\eta_{\xi\xi} + \eta_{yy}) - (\frac{1}{2} - \alpha)\eta_\xi - \frac{1}{4}H\{\eta_{\xi\xi} + 2\eta_{yy} - \eta\} - \beta(\eta^2)_\xi = A'p_\xi \tag{4.3}$$

Here, A' denotes the peak amplitude of the applied forcing and $H\{f\} = F^{-1}\{-isgn(k)F\{f\}\}$ stands for the Hilbert transform, with

$$F\{f\} = \frac{1}{2\pi}\int_{-\infty}^{\infty} f(x)e^{-ikx}dx \tag{4.4}$$

being the Fourier transform. The coefficient of the nonlinear term in equation 4.3 is set to $\beta = \sqrt{11/2}/8$. This ensures that, for $\tilde{\nu} = 0$ and α slightly below the bifurcation point $\alpha = 1$, free solitary-wave and lump solutions of equation 4.3 agree, to leading order, with their weakly nonlinear counterparts of the full water-wave equations ([28]).

In contrast to the progress in the mathematical formulation of lumps, there has been remarkably little progress made in experiments. [124] observed isolated features with sharp curvatures in gradient images of a wind-wave field. Measured profiles of these features looked similar to the numerical profiles calculated by [24] although no actual velocity of the features was recorded. In a more thorough experiment, [125] used a narrow 2D slit to create an impinging air jet on the surface of a recirculating water channel. A small amount of chalk powder was used to make the free surface visible to a camera positioned on the side of the tank. When the free stream water velocity was below the minimum phase speed, a localized wave formed directly beneath the impinging jet. The shape of the free surface matched very well with the earlier calculations of [24] for 2D solitary waves. Measurements of the surface slope as a function of wave speed also showed good agreement with the theory, although the wave pattern was not completely steady, showing some lateral instabilities, in particular at lower speeds. Measurements were also made of the slope and position of the wave pattern after the air was turned off, so the wave became a freely propagating wave damped by viscosity. The surface slope decreased as a function of time and the wave moved upstream, indicating an increase in velocity with decreasing wave slope, another result consistent with the theory. More recently, [126] measured

the properties of the wave packet generated by a water drop on a free surface. A localized wave packet was found that propagated at constant velocity and with little diffusion. The wavelength of the carrier waves and the group velocity of the packet were near the minimum of the dispersion curve, so it is plausible that the waves observed were solitary waves.

To the best of the author's knowledge no other experimental work has been done on deep water gravity-capillary solitary waves, while theoretical advancements have been abundant. The results of the experimental works are both qualitatively and quantitatively consistent with the 2D theory, but they do not address the 3D nature of the problem that appears to be so evident in more recent calculations. Furthermore, theoretical and experimental results regarding the unsteady behavior and stability of any lumps that may exist are lacking. Clearly, experiments in this area are long overdue. Therefore, results of experiments looking at the non-linear gravity-capillary wave pattern generated by a moving pressure source travelling below the minimum phase speed are presented in this chapter.

4.3 Experimental details

4.3.1 Experimental setup

The experiments were carried out in a tank that is 7.3 m long, 76 cm wide and 91 cm deep, see figure 4.2. The sides and bottom of the tank were constructed out of translucent glass, and the tank was filled with water to a depth of approximately $H = 60$ cm. The surface tension, measured with a Willhelmy plate, was maintained

at $\tau = 73$ dynes/cm throughout the experiments via a surface skimmer and filtration system, so that $Bo \ll 1/3$ (i.e. deep water). A pipe with inner diameter $D = 2.5$ mm was positioned 1 cm above the water surface and mounted on a translation stage, which is attached to a carriage that rides on top of the tank. The pipe was secured in a silicone slot between two aluminum plates and mounted to the carriage with vibration reducing bushings to prevent the pipe from shaking when the carriage was moving. The carriage was towed by a steel cable attached to a servo-motor and the speed of the motor is controlled by a PC. The carriage is accelerated from rest to a constant speed U_c at an acceleration of 10 cm/s^2. We define a speed parameter, $\alpha = U_c/c_{min}$. This speed parameter was in the range $0.6 < \alpha < 1.03$ for these experiments. Output from a linear displacement position sensor that monitors the position of the carriage as a function of time revealed that the carriage speed varied by less than 0.3% from the nominal speed during an individual run and the average speed varied by 0.01% from run-to-run. A pressure disturbance was made on the water surface by connecting a pressurized airline to the 2.5 mm tube. By controlling the air flow-rate with a flow metering valve, various amounts of forcing were applied. We define a forcing parameter, $\epsilon = h_0/D$, where h_0 is the depth of the water surface depression created by the air-forcing when the carriage is stationary. For these experiments, the forcing parameter was in the range $0.3 < \epsilon < 0.69$. Measurements of h_0 using a high-speed camera showed a variation of about 5% of the mean from run-to-run for a given forcing, see the discussion in section 4.3.2.

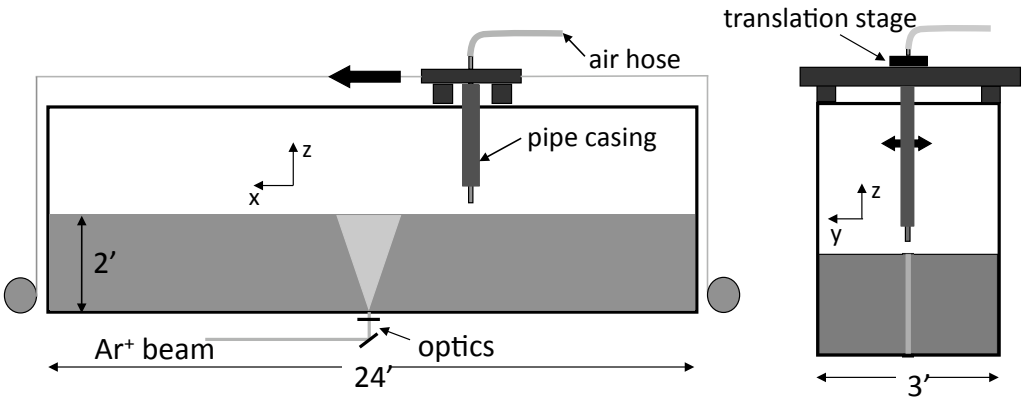

Figure 4.2: Schematic of the experimental setup used in the solitary wave experiment. A small pipe (2.5 mm ID) is mounted in a vibration reducing casing and attached to a movable carriage. A pressurized air line pushes air through the pipe to generate a small depression on the water surface. A high-speed camera (not shown) images the pattern from the side. The pipe is towed in the x (streamwise) direction, and is mounted on a translational stage so it can be displaced in the y (cross-stream) direction.

4.3.2 Measurement details

In order to measure the wave pattern, two different techniques were used: laser-induced fluorescence (LIF) and shadowgraph. In the LIF method, Fluourescin dye was added to the water and a small ($\sim$ 5 cm wide and $\sim$ 1mm thick) laser light sheet was projected onto the water surface from below. This light sheet was oriented so that its long axis was in the direction of the carriage motion (i.e. the x or streamwise direction). A high-speed camera (Phantom 9, Vision Research, 1632 x 800 pixels at 800 fps) was positioned outside the tank and remained stationary. The camera imaged the intersection of the laser sheet and water surface from the side and slightly above the mean water level. In this configuration, the camera recorded images as the wave pattern passed by, and these images were then used to track the height of a particular point using the edge detection algorithms described in section

2.3.3. For these experiments, one pixel corresponded to roughly 0.02 mm in the physical plane. Tracking the height of one point as a function of time yields $z(t)$, which, assuming the pattern to be steady, can be converted to a 2D profile, $z(x)$, using the known speed of the carriage and frame-rate of the camera. In this method, the frame rate was set to 500 fps. This processing method was particularly useful for obtaining a "wide" view of the pattern since a large number of images (> 1000) can be taken that captured both the approach and departure of the wave pattern from the measurement area. However, because of lighting limitations, the frame rate was low enough that this method only captured 4 or 5 frames near the center of the pattern, or a streamwise distance of about 2 mm. To obtain a more detailed view in this region, a 2D profile was extracted from a single image near the center of the wave pattern, again using the edge detection techniques described in section 2.3.3. Note that, in the end, both of these analysis techniques yield $z(x)$ for a single movie. Since the pipe was mounted on a translation stage, it could be displaced accurately in the cross-stream (y) direction. Repeating a set of experimental conditions with the pipe at different y-locations yielded several 2D ($z(x)$) profiles that were combined together to form a detailed 3D ($z(x, y)$) picture of the pattern. To ensure that the streamwise (x) location of the pattern was the same at each frame from different movies, the camera was triggered by the passage of the pipe through a laser-photo-diode circuit. The position of the pipe in the high-speed movie was repeatable to within 0.5 mm ($\approx 1/5$ pipe diamters) from run-to-run using this method.

One draw back of the LIF method is that the laser light could become highly refracted in regions of high surface curvature, which were primarily in the plane of

the light sheet, making detailed measurements of quantities such as the maximum depth unreliable. Therefore, in the shadowgraph technique, the camera was repositioned to view the pattern from just below the mean water level and a white light source backlit the image to create contrast between the air and the water. This technique removed the refraction issue and allowed for very detailed measurements of the underwater profile as well as accurate measurement of the maximum depth of the depression. Because the length scales are small ($\sim$ 1 mm) an accurate measure of the mean water level was important. To this end, a checkerboard pattern with diagonal lines was mounted vertically and partially submerged so it could be viewed by the camera below the water surface. The location where the diagonal lines were seen to change direction (because of reflection off of the underside of the free surface) was called the mean water level. With this method we are confident that we can locate the mean free surface to within 5 pixels (0.1 mm in the physical plane). The accuracy of this method, combined with the accuracy of the air-flow monitoring system, is the source of the 5% error in h_0 mentioned above. Shadowgraph measurements were also made with the camera mounted to the carriage. To prevent camera shake in the images, the camera was connected to a custom-made 1/2 inch-thick aluminum plate that acted as a brace for both the camera body and the lens element. This plate was then attached to a ball-mount tripod head (Arca Swiss Monoball) and was attached to the carriage using vibration isolation bushings. Because the camera moved with the pipe in this configuration, it captured any time dependent behavior of the wave pattern at various towing speeds.

4.4 Results and discussion

4.4.1 Behavioral states and a critical jump condition

In order to understand the qualitative shape of the surface wave pattern at various speeds, the high-speed camera was first mounted to the carriage and pictures were taken of the wave pattern from above the water surface. These images, presented in figure 4.3, show the three-dimensional pattern that forms around the pipe as it moves at various towing speeds. In all the photos, the pipe (and hence the forcing) is moving from right to left. The surface is back-lit and the light and dark patterns formed are caused by ridges and depressions with various slopes and curvatures. Roughly speaking, the dark patterns represent downward sloping faces that are blocked from the light and the light patterns are ridges or crests that are well illuminated. At low speeds, 4.3(a), there is a depression located directly beneath the air-jet which is fairly symmetric in the streamwise and cross-stream planes and the pattern resembles the stationary condition. We call this configuration state I. At higher speeds, a trailing wave forms that lags the location of the pressure forcing (b). This trailing wave has larger cross-stream extent, and moves further behind the air-jet as the speed increases (c–d). We call this asymmetric configuration state II. As the towing speed approaches c_{min}, the wave exhibits time-dependent behavior, and begins to stretch out into a "V" shape (e). We call this time-dependent state state III. Finally, above c_{min}, the air-jet creates a steady wave pattern with a wave "cone" that is typical of the wave pattern generated by fast moving objects.

To further elucidate the shape of the wave pattern in states I and II, shadow-

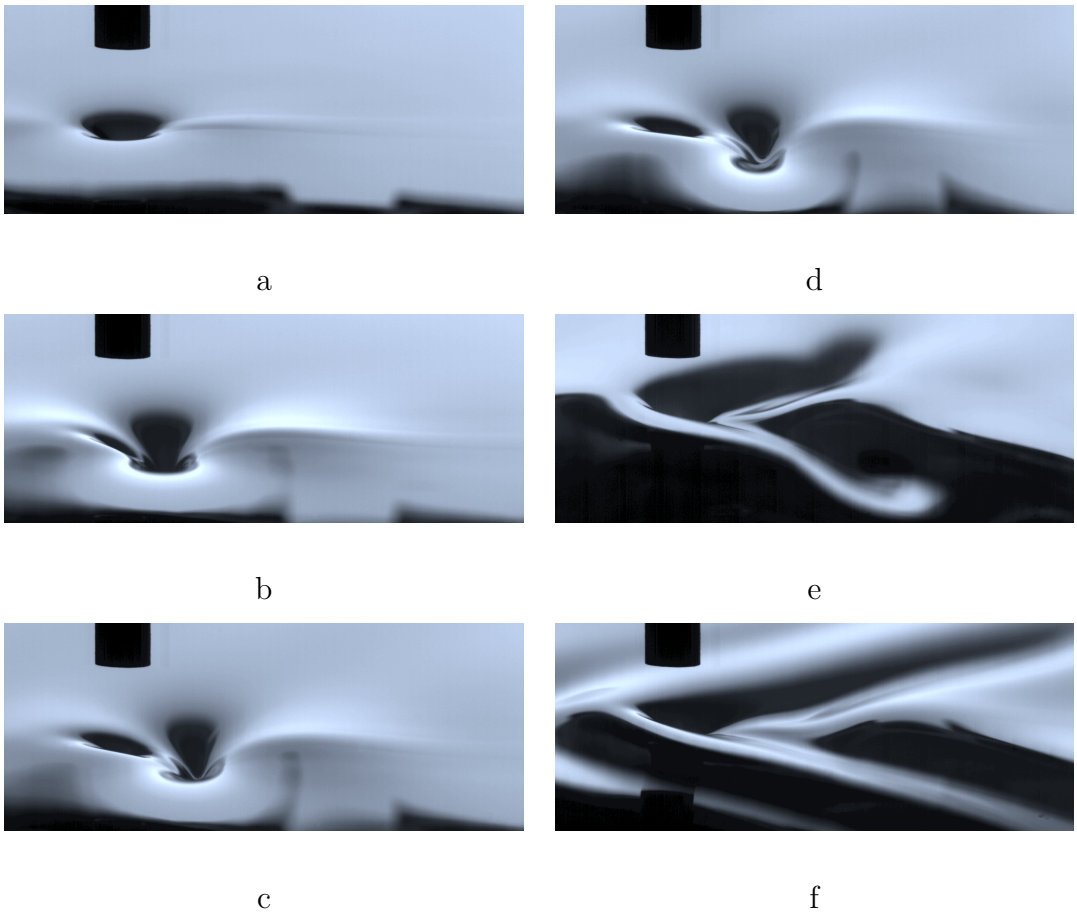

Figure 4.3: Images of the wave pattern taken from above the water surface with the high-speed camera. The forcing parameter is approximately $\epsilon = 0.43$. The pressure forcing (and the pipe) are moving from right to left. (a) $\alpha = 0.905$, (b) $\alpha = 0.927$, (c) $\alpha = 0.948$, (d) $\alpha = 0.970$, (e) $\alpha = 0.981$, (f) $\alpha = 1.03$. The pipe OD is approximately 3.2 mm for scale.

graph images are shown in figure 4.4. In these images, the camera views the wave pattern from slightly below the mean water level, so the top half of the image is merely a reflection across the water surface. In all of these images the air-jet is moving from right to left. Although it is not shown in these cropped images, the pipe is visible in the raw images and a rough pipe position can be determined[3]. The

[3]Here we say "rough" because the camera is focused on the wave pattern, not the pipe. Although they are at nearly the same working distance from the camera lens, the wave pattern is being viewed through water, while the pipe is being viewed through air. This results in a difference in path lengths of the light coming from each object, so while the wave pattern appears in focus, the

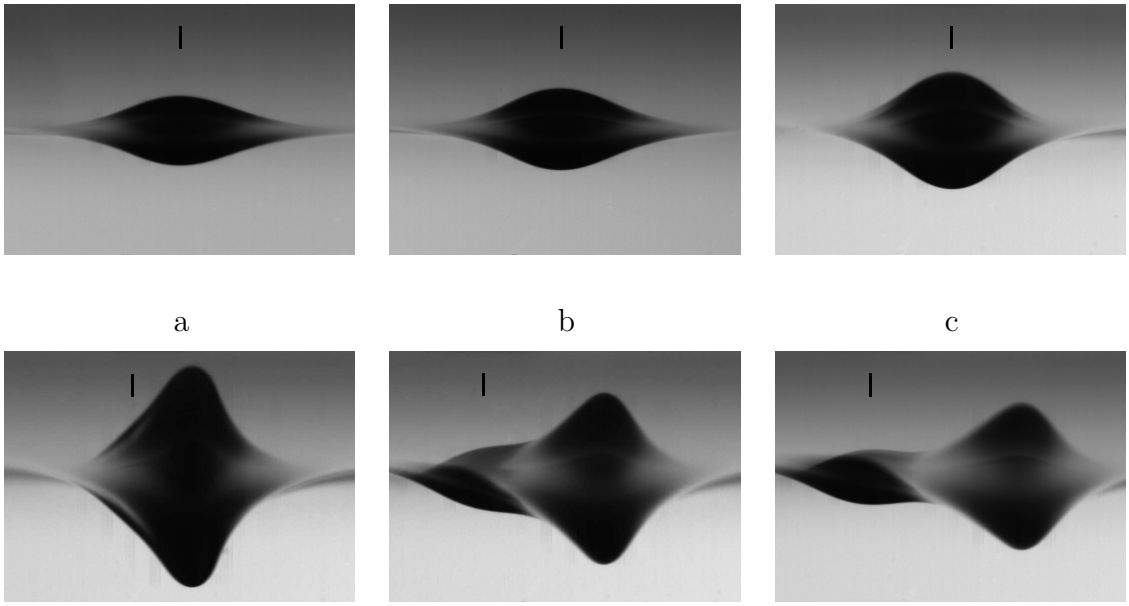

Figure 4.4: Shadowgraph images showing the shape of the wave pattern for several values of the speed parameter α for $\epsilon = 0.43$. The images are taken from slightly below the water surface so the top half of the image is a reflection. In all cases, the air-jet is moving from right to left. The black lines denote the approximate position of the pipe when the photo was taken. Each image is roughly 9.5 by 7 mm in the physical plane. (a) $\alpha = 0.73$, (b) $\alpha = 0.82$, (c) $\alpha = 0.90$, (d) $\alpha = 0.90$, (e) $\alpha = 0.92$, (f) $\alpha = 0.95$. The letters correspond to the points on the curve in figure 4.5.

approximate location of the pipe at the moment the image was taken is denoted by the dark vertical lines in the images. For low α the pattern is in state I with a symmetric shape and the pipe located over the point of maximum depth, as in (a–c). This shape resembles the case when the pipe is stationary and is essentially a linear response. For larger α, the pattern is in state II, with the forcing located ahead of the point of maximum depth, and the formation of a trailing wave, as in (d–f). One can also notice that the depth of this trailing wave decreases and it moves further

pipe appears out of focus, so its precise position is difficult to determine. What we report here is merely based off of visual observation.

behind the pressure forcing as α is increased.

The transition between states I and II is abrupt; a small change in α can yield a dramatically different response. In fact, the two images in figures 4.4(c) and (d) are from experiments with the same value of α, indicating that at some speeds there may even be a kind of bimodal behavior. To investigate this transition, the peak depth of the wave pattern, h_{min}, was measured as a function of the speed parameter α. This peak depth was normalized by h_0 and results are shown in figure 4.5 for $\epsilon = 0.43$. Note that the quantity h_{min}/h_0 is being reported as positive, although these are depression type waves. Each data point in the figure represents a measurement from a separate experimental run. The data in figure 4.5 show that, at low speeds, the depression gradually increases in depth with increasing speed. The noise level in this region, say for $\alpha < 0.85$, is quite low. However, at a certain critical speed α_c, with $\alpha_c \approx 0.9$ for this particular case, there is a discontinuous jump in h_{min}/h_0. Points below this jump (i.e. on the lower curve) are always observed in state I while the points after the jump (i.e. on the upper curve) are observed to be in state II. This is supported by the location of the letters in figure 4.5 which correspond to the conditions for the pictures in figure 4.4. Near the jump, we see more noise in the experimental data, and even the bimodal behavior mentioned above. Take, for example, the six runs with $\alpha \approx 0.9$; four were observed to be in state I, while two were observed to be in state II. This small overlap between the two curves may be due to small errors in carriage speed or air-flow rate rather than some purely bimodal behavior, but it is clear that the response of the system is very sensitive to the experimental conditions in this region of the parameter space. Furthermore,

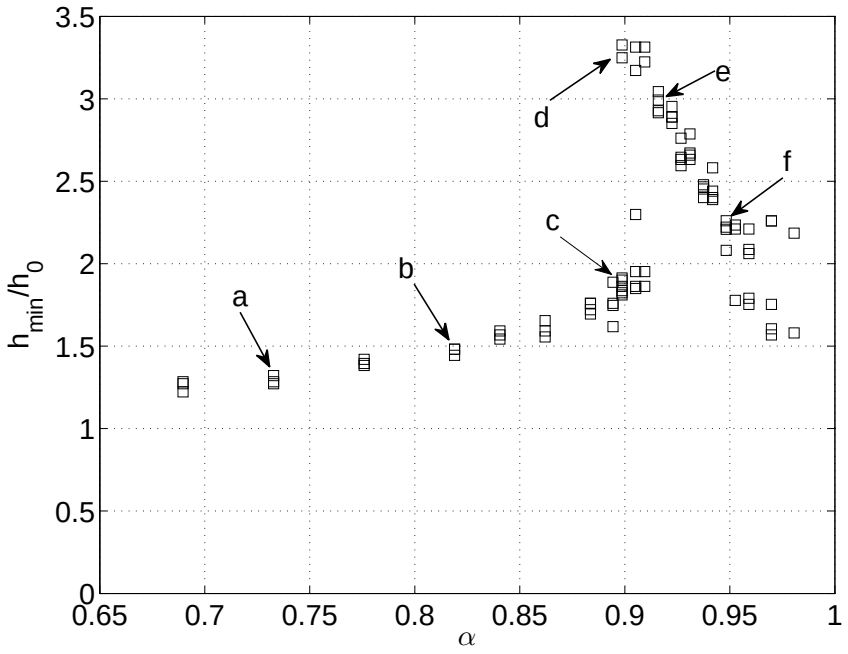

Figure 4.5: Normalized peak depth of the wave pattern, h_{min}/h_0, versus α for $\epsilon = 0.43$. Each data point is taken from a different experiment. The letters correspond to the approximate location of the images in figure 4.4.

near the jump condition, oscillations begin to appear in the wave pattern, another reason for higher experimental noise in this region. This will be discussed more fully in the next section. As a side-note, the shape of the curve in 4.5 seems to resemble the response of a damped, driven, non-linear oscillator near the resonance condition, where the amplitude is observed to jump with small changes in the forcing frequency.

The value of α_c where the transition between states I and II occurs is dependent on the level of forcing. This is shown grahpically in figure 4.6 which shows a plot of h_{min}/λ_{min} versus α for four different values of ϵ. Here the choice of the minimum gravity-capillary wavelength $\lambda_c = 2\pi(\tau/g\rho)^{1/2}$ as the non-dimensionalizing paramter is useful as the data curves collapse in state II (note that if we had instead chosen h_0

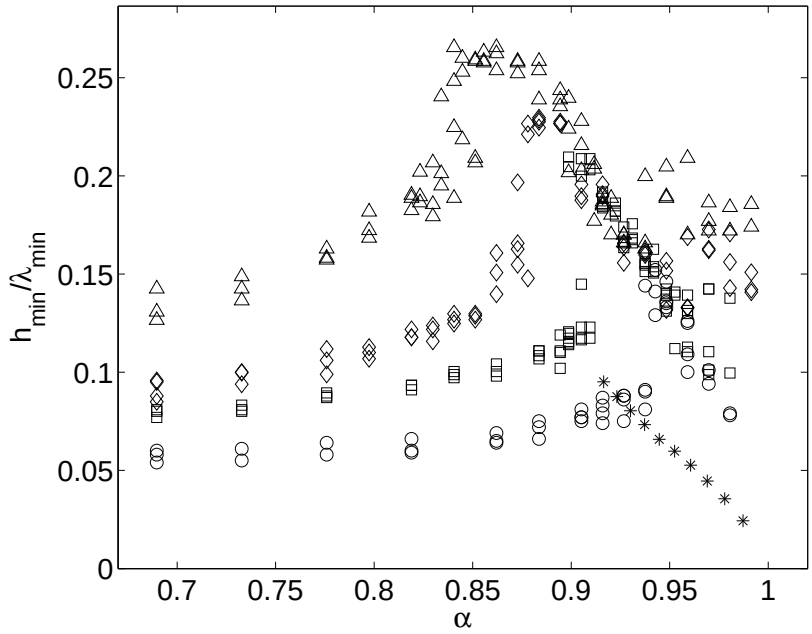

Figure 4.6: Normalized peak depth of the wave pattern h_{min}/λ_{min} versus the speed parameter α. Four different values of ϵ are shown. $\circ$ $\epsilon = 0.30$, $\square$ $\epsilon = 0.43$, $\diamond$ $\epsilon = 0.51$, $\triangle$ $\epsilon = 0.69$. Note that all the data fall on a common line in state II, independent of the level of forcing. Points above this curve at high values of α represent conditions where the pattern is in state III, see text. The points with the $*$ are the approximate values from the inviscid, freely propogating lump solutions calculated by [27], their figure 6.

as the length scale the curves would not collapse in this region since h_0 is different for each case). Because λ_{min} is the same for each case, the universal behavior of the curves indicates that in state II there is a one-to-one relationship between wave depth and phase speed, a behavior that is typical in the theory and calculations of gravity-capillary solitary waves. For example, also shown in figure 4.6 are approximate data from [27] for steady numerical calculations of freely propogating lumps (their figure 6). As can be seen in the figure, the numerical calculations of [27] do not match the curve for state II, although they do appear to roughly intersect the state I-state II transition point for the two lowest forcings ($\epsilon = 0.30$ and $\epsilon = 0.43$). For high levels

of forcing and high towing speeds, the data appear to move away from this universal curve, showing a different kind of behavior; see for example the points for $\epsilon = 0.69$ and $\alpha > 0.90$ in figure 4.6. As will be seen, the behavior of the wave pattern in this region is due to a transition to the time-dependent state III and will be analysed in the next section. It is clear from figure 4.6 that the value of α_c decreases as ϵ increases, indicating that nonlinear effects are important over a broader range of speeds when the forcing is higher. Figure 4.6 also shows the transition region appears to broaden with increased forcing, so that the jump is less abrupt.

4.4.2 Time-dependent behavior

As was described in the previous section, at low α a stable, symmetric state I response is observed while for higher α a stable, asymmetric state II reponse is seen. In between, there is a transition between the two states. This transition is very abrupt for low ϵ but becomes more gradual at higher ϵ. However, as is shown below, regardless of the value of ϵ, a clear time-dependent behavior is observed near the transition point. Similarly, for high values of α and ϵ, time-dependent motions are also observed although these motions are of a different character and are therefore referred to seperately as state III.

4.4.2.1 Transition to state II

To measure the time-dependence near the transition from state I to state II, the camera was mounted to the carriage to take shadowgraph movies in a frame

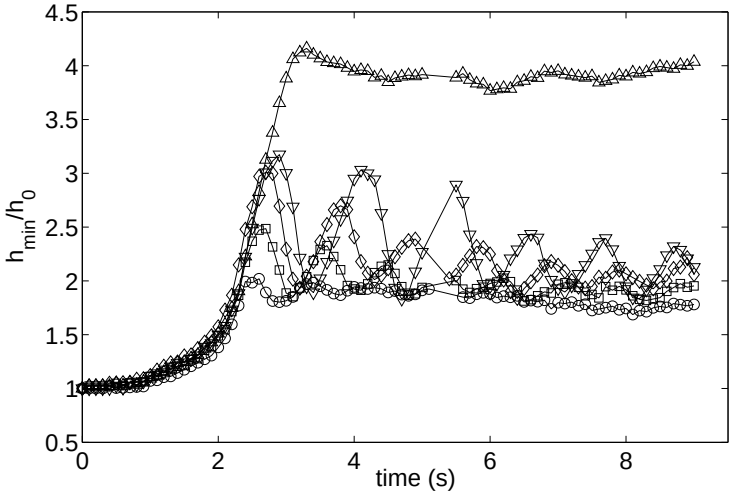

Figure 4.7: Plot of the normalized peak depth of the wave pattern h_{min}/h_0 as a function of time for $\epsilon = 0.43$ and various values of α. $\circ$ $\alpha = 0.88$, $\square$ $\alpha = 0.89$, $\diamond$ $\alpha = 0.905$, $\triangledown$ $\alpha = 0.907$, $\triangle$ $\alpha = 0.909$.

of reference moving with the pipe. This allows the time-dependent behavior of the pattern to be recorded as the pressure forcing moves down the tank. The camera was triggered with the start of the carriage motion so the intial startup could also be captured. The results are presented in figure 4.7 which show the normalized peak depth of the wave pattern h_{min}/h_0 as a function of time for $\epsilon = 0.43$ and several values of α near α_c. The camera passes in front of a column of the tank half-way through the carriage motion (from about 5–5.5 seconds), so there is a small gap in the curves. It should be noted that for the shadowgraph measurements presented in the previous section, the camera (which was stationary) was positioned about 30 cm beyond this column, so the moving camera passes the original shadowgraph location at around $t = 7$ seconds. For low values of α, the pattern appears to be stable in the lower state I, and the wave resembles the pictures shown in figure 4.4(a–c). As the towing speed is increased, the maximum depth shows oscillations in the vertical (z)

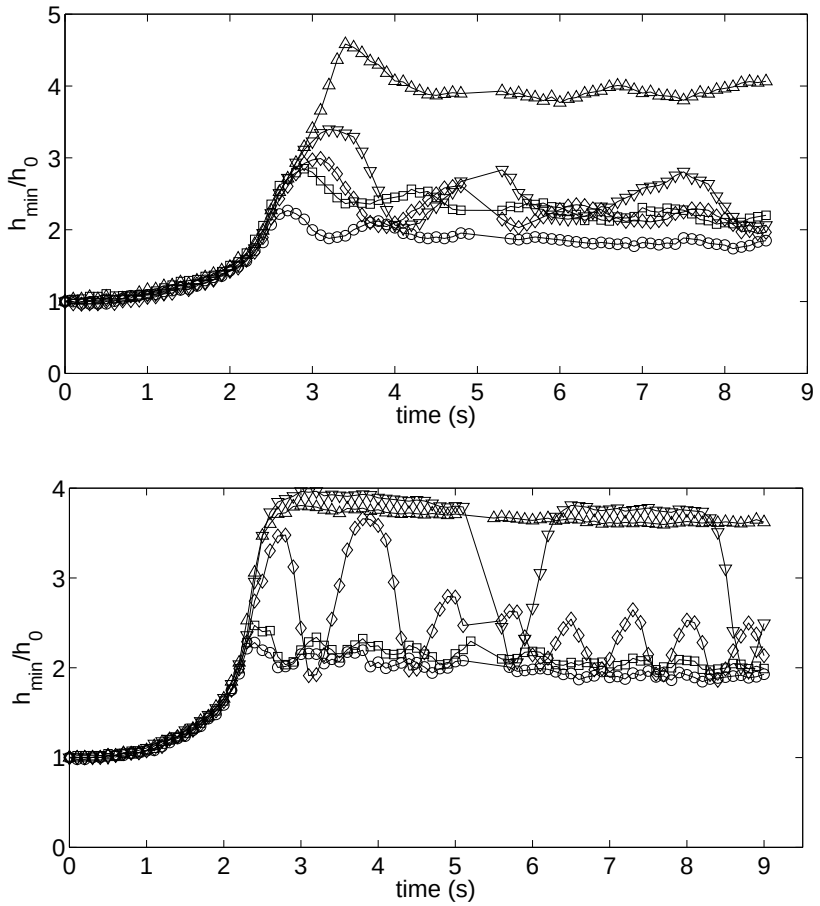

Figure 4.8: Plot of the normalized peak depth of the wave pattern h_{min}/h_0 as a function of time for $\epsilon = 0.30$ (upper plot) and $\epsilon = 0.51$ (lower plot) for various values of α. Upper plot: $\circ$ $\alpha = 0.927$, $\square$ $\alpha = 0.938$, $\diamond$ $\alpha = 0.940$, $\triangledown$ $\alpha = 0.9440$, $\triangle$ $\alpha = 0.9444$. Lower plot: $\circ$ $\alpha = 0.856$, $\square$ $\alpha = 0.862$, $\diamond$ $\alpha = 0.873$, $\triangledown$ $\alpha = 0.884$, $\triangle$ $\alpha = 0.888$.

direction. Both the amplitude and the period of these oscillations appear to increase with increasing towing velocity. Finally, after only a small additional change in α ($\Delta\alpha = 0.002$ or about 0.05 cm/s), the pattern jumps into the higher state II, where it appears to be relatively stable again, and the wave resembles the photograph shown in figure 4.4(d).

The range over which these oscillations occur and their amplitude are also

affected by the level of forcing. This is presented graphically in figure 4.8, which shows the normalized height as a function of time for $\epsilon = 0.30$ (upper plot) and $\epsilon = 0.51$ (lower plot), for several values of α near α_c (time-dependent data for $\epsilon = 0.69$ were not recorded). In both of these cases we see similar behavior: a stable state I h_{min} at low speeds, oscillations that increase in both amplitude and period as α is increased, and finally a "jump" to state II. For $\epsilon = 0.30$ this jump is very sudden; the difference in speed between the highest two curves in the upper plot is only 0.01 cm/s. For $\epsilon = 0.51$, the jump region is broader; for example the difference in speed between $\alpha = 0.873$ (diamonds) and $\alpha = 0.884$ (down triangles) is 0.25 cm/s. Although, even for $\alpha = 0.884$, the wave pattern was even observed to be stable in state II, briefly transition to state I, then back to state II (see figure 4.8 lower plot), so there still appears to be some instability even for a larger difference in towing speed.

The oscillations in figures 4.7 and 4.8 appear to decay as the wave propagates, indicating that they may be transient. The period of the oscillations are very large (~ 1 s) in comparison to a capillary-gravity time scale ($\sim (\tau/\rho g^3)^{1/4} \approx 0.017s$), and persist even though the wave pattern has traveled many wavelengths at a constant speed (1 second of time is roughly 100 tube diameters). To investigate whether the oscillations eventually decay to zero, the shadowgraph setup was moved to allow movies to be recorded further down the tank from where the motion starts. Due to lighting limitations, this setup could not capture the entire motion in a single run. Figure 4.9 shows h_{min}/h_0 versus time for $\epsilon = 0.43$ and $\alpha = 0.905$, with the data from the extended run plotted along with the original data from figure 4.7 for

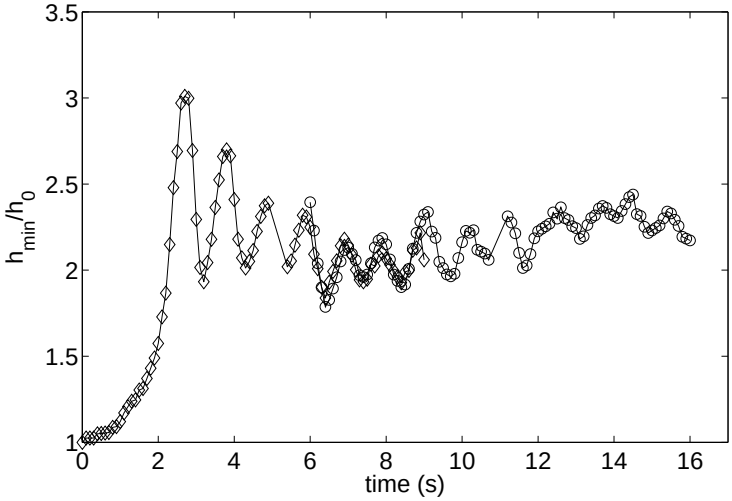

Figure 4.9: Plot of the normalized peak depth of the wave pattern h_{min}/h_0 as a function of time for $\epsilon = 0.43$ and $\alpha = 0.905$. $\diamond$ are the original data and $\circ$ are the data from the extended run.

comparison. The camera passes in front of another tank column between roughly 10 and 11 seconds so there is another gap in the data. The figure shows that while the amplitude of the oscillations does decrease, it does not appear to reach zero, at least over the range measured. Furthermore, at late times, the oscillation period does not appear to be as regular as it was near the startup. Unfortunately the length of this data set reaches the physical limitations of our experimental facility, so whether or not the wave pattern settles to a steady state near α_c, given enough time, is still an open question.

4.4.2.2 State III behavior

After passing through the region of unsteady behavior below α_c, the wave pattern becomes steady again in state II, and the wave shape resembles that in figure 4.4(f) with two peaks, one located under the forcing, and the larger depression lag-

ging the forcing. As is shown in figure 4.6, as the towing speed is increased further, the amplitude of this trailing depression decreases. As the amplitude of the following wave decreases, the amplitude of the leading wave actually *increases*, eventually becoming larger than the following wave if the towing speed is high enough. Eventually, for high levels of forcing and high towing speeds, the relationship between the amplitude and phase speed of the wave departs from the universal behavior noted in figure 4.6 (see for example the points with $\epsilon \geq 0.40$ and for $\alpha > 0.905$) and the wave pattern begins to exhibit a time-dependent behavior. The oscillations of the wave in this upper region are characterisitcally different from the oscillations observed between state I and state II. The wave motion does not appear to be strictly periodic, but it does have a rather well defined "cycle" with the "shedding" of solitary depressions from the tips of a "V"-shaped pattern. Figure 4.10 shows images of the water surface as the wave passes through one of these cycles. In this image sequence, the camera was mounted to the carriage and moved with the pipe. Initially the wave has a "V" shape as shown in figure 4.10(a). The pattern then stretches out as two disturbances are shed from the tips of the "V" (b–c) producing a more localized, linear response (d). The nonlinear response quickly grows again and the "V" shaped pattern is observed once more (e–f). The temporal spacing between each image is 0.36 seconds. These images have been found to match quite well with the numerical calculations of Akylas *et al.* based on the simple model equation discussed in section 4.2, [101].

This same shedding cycle is shown in figure 4.11 which presents a sequence of shadowgraph images of the pattern taken from below the water surface. For

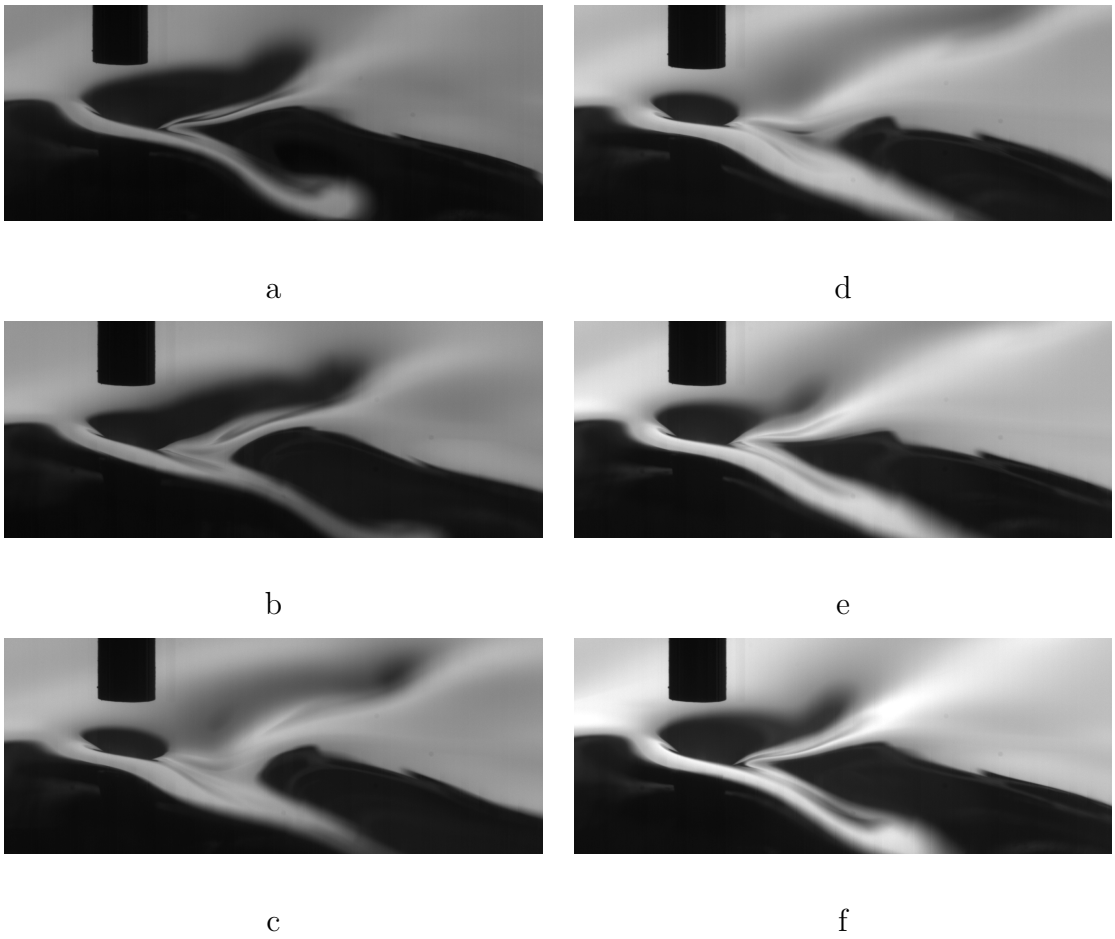

Figure 4.10: Sequence of images showing the "shedding" oscillation of the wave pattern in state III from above the water surface for $\epsilon = 0.43$ and $\alpha = 0.981$. The images are separated by 0.36 s in time. (a) The pattern begins as a "V" shape. (b–c) The pattern stretches out as two small disturbances are shed backwards from the tips of the "V". (d) The response momentarily resembles a localized, linear response. (e–f) The nonlinear response quickly grows and the "V"-shaped pattern is observed once more.

these images, the camera was also mounted to the carriage and moved with the pipe. The parameters are $\epsilon = 0.51$ and $\alpha = 0.958$; note that these are different than the parameters for the images in figure 4.10. The temporal spacing between each image in figure 4.11 is 0.2 seconds. The pattern begins with a small trailing wave pattern 4.11(a), and the dip under the pressure forcing grows (b). As the

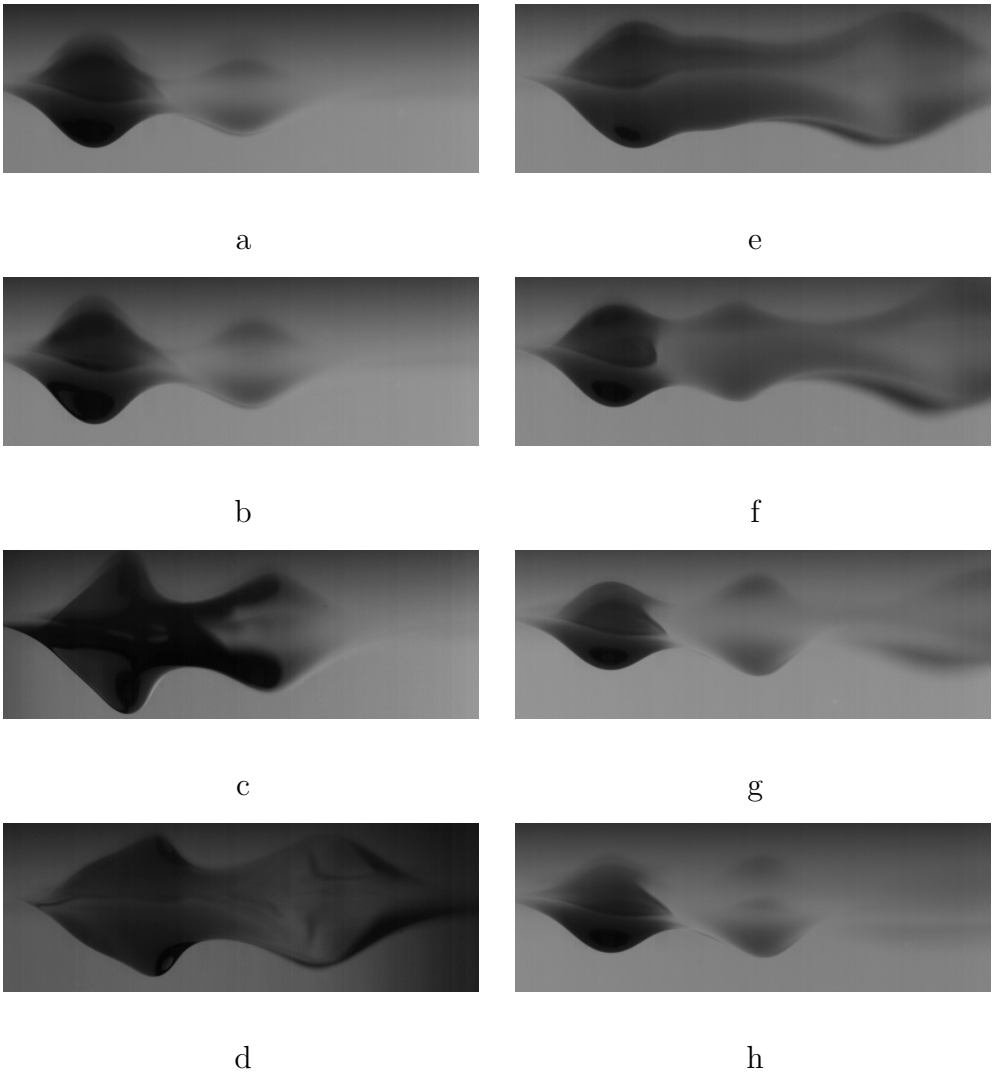

Figure 4.11: Sequential shadowgraph images taken from below the water surface showing the oscillation of the wave pattern for $\epsilon = 0.51$ and $\alpha = 0.958$. The spacing between each image is 0.2 seconds. (a) The wave begins with a trailing depression. (b) The amplitude of the peak under the forcing grows. (c) As the peak grows it moves backwards (moving slower than the forcing) (d) As the main peak moves back further, the trailing wave grows in amplitude, and is eventually "shed" in (e). (f) A new trailing peak is formed and the pattern begins to retake its original shape (g) and (h).

amplitude increases, the phase speed decreases and the peak begins to move behind the pressure forcing (c) and the amplitude of the following wave increases as well (d). As this "peak" continues to move back, the trailing wave is "shed" (e), and is

eventually replaced by the backwards propogating peak (f). The wave then returns to a shape similar to its original configuration (g–h). As the images in figures 4.10–4.11 show, as the speed approaches c_{min} a highly time-dependent, highly-3D pattern develops, although this pattern does not appear to have a very regular period. For speeds even closer to c_{min} the various shapes of the wave do not necessarily resemble those in figure 4.11 as the wave pattern becomes highly extended behind the forcing and the ability of the shadowgraph technique to understand the wave shape (i.e. a 2D projection of a 3D pattern) becomes rather limited. Preliminary results of the work by Akylas and colleagues (personal communication) have shown that the time dependent behavior at high towing speeds may be the result of secondary and tertiary "resonances", with multiple solutions at a given value of α.

4.4.3 Three-dimensional shape

In addition to the changes in the streamwise shape of the pattern, the cross-stream shape is also affected by the towing speed. Variation in the cross-stream shape was measured using the LIF technique. By measuring a series of 2D profiles in the $x-z$ plane, and with the pipe at various y locations, it is possible to combine these profiles together to form a surface $z(x, y)$. It is important to note that while this method accurately measured the majority of the wave pattern, it was rather poor at resolving the details of the depression directly beneath the pipe. This is because the highly curved surface under the pipe caused large refraction patterns and line-of-sight blockage in the image that made accurate measurement somewhat

unreliable. Furthermore, the small size of the pipe, the finite width of the laser sheet and the finite spacing between the y locations all compounded to make the actual surface under the pipe almost undetectable with the LIF method. For example, the width of the light sheet (≈ 1 mm) and the spacing between consecutive y locations (2.5 mm) are nearly the same as the diameter of the pipe, so any features that have a width on the order of the pipe diameter will only appear in a single $z(x)$ profile. So, while two distinct peaks can be seen in shadowgraph images shown in figure 4.4(f), one beneath the pipe and one trailing it, only the latter, which is much wider in the cross-stream direction, is resolved using the LIF technique.

Figure 4.12 shows a typical set of results obtained using the LIF method. The figure shows a surface plot, $z(x, y)$, with underlying contours, of the wave pattern at $\epsilon = 0.43$ and $\alpha = 0.95$. In the figure the pipe motion is in the negative x direction. Lines in the $x - z$ plane are obtained by tracking the location of the free surface at one horizontal location in a single movie, and each line was obtained from a different movie with the pipe placed at a different y position. The figure is exaggerated by a factor of 10 in the vertical (z) direction. One conclusion that can be made from this surface plot is that even though each $z(x)$ slice was obtained from a different run, the data appear to line up in the y (cross-stream) direction very well, indicating that the pattern is both steady and repeatable. The surface shows a very clear 3D pattern that is highly localized in all directions, elongated in the cross-stream relative to the streamwise, and very clearly resembles the gravity-capillary lump solutions computed by previous authors; see for example figure 4.1. The asymmetry between the streamwise and cross-stream directions is shown more clearly in figure

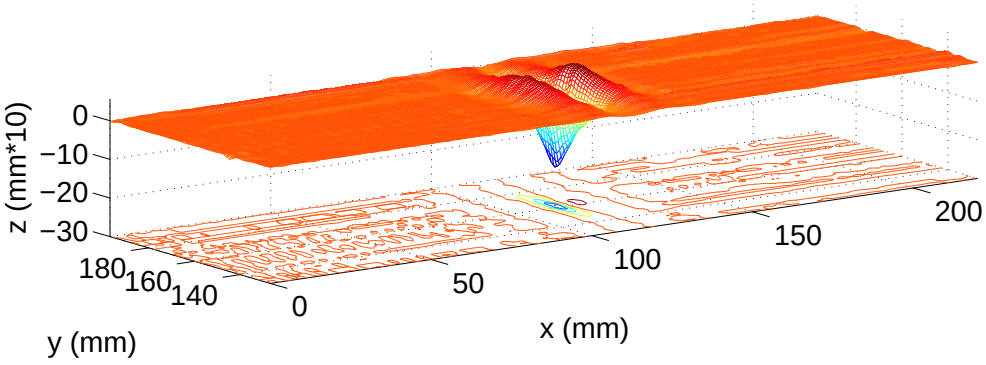

Figure 4.12: A typical surface plot obtained using the LIF method with $\epsilon = 0.43$ and $\alpha = 0.95$. The data are obtained by tracking the height of a single point in a movie as the wave passes by. Each line in the $x - z$ plane is obtained from a different run with the pipe at a different y location. The x and y axes are scaled the same, but the vertical scale is exaggerated by a factor of 10. The smooth variation of the pattern in the y direction is indicative of the repeatability and steadiness of the wave pattern.

4.13 which contains plots of the streamwise and cross-stream profiles at the center of the wave pattern. The streamwise profile also shows a slight asymmetry, with the elevation of the leading edge (to the left) smaller than the trailing edge. This is somewhat in contrast with the results of [121] who found the leading edge to be larger in their numerical calculations of a pressure source moving near c_{min}. Closer analysis of the streamwise profile in figure 4.13 also shows that the trough is not symmetric either; the downstream edge appears to have a slight change in curvature near $x \approx -3$ mm. As the shadowgraph data showed, this is most likely the location of the leading depression that is located beneath the pipe, but is unable to be resolved accurately with the LIF method.

Figure 4.14 shows the dependence of the 3D behavior of the wave pattern on the translation speed for a constant value of the forcing parameter ϵ. The figure

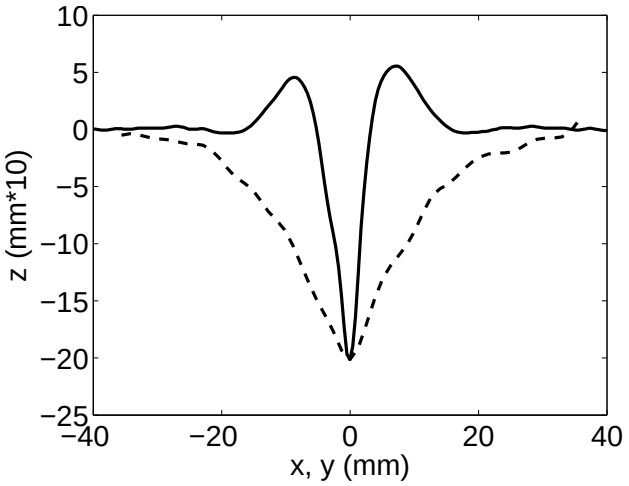

Figure 4.13: Streamwise (solid) and cross-stream (dashed) profiles at the center of the surface pattern shown in figure 4.12.

shows a top view ($x - y$ plane) of the wave pattern with $\epsilon = 0.43$ but with three different values of the speed parameter α. All three plots are colored on the same vertical scale so direct comparisons can be made. The pattern appears to change only slightly between $\alpha = 0.86$ and $\alpha = 0.90$ (a–b), with a marginal increase in depth and cross-stream extent; these are state I responses. However, between $\alpha = 0.90$ and $\alpha = 0.95$ (b–c), we see a marked increase both in the depth and the cross-stream size of the wave pattern, all while remaining highly localized; this is a state II response. The clear 3D character of the wave pattern in state II, coupled with the distinct nonlinear response of the wave amplitude above α_c leads us to believe that the wave pattern trailing the pressure forcing in state II is a gravity-capillary lump that is being excited by the motion of the pressure forcing.

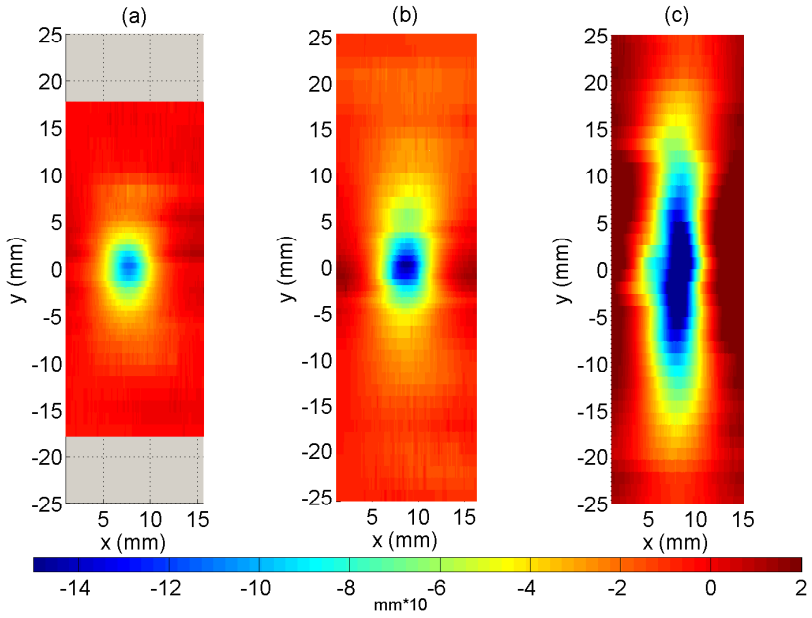

Figure 4.14: Top view (x-y plane) of the reconstructed wave pattern for $\epsilon = 0.43$ and at three different values of α. (a) $\alpha = 0.86$, (b) $\alpha = 0.90$, (c) $\alpha = 0.95$.

4.5 Summary and conclusions

The results presented here have shown that a pressure source moving over a free liquid surface at speeds below the linear minimum phase speed creates a wave pattern that is locally confined in 3D. These solitary waves, commonly referred to as lumps, are elongated in the cross-stream direction relative to the streamwise direction, and have a phase speed that is related to the wave depth. For a given forcing, the maximum wave depth h_{min} increases slightly with increasing speed, until at a certain critical speed, where h_{min} "jumps" and the wave pattern looks qualitatively different. After this jump, h_{min} appears insensitive to the level of forcing and shows a one-to-one relationship with the phase speed. The point of maximum depth, while initially located directly beneath the forcing, begins to trail the forcing

beyond this jump condition. In the region near, but below the jump condition, oscillations appear in the wave pattern. Both the period and the amplitude of these oscillations increase as the wave speed is increased, and the range of speeds over which these oscillations occur depends on the level of applied forcing. Time-dependent behavior is also observed at high towing speeds, given a large enough forcing. This time-dependent behavior may be related to the existence of secondary and tertiary "resonances" observed in some numerical solutions. The results of this work comprise the first experimental investigations of the three-dimensional nature and time-dependent behavior of gravity-capillary solitary waves on deep water, and help to elucidate the physics of solitary waves in nonlinear dispersive media.

Chapter 5

Summary of contributions and future work

This thesis presented some experimental investigations of capillary effects on free-surface waves. In particular, our goal was to understand some of the complicated surface phenomena that result from nonlinear effects such as wave breaking and the formation of gravity-capillary solitary waves. While the current work was directed in these specific areas, the results have some broader implications in fluid mechanics as well as in other areas such as physical oceanography and nonlinear wave theory. As waves steepen, driven either by direct wind forcing or nonlinear interactions, capillary effects can become important near the wave crest just prior to breaking. Although it was previously held that the crest shape at breaking was independent of the breaker wavelength, the current results are to the contrary. Several measurements of the crest shape showed significant change in our experiments, a result most likely attributed to the fact that the current work covered a larger range of wavelengths than previously reported. This change in crest shape is important because it implies a coupling between the small scales, which are dominated by surface tension, and the larger scales, which are dominated by gravity, so attempts to understand the dynamics at small scales independently may be misguided. It was also found that plotting the various crest measurements versus a certain measure of the wave slope revealed a monotonic behavior that is independent of the method

used to generate the wave. This indicates that the wave dynamics near breaking are unaffected by the wind. This result is particularly useful because it leaves open the possibility for studying the small surface features produced by breaking, such as ripples, drops and bubbles, without the need to recreate wind conditions experimentally or numerically. Interestingly, although the dimensional shape changes with the dynamics of the gravity wave, the non-dimensional crest shape remains remarkably self-similar over a large range of wavelengths and breaker types. Finally, the slope of the wave at breaking, and hence the shape of the crest, was found to be a function of the wave growth rate and phase speed, a result which contributes to our understanding of a universal breaking criterion. Although this result was determined for individual waves, it seems plausible that it is related to the breaking criterion put forth by [64] who used the growth rate of the energy at the peak of the modulating wave packet as a means of determining breaking. How these two results are related is an area for future investigation.

Once breaking begins, the flow quickly transitions from an essentially 2D irrotational flow to a 3D turbulent flow that produces an assortment of surface ripples in the breaking zone. The experiments presented here represent some of the first investigations into the three-dimensional nature of the surface ripples generated by unsteady spilling breakers. The results show very clearly the presence of periodic streamwise ripples generated at the leading edge of the breaker, an observation in agreement with previous experiments. An entirely new result is that the period of these ripples appears to be related to the generation of three-dimensional surface motions, as evidenced by the large variation in the cross-stream ripple ampli-

tude. Moreover, this flurry of cross-stream activity coincides with the troughs of the streamwise ripples, as opposed to their crests as was previously believed. Both the streamwise and cross-stream ripples do not Froude scale, further substantiating the idea that these motions are controlled by turbulent length scales and surface tension. The typical cross-stream ripple amplitude was found to have a cubic dependence on the breaker wavelength, a result that may serve well in obtaining estimates of small-scale fluctuations from observations of breaker phase speeds or wavelengths in the field. Measurements of 1D cross-stream surface gradients showed the existence of thin and persistent "scar"-like regions in the breaking zone. These features appear to be produced in the troughs of the streamwise ripples, and may be the result of low or high-speed "streaks" that have been observed near the crest of steep waves. We use these results to speculate a possible model for the distribution of vorticity in the early stages of breaking. Measurements or numerical calculations of the time-dependent flow velocity in this region would certainly sharpen our understanding of the sub-surface turbulence and its role in the production of 3D ripples.

Finally, the nonlinear wave pattern generated by a moving pressure source was also investigated. Water waves by nature are dispersive and feature a minimum phase speed at finite wavenumber. Local extrema of the phase speed are known bifurcation points between linear wave trains and solitary-wave type solutions. Morever, if this extrema happens to be a minimum, 3D solitary wave solutions may be expected. In this thesis it was shown that a moving pressure source can produce a stationary 3D wave pattern that travels at speeds below the minimum phase speed. An entirely novel result is that the wave pattern undergoes a series of

transitions that result in a dramatic change of the wave state. At speeds far below the linear minimum no waves are produced, and the pattern resembles the stationary case. However, at a certain speed there is an abrupt transition to a wave-like state with an asymmetric pattern that forms behind the pressure forcing. This wave is elongated in the cross-stream direction and is qualitatively in agreement with recent numerical calculations. It was also shown that in this state the maximum depth of the wave has a one-to-one relationship with the phase speed, a common feature of solitary wave behavior. The boundary between these first two states appears to be unstable, with the appearance of periodic oscillations in the wave pattern. At even higher speeds, but still below the minimum, there is a second transition to a time-dependent state that features the shedding of solitary depressions from the tips of a "V"-shaped pattern. The abrupt transitions between these various states are somewhat analogous to resonances in forced non-linear oscillators, although the possibility that several such "resonances" might exist is intriguing. Although this work pertains to waves on water surfaces, the results generalize to other areas of physics with dispersive wave systems and phase speed minima, such as the generation of rotons in superfluid helium or waves in plasmas.

Appendix A

Wave growth rate

To illustrate the choice of the average growth rate, P, consider the wave crest height versus time data for focused breakers plotted in figure A.1. In this plot, the crest height, $z(t)$, is nondimensionalized by its maximum value for each wave, and the time t is nondimensionalized by the average wave frequency ($t\bar{f}$) with $t = 0$ the time of incipient breaking. Data are shown for the seven dispersively focused waves. As can be seen from the plot, the instantaneous rate of change of dimensionless crest height is nearly zero at incipient breaking for all the waves. However, the wide range of changes in height over the time period from say $t\bar{f} = -0.2$ to $t\bar{f} = 0$ for the various waves indicates a wide range in average rate of growth. The data in figure A.1 are consistent with a wave crest traveling through a wave packet envelope and breaking when the wave reaches the position of the maximum height of the envelope. The crest height data for the side-band waves and some of the wind waves show similarly shaped curves.

Values of P could not be computed for five of the wind waves. The problem in computing P for these waves stems from the fact that wind waves break at random times and locations and that they interact with other wave components during breaking. Because they occur randomly, it is difficult to get a full movie of the breaking event; see description of procedure for obtaining movies of these waves

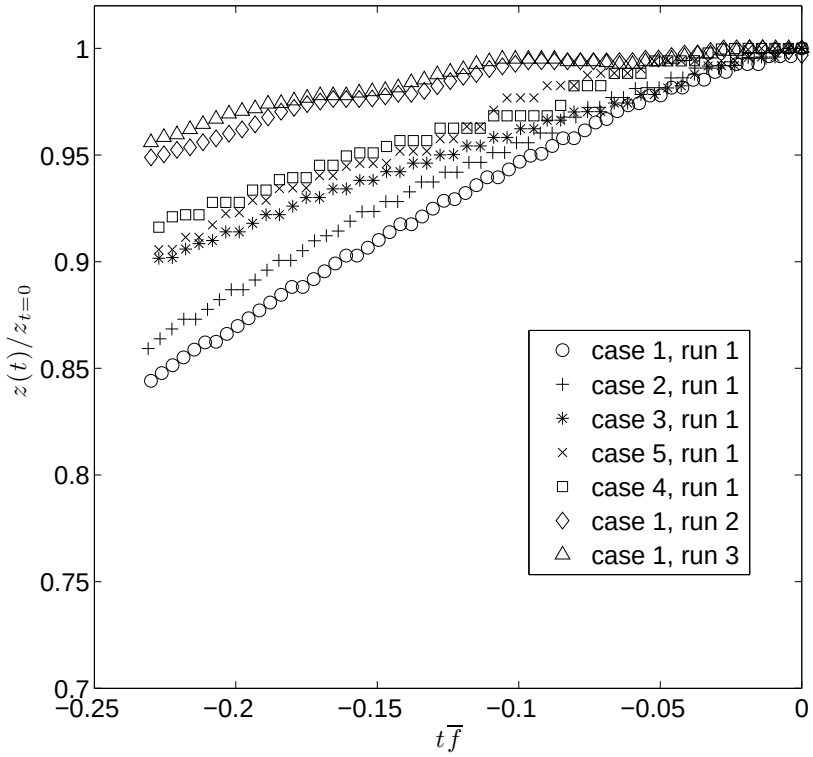

Figure A.1: Non-dimensional height ($z(t)/z_{t=0}$) versus non-dimensional time ($t\bar{f}$) for the dispersively focused breakers. Here $z(t)$ is the wave height at any time t with $t = 0$ the time of incipient breaking, $z_{t=0}$ is the wave height at incipient breaking and $\bar{f}$ is the average frequency of the wave packet.

at the end of section 2.3.3 . Thus, in some of the waves there was no photographic record of the breaking event for the required 0.23 wave periods prior to incipient breaking. The interaction of the breaker with other wave components is seen in the movies as the pre-breaking crest moves over small slow-moving wave components. Sometimes the breaking event is triggered by this interaction. While the crest shape data at the incipient condition was included in the geometry parameter plots for these breaking events, a growth rate could not be obtained since these waves can break even when the crest height has been constant or decreasing up to the

point where the long wave interacts with the short wave. Our relationship between c_p/c_{min}, P/c_p and m is not valid for these waves since the breaking mechanism does not involve a continuous increase in amplitude leading up to incipient breaking. It is interesting that, even for these breaking events, the geometrical parameters describing their crest shape fall on the same curve when plotted versus m as the data from the other waves.

Bibliography

[1] JH Duncan, H Qiao, V Philomin, and A Wenz. Gentle spilling breakers: crest profile evolution. *Journal of Fluid Mechanics*, 379:191–222, 1999.

[2] KM Berger and PA Milewski. The generation and evolution of lump solitary waves in surface-tension-dominated flows. *Journal of Applied Mathematics*, 61(3):731–750, OCT 25 2000.

[3] ADD Craik. The origins of water wave theory. *Annual Review of Fluid Mechanics*, 36:1–28, 2004.

[4] ADD Craik. George Gabriel Stokes on Water Wave Theory. *Annual Review of Fluid Mechanics*, 37:23–42, 2005.

[5] F White. *Viscous Fluid Flow*. McGraw-Hill, 1991.

[6] RS Hansen and J Ahmad. Waves at interfaces. In DA Cadenhead, editor, *Progress in Surface and Membrane Science*. Academic Press, 1981.

[7] GG Stokes. On the theory of oscillatory waves. *Transactions of the Cambridge Philosophical Society*, 8:441, 1847.

[8] JV Wehausen and EV Laitone. Surface waves. In *Encycolpedia of Physics*, volume IX, pages 446–778. Springer Verlag, 1960.

[9] ML Longuet-Higgins and M Tanaka. On the crest instabilities of steep surface waves. *Journal of Fluid Mechanics*, 336:51–68, 1997.

[10] O. M. Phillips. On the generation of waves by turbulent wind. *Journal of Fluid Mechanics Digital Archive*, 2(05):417–445, 1957.

[11] JW Miles. On the generation of surface waves by shear flows. part 4. *Journal of Fluid Mechanics*, 13:433–448, 1962.

[12] OM Phillips. On the dynamics of unsteady gravity waves of finite amplitude 1: The elementary interactions. *J. Fluid Mech.*, 9:193–217, 1960.

[13] OM Phillips. On the dynamics of unsteady gravity waves of finite amplitude 2: Local properties of a random wave field. *J. Fluid Mech.*, 11:143–155, 1961.

[14] TB Benjamin and JE Feir. Disintigraion of wave trains on deep water 1: Theory. *Journal of Fluid Mechanics*, 27:417–430, 1967.

[15] TD Benjamin. Instability of periodic wavetrains in nonlinear dispersive systems. *Proc. Roy. Soc. London Ser. A*, A299, 1967.

[16] BM Lake, HC Yuen, H Rungaldier, and WE Ferguson. Nonlinear deep-water waves - theory and experiment 2: Evolution of a continuous wave train. *Journal of Fluid Mechanics*, 83:49–74, 1977.

[17] MJ Lighthill. Some special cases treated by Whitam theory. *Proceedings of the Royal Society of London Series A - mathematical and physical sciences*, 299:28–53, 1967.

[18] WK Melville. The instability and breaking of deep-water waves. *Journal of Fluid Mechanics*, 115:165–185, 1982.

[19] WK Melville. Wave modulation and breakdown. *Journal of Fluid Mechanics*, 128:489–506, 1983.

[20] MY Su. 3-dimensional deep-water waves 1: Experimental-measurement of skew and symmetric wave patterns. *Journal of Fluid Mechanics*, 124:73–108, 1982.

[21] MY Su, M Bergin, P Marler, and R Myrick. Experiments on non-linear instabilities and evolution of steep gravity-wave trains. *Journal of Fluid Mechanics*, 124:45–72, 1982.

[22] Y Yao, P Wang, and MP Tulin. Surface tension effects on breaking waves - longtank simulation. Technical report, University of California, Santa Barbera, 1996.

[23] MS Longuet-Higgins. Capillary rollers and bores. *Journal of Fluid Mechanics*, 240:659–679, 1992.

[24] MS Longuet-Higgins. Capillary-gravity waves of solitary type on deep water. *Journal of Fluid Mechanics*, 200:451–470, 1989.

[25] MS Longuet-Higgins. Capillary-gravity waves of solitary type and envelope solitons on deep water. *Journal of Fluid Mechanics*, 252:703–711, 1993.

[26] TR Akylas. Envelope solitons with stationary crests. *Physics of Fluids A*, 5(4):789–791, APR 1993.

[27] EI Părău, JM Vanden-Broeck, and MJ Cooker. Nonlinear three-dimensional gravity-capillary solitary waves. *Journal of Fluid Mechanics*, 536:99–105, 2005a.

[28] B Kim and TR Akylas. On gravity-capillary lumps. *Journal of Fluid Mechanics*, 540:337–351, 2005.

[29] J Wu, J Wheatley, S Putterman, and I Rudnick. Observation of envelope solitons in solids. *Physical Review Letters*, 59, 1987.

[30] A Scott. *Nonlinear Science: Emergence and Dynamics of Coherent Structures.* Oxford University Press, 1999.

[31] A Hasegawa and M Matsumoto. *Optical Solitons in Fibers.* Springer, 2003.

[32] JH Duncan, V Philomin, M Behres, and J Kimmel. The formation of spilling breaking water waves. *Physics of Fluids*, 6(8):2558–2560, 1994a.

[33] MP Tulin. Breaking of ocean waves and downshifting. In J. Grue et al., editor, *Waves and Nonlinear Processes in Hydrodynamics*, pages 177–190. Springer, 1996.

[34] JC Lin and D Rockwell. Evolution of a quasi-steady breaking wave. *Journal of Fluid Mechanics*, 302:29–44, 1995.

[35] D Dabiri and M Gharib. Experimental investigation of the vorticity generation within a spilling water wave. *Journal of Fluid Mechanics*, 330:113–139, 1997.

[36] H Qiao and JH Duncan. Gentle spilling breakers: crest flow-field evolution. *Journal of Fluid Mechanics*, 439:57–85, 2001.

[37] ML Banner and OM Phillips. On the incipient breaking of small scale waves. *Journal of Fluid Mechanics*, 65:647–656, 1974.

[38] ML Banner and DH Peregrine. Wave breaking in deep water. *Annual Review of Fluid Mechanics*, 25:373–397, 1993.

[39] SA Thorpe. Dyanmical processes of transfer at the sea surface. *Progress in Oceanography*, 35:315–352, 1995.

[40] WK Melville. The role of surface-wave breaking in air-sea interaction. *Annual Review of Fluid Mechanics*, 28:279–321, 1996.

[41] AT Jessup, CJ Zappa, MR Loewen, and V Hesany. Infrared remote sensing of breaking waves. *Nature*, 385(6611):52–55, JAN 2 1997.

[42] JH Duncan. Spilling breakers. *Annual Review of Fluid Mechanics*, 33:519–547, 2001.

[43] MHK Siddiqui, MR Loewen, WE Asher, and AT Jessup. Coherent structures beneath wind waves and their influence on air-water gas transfer. *Journal of Geophysical Research - Oceans*, 109(C3), MAR 17 2004.

[44] CJ Zappa, WE Asher, AT Jessup, J Klinke, and SR Long. Microbreaking and the enhancement of air-water transfer velocity. *Journal of Geophysical Research - Oceans*, 109(C8), AUG 27 2004.

[45] ML Banner and EH Fooks. On the microwave reflectivity of small-scale breaking water waves. *Proceedings of the Royal Society of London, A*, 399:93–109, 1985.

[46] WK Melville and RJ Rapp. Momentum flux in breaking waves. *Nature*, 317(6037):514–516, 1985.

[47] MJ Smith, EM Poulter, and JA McGregor. Doppler radar measurements of wave groups and breaking waves. *Journal of Geophysical Research*, 101(C6):14,269–14,282, 1996.

[48] WJ Plant, PH Dahl, and WC Keller. Microwave and acoustic scattering from parasitic capillary waves. *Journal of Geophysical Research*, 104(C11):25,853–25,866, 1999.

[49] JD Diorio, X Liu, and JH Duncan. An experimental investigation of incipient spilling breakers. *Journal of Fluid Mechanics*, 633:271–283, 2009.

[50] AH Schooley. Profiles of wind-created water waves in the capillary-gravity transition region. *Journal of Marine Research*, 16(2):100–108, 1958.

[51] CS Cox. Measurements of slopes of high-frequency wind waves. *Journal of Marine Research*, 16(3):199–225, 1958.

[52] MS Longuet-Higgins. The generation of capillary waves by steep gravity waves. *Journal of Fluid Mechanics*, 16:138–159, 1963.

[53] GD Crapper. Non-linear capillary waves generated by steep gravity waves. *Journal of Fluid Mechanics*, 40:149–159, 1970.

[54] K Okuda. Internal flow structure of short wind waves part 1: On the internal vorticity. *Journal of the Oceanographic Society of Japan*, 30:185–198, 1982.

[55] N Ebuchi, H Kawamura, and Y Toba. Fine structure of laboratory wind-wave surfaces studied using an optical method. *Boundary-Layer Meteorology*, 39(1-2):133–151, APR 1987.

[56] MS Longuet-Higgins. Progress towards understanding how waves break. In *21st Symposium on Naval Hydrodynamics*, pages 7–28, 1997.

[57] MS Longuet-Higgins. Capillary jumps on deep water. *Journal of Physical Oceanograophy*, 96(9):1957–1965, 1996.

[58] AV Fedorov and WK Melville. Nonlinear gravity-capillary waves with forcing and dissipation. *Journal of Fluid Mechanics*, 354:1–42, 1998.

[59] AV Fedorov, WK Melville, and A Rozenberg. An experimental and numerical study of parasitic capillary waves. *Physics of Fluids*, 10(6):1315–1323, JUN 1998.

[60] JH Duncan, V Philomin, H Qiao, and J Kimmel. The formation of a spilling breaker. *Physics of Fluids*, 6(9):S2, SEP 1994b.

[61] G Caulliez. Self-similarity of near-breaking short gravity wind waves. *Physics of Fluids*, 14(8):2917–2920, AUG 2002.

[62] JH Duncan. The breaking and non-breaking wave resistance of a two-dimensional hydrofoil. *Journal of Fluid Mechanics*, 126:507–520, 1983.

[63] M Miller, T Nennstiel, JH Duncan, AA Dimas, and S Pröstler. Incipient breaking of steady waves in the presence of surface wakes. *Journal of Fluid Mechanics*, 383:285–305, 1999.

[64] ML Banner and WL Peirson. Wave breaking onset and strength for two-dimensional deep-water wave groups. *Journal of Fluid Mechanics*, 585:93–115, 2007.

[65] ML Banner and JB Song. On determining the onset and strength of breaking for deep water waves Part II: Influence of wind forcing and surface shear. *Journal of Physical Oceanography*, 32(9):2559–2570, SEP 2002.

[66] JB Song and ML Banner. On determining the onset and strength of breaking for deep water waves Part I: Unforced irrotational wave groups. *Journal of Physical Oceanography*, 32(9):2541–2558, SEP 2002.

[67] MP Tulin and M Landrini. Wave breaking in the ocean and around ships. In *23rd Symposium on Naval Hydrodynamics*, pages 713–745, 2001.

[68] RJ Rapp and WK Melville. Laboratory measurements of deep-water breaking waves. *Philosophical transactions of the Royal Society of London Series A*, 331:735–800, JUN 30 1990.

[69] MS Longuet-Higgins. Instabilities of gravity-waves of finite-amplitude in deep water 2: subharmonics. *Proceedings of the Royal Society of London Series A*, 360(1703):489–505, 1978.

[70] RCY Mui and DG Dommermuth. The vortical structure of parasitic capillary waves. *Journal of Fluids Engineering*, 117(3):355–361, SEP 1995.

[71] GD Crapper. An exact solution for progressive capillary waves of arbitrary amplitude. *Journal of Fluid Mechanics*, 2(6):532–540, 1957.

[72] YC Agrawal, EA Terray, MA Donelan, PA Hwang, AJ Williams, WM Drennan, KK Kahma, and SA Kitaigorodskii. Enhanced dissipation of kinetic-energy beneath surface waves. *Nature*, 359(6392):219–220, SEP 17 1992.

[73] EA Terray, MA Donelan, YC Agrawal, WM Drennan, KK Kahma, AJ Williams, PA Hwang, and SA Kitaigorodskii. Estimates of kinetic energy dissipation under breaking waves. *Journal of Physical Oceanography*, 26(5):792–807, MAY 1996.

[74] JR Gemmrich and DM Farmer. Near-surface turbulence in the presence of breaking waves. *Journal of Physical Oceanography*, 34(5):1067–1086, MAY 2004.

[75] TK Cheung and RL Street. The turbulent layer in the water at an air-water interface. *Journal of Fluid Mechanics*, 194:133–151, 1988.

[76] L Thais and J Magnaudet. Turbulent structure beneath surface gravity waves sheared by the wind. *Journal of Fluid Mechanics*, 328:313–344, 1996.

[77] MHK Siddiqui, MR Loewen, C Richardson, WE Asher, and AT Jessup. Simultaneous particle image velocimetry and infrared imagery of microscale breaking waves. *Physics of Fluids*, 13(7):1891–1903, JUL 2001.

[78] MHK Siddiqui and MR Loewen. Characteristics of the wind drift layer and microscale breaking waves. *Journal of Fluid Mechanics*, 573:417–456, FEB 25 2007.

[79] WK Melville, F Veron, and CJ White. The velocity field under breaking waves: coherent structures and turbulence. *Journal of Fluid Mechanics*, 454:203–233, 2002.

[80] SH Oh, N Mizutani, and KD Suh. Laboratory observation of coherent structures beneath microscale and large-scale breaking waves under wind action. *Experimental Thermal and Fluid Science*, 32:1232–1247, 2008.

[81] ZC Huang, SC Hsiao, and HH Hwung. Observation of Coherent Turbulent Structure Under Breaking Wave. *International Journal of Offshore and Polare Engineering*, 19(1):15–22, MAR 2009.

[82] JH Duncan and AA Dimas. Surface ripples due to steady breaking waves. *Journal of Fluid Mechanics*, 329:309–339, 1996.

[83] A Iafrati and EF Campana. Free-surface fluctuations behind microbreakers: space-time behaviour and subsurface flow field. *Journal of Fluid Mechanics*, 529:311–347, 2005.

[84] D Coakely and JH Duncan. The flow field in steady breaking waves. In *21st Symposium on Naval Hydrodynamics*, pages 534–550, 1996.

[85] WK Melville, R Shear, and V Fabrice. Laboratory measurements of the generation and evolution of langmuir circulations. *Journal of Fluid Mechanics*, 364:31–58, 1998.

[86] Y Watanabe, H Saeki, and RJ Hosking. Three-dimensional vortex structures under breaking waves. *Journal of Fluid Mechanics*, 545:291–328, 2005.

[87] Y Watanabe, Y Hideshima, T Shigematsu, and K Takehara. Application of three-dimensional hybrid stereoscopic particle image velocimetry to breaking waves. *Measurement Science & Technology*, 17(6):1456–1469, JUN 2006.

[88] WT Tsai and LP Hung. Three-dimensional modeling of small-scale processes in the upper boundary layer bounded by a dynamic ocean surface. *Journal of Geophysical Research - Oceans*, 112(C02019), 2007.

[89] M Brocchini and DH Peregrine. The dynamics of strong turbulence at free surfaces part 1: Description. *Journal of Fluid Mechanics*, 449:225–254, 2001.

[90] T Sarpkaya. Vorticity, free surface, and surfactants. *Annual Review of Fluid Mechanics*, 28:83–128, 1996.

[91] M Gharib and A Weigand. Experimental studies of vortex disconnection and connection at a free surface. *Journal of Fluid Mechanics*, 321:59–86, 1996.

[92] CE Willert and M Gharib. The interaction of spatially modulated vortex pairs with free surfaces. *Journal of Fluid Mechanics*, 345:227–250, 1997.

[93] C Zhang, L Shen, and DKP Yue. The mechanism of vortex connection at a free surface. *Journal of Fluid Mechanics*, 384:207–241, 1999.

[94] D Dabiri and M Gharib. Simultaneous free-surface deformation and near-surface velocity measurements. *Experiments in Fluids*, 30(4):381–390, APR 2001.

[95] D Dabiri. On the interaction of a vertical shear layer with a free surface. *Journal of Fluid Mechanics*, 480:217–232, 2003.

[96] R Nagaosa. Direct numerical simulation of vortex structures and turbulent scalar transfer across a free surface in a fully developed turbulence. *Physics of Fluids*, 11(6):1581–1595, JUN 1999.

[97] R Savelsberg and W Van de Water. Turbulence of a free surface. *Physical Review Letters*, 100(034501), JAN 25 2008.

[98] R Savelsberg and W Van de Water. Experiments on free-surface turbulence. *Journal of Fluid Mechanics*, 619:95–125, JAN 25 2009.

[99] T Steinbach, X Liu, and JH Duncan. The cross-stream crest profile of gentle spilling breakers. unpublished, 2001.

[100] MS Longuet-Higgins. Shear instability in spilling breakers. *Proceedings of the Royal Society of London, A*, 446:399–409, 1994.

[101] JD Diorio, Y Cho, JH Duncan, and TR Akylas. Gravity-capillary lumps generated by a moving pressure source. *Physical Review Letters*, 103(21), 2009.

[102] H Lamb. *Hydrodynamics*. Dover, 1932.

[103] JJ Stoker. *Water Waves, the Mathematical Theory with Applications*. Wiley-Interscience, 1957.

[104] JS Russell. Report of the committee on waves. In *Rep. Meet. Brit. Assoc. Adv. Sci., Liverpool 1837*, pages 417–496, 1838.

[105] J Boussinesq. Théorie des ondes et des ramous qui se propagent le long d'un canal rectangulaire horizontal. *J. Maths Pure Appl.*, 17:55–108, 1872.

[106] DJ Korteweg and G De Vries. On the change of form of long waves advancing in a rectangular canal, and on a new type of long stationary wave. *Phil. Mag.*, pages 422–433, 1895.

[107] VH Chu and CC Mei. On slowly-varying stokes waves. *Journal of Fluid Mechanics*, 41(04):873–887, 1970.

[108] VH Chu and CC Mei. The non-linear evolution of stokes waves in deep water. *Journal of Fluid Mechanics*, 47(02):337–351, 1971.

[109] HC Yuen and BM Lake. Nonlinear deep-water waves - theory and experiment. *Physics of Fluids*, 18(8):956–960, 1975.

[110] F Dias and C Kharif. Nonlinear gravity and capillary-gravity waves. *Annual Review of Fluid Mechanics*, 31:301–346, 1999.

[111] J Satsuma and MJ Ablowitz. Two-dimensional lumps in non-linear dispersive systems. *Journal of Mathematical Physics*, 20(7):1496–1503, 1979.

[112] DJ Benney and GJ Roskes. Wave instabilities. *Studies in Applied Mathematics*, 48(4):377–&, 1969.

[113] A Davey and K Stewartson. On three-dimensional packets of surface-waves. *Proceedings of the Royal Society A*, 338(1613):101–110, 1974.

[114] PA Milewski. Three-dimensional localized solitary gravity-capillary waves. *Communications in Mathematical Sciences*, 3(1):89–99, MAR 2005.

[115] B Kim and TR Akylas. On gravity-capillary lumps part 2: Two-dimensional benjamin equation. *Journal of Fluid Mechanics*, 557:237–256, 2006.

[116] TB Benjamin. A new kind of solitary wave. *Journal of Fluid Mechanics*, 245:401–411, 1992.

[117] EI Părău, JM Vanden-Broeck, and MJ Cooker. Nonlinear three-dimensional interfacial flows with a free surface. *Journal of Fluid Mechanics*, 591:481–494, 2007a.

[118] B Akers and PA Milewski. Model equations for gravity-capillary waves in deep water. *Studies in Applied Mathematics*, 121(1):49–69, JUL 2008.

[119] TR Akylas and Y Cho. On the stability of lumps and wave collapse in water waves. *Philosophical Transactions of the Royal Society A*, 366(1876):2761–2774, AUG 13 2008.

[120] M Maleewong, R Grimshaw, and J Asavanant. Free surface flow under gravity and surface tension due to an applied pressure distribution II: Bond number less than one-third. *European Journal of Mechanics B - Fluids*, 24(4):502–521, JUL-AUG 2005.

[121] EI Părău, JM Vanden-Broeck, and MJ Cooker. Three-dimensional capillary-gravity waves generated by a moving disturbance. *Physics of Fluids*, 19(8), AUG 2007b.

[122] EI Părău, JM Vanden-Broeck, and MJ Cooker. Three-dimensional gravity-capillary solitary waves in water of finite depth and related problems. *Physics of Fluids*, 17(12), DEC 2005b.

[123] B Akers and PA Milewski. A model equation for wavepacket solitary waves arising from capillary-gravity flows. *Studies in Applied Mathematics*, 122:249–274, 2009.

[124] X Zhang. Capillary-gravity and capillary waves generated in a wind wave tank: observations and theories. *Journal of Fluid Mechanics*, 289:51–82, 1995.

[125] M Longuet-Higgins and X Zhang. Experiments on capillary-gravity waves of solitary type on deep water. *Physics of Fluids*, 9(7):1963–1968, JUL 1997.

[126] GZ Zhu, ZH Li, and DY Fu. Experiments on ring wave packet generated by water drop. *Chinese Science Bulletin*, 53(11):1634–1638, JUN 2008.